

Year: 2015

Order Number: 41826



3D Dynamic Facial Sequences Analysis for Face Recognition and Emotion Detection

By

Taleb ALASHKAR

2-Nov-2015

Thesis Committee

Mr. Renaud Segulier	Professor, CentraleSupélec Rennes, France	Reviewer
Mr. Stefanos Zafeiriou	Senior Lecturer, Imperial College London, UK	Reviewer
Ms. Bernadette Dorizzi	Professor, Télécom SudParis, France	Examiner
Mr. Stefano Berretti	Associate Professor, University of Fierenze, Italy	Examiner
Mr. Mohamed Daoudi	Professor, Télécom Lille, France	Supervisor
Mr. Boulbaba Ben Amor	Associate Professor (HDR), Télécom Lille, France	Supervisor
Ms. Hyewon Seo	CNRS Researcher (HDR), University of Strasbourg, France	Invited

ABSTRACT

In this thesis, we have investigated the problems of identity recognition and emotion detection from facial 3D shapes animations (called 4D faces). In particular, we have studied the role of facial (shapes) dynamics in revealing the human identity and their exhibited spontaneous emotion. To this end, we have adopted a comprehensive geometric framework for the purpose of analyzing 3D faces and their dynamics across time. That is, a sequence of 3D faces is first split to an indexed collection of short-term sub-sequences that are represented as matrix (subspace) which define a special matrix manifold called, Grassmann manifold (set of k -dimensional linear subspaces). The geometry of the underlying space is used to effectively compare the 3D sub-sequences, compute statistical summaries (e.g. sample mean, etc.) and quantify densely the divergence between subspaces. Two different representations have been proposed to address the problems of face recognition and emotion detection. They are respectively (1) a dictionary (of subspaces) representation associated to Dictionary Learning and Sparse Coding techniques and (2) a time-parameterized curve (trajectory) representation on the underlying space associated with the Structured-Output SVM classifier for early emotion detection. Experimental evaluations conducted on publicly available BU-4DFE, BU4D-Spontaneous and Cam3D Kinect datasets illustrate the effectiveness of these representations and the algorithmic solutions for identity recognition and emotion detection proposed in this thesis.

Keywords: 4D face recognition, Grassmann manifold, Sparse coding, Spontaneous emotion detection, Early detection, depth videos, Grassmann trajectories, pain detection.

PUBLICATIONS LIST

Submitted journal papers

1. T. Alashkar, B. Ben Amor, M. Daoudi and S. Berretti. "*3D Spontaneous Emotion Detection by Analyzing Trajectories on Grassmann Manifolds*", **Submitted** to IEEE Transaction on Affective Computing, Sep-2015.
2. T. Alashkar, B. Ben Amor, M. Daoudi and S. Berretti. "*Modeling Shape Dynamics on Grassmann Manifolds for 4D Face Recognition*", **in preparation**.

Papers in international conferences and workshops

1. T. Alashkar, B. Ben Amor, S. Berretti and M. Daoudi, "*Analyzing Trajectories on Grassmann Manifold for Early Emotion Detection from Depth Videos*", in 11th IEEE International Conference on Automatic Face and Gesture Recognition, Ljubliana, Slovenia, May-2015.
2. T. Alashkar, B. Ben Amor, M. Daoudi and S. Berretti, "*A Grassmannian Framework for Face Recognition of 3D Dynamic Sequences with Challenging Conditions*", in NORDIA ECCV Workshop 2014, Zurich, Switzerland, Sep-2014.
3. T. Alashkar, B. Ben Amor, M. Daoudi and S. Berretti, "*3D Dynamic Database for Unconstrained Face Recognition*" in 3D Body Scanning Technology, Lugano, Switzerland, Oct-2014.

National conferences

1. T. Alashkar, B. Ben Amor, S. Berretti and M. Daoudi, "*Analyse des trajectoires sur une Grassmannienne pour la detection d'emoions dans des videos de profondeur*", in journees francophones des jeunes chercheurs en vision par ordinateur (ORASIS), Amiens, France, Jun-2015.

TABLE OF CONTENTS

	Page
List of Tables	ix
List of Figures	xi
1 Introduction	5
1.1 Motivation and challenges	6
1.2 Thesis contributions	8
1.3 Organization of the manuscript	10
2 State-of-the-art on Dynamic Face Analysis	13
2.1 Introduction	13
2.2 Face recognition from dynamic data	14
2.2.1 Motion-based approaches	15
2.2.2 Frame-set approaches	18
2.2.3 Super-resolution approaches	19
2.2.4 Spatio-temporal approaches	19
2.3 Emotion recognition from dynamic data	21
2.3.1 3D feature tracking approaches	22
2.3.2 3D facial deformation approaches	24
2.4 Spontaneous emotion recognition	26
2.5 Subspace representation for face classification	27
2.6 Physical pain detection in videos	28
2.7 Early event detection in videos	29
2.8 Dynamic facial datasets	30
2.8.1 Spontaneous dynamic facial expression datasets	30
2.8.2 3D dynamic facial databases	33
2.9 Conclusion	35

3	Geometric Framework for Modeling 3D Facial Sequences	37
3.1	Introduction	37
3.2	Which data of interest?	38
3.3	Geometry of Grassmann manifolds	39
3.3.1	Special orthogonal group	40
3.3.2	Stiefel manifold	41
3.3.3	Grassmann manifolds	42
3.3.4	Exponential and logarithm map on Grassmann manifolds	44
3.3.5	Distances on Grassmann manifolds	46
3.4	Statistical learning on Grassmann manifolds	49
3.4.1	Sample (Karcher) mean computation	50
3.4.2	Grassmann k-means algorithm	51
3.4.3	Sparse coding and dictionary learning	52
3.5	Trajectories on Riemannian manifolds	54
3.5.1	Trajectories on Grassmann manifolds	55
3.5.2	Instantaneous speed along trajectories	56
3.5.3	Transported velocity vector fields of trajectories	57
3.6	Conclusion	58
4	Face Recognition from 4D Data	61
4.1	Introduction	61
4.2	Overview of the proposed solution	62
4.3	Modeling 4D-faces on Grassmann manifold	64
4.4	Identity recognition algorithms	67
4.4.1	Grassmann Nearest-Neighbor Classifier (GNNC)	68
4.4.2	Grassmann Sparse Representation Classifier (GSRC)	72
4.5	Experiments and results	73
4.5.1	BU-4DFE dataset description and pre-processing	74
4.5.2	Experimental setting	75
4.5.3	4D face recognition using GNNC	75
4.5.4	4D face recognition using GSRC	77
4.5.5	Comparative study and discussions	82
4.6	Towards 4D face recognition in adverse conditions	83
4.6.1	The full 3D/4D face recognition database	84
4.6.2	Preliminary experiments and results	85

4.7	Conclusion	88
5	Spontaneous Emotion Detection in 4D Data	91
5.1	Introduction	91
5.2	Methodology and contributions	93
5.3	Emotion detection from Kinect depth-bodies	95
5.3.1	Geometric Motion History (GMH)	96
5.3.2	Structured output learning from sequential data	96
5.4	Physical pain detection from 4D-faces	98
5.4.1	3D landmarks-based Grassmann trajectories	99
5.4.2	Depth-based Grassmann trajectories	100
5.5	Experiments and evaluation	103
5.5.1	Cam3D Kinect database	105
5.5.2	Emotional state detection	106
5.5.3	BP4D-Spontaneous facial expression database	110
5.5.4	Analyzing 4D-faces for physical pain detection	111
5.6	Conclusion	116
6	Conclusion and Perspectives	119
	Bibliography	125

LIST OF TABLES

TABLE	Page
0.1 List of symbols used and their definition in the thesis	3
2.1 Overview of spontaneous facial expressions and action units datasets.	33
2.2 Comparison of existing 4D Face databases.	34
4.1 Recognition rates (RR%) for GNN-classification using different distances	76
4.2 EI experiment: Effect of the subspace order k on the recognition rate for the GSR algorithm. Subsequences with window size $\omega = 6$ have been used in all the cases	78
4.3 EI experiment: Effect of the window size ω on the recognition accuracy for the GGDA and GSR algorithms. The subspace order k is set to keep 90% of the information	79
4.4 EI experiment: Recognition rate obtained using different training expressions compared to the approach in [128]	80
4.5 Impact of the training set on the performance: training based on only one expression vs. training based on five expressions	81
4.6 ED-experiment: Comparison between the recognition accuracy obtained for the methods proposed in this works, and for the 2D video, 3D static, and 3D dynamic (4D) approaches reported in [128]	82
4.7 ED and EI results for 2D and 3D videos	82
4.8 Processing time of the proposed pipeline compared to [128]. A 3.2GHz CPU was used in [128], compared to the 2.6GHz CPU used in our work	83
5.1 Number of available depth videos for each emotional state	106
5.2 Possible AUs related to pain according to [70].	112
5.3 AUC values for the landmarks method, with and without pose normalization, for $\delta = 1, 2, 3, 4, 5$	114

LIST OF FIGURES

FIGURE	Page
2.1 Taxonomy of 3D dynamic facial sequences analysis approaches in the two main targeted applications; face recognition and emotion classification.	16
3.1 Equally-spaced 3D frames of a sample dynamic facial sequence (of the author) conveying a happiness expression. The sequence shows some challenges, such as pose variations, incomplete data and noise.	38
3.2 Illustration of a tangent plane at point μ and tangent vectors with their map to the Grassmann manifold with Exponential and Logarithm map functions.	45
3.3 Principal angles $\Theta = [\theta_1, \dots, \theta_k]$ computed between two linear subspaces \mathcal{X} and \mathcal{Y} of the Grassmannian $\mathcal{G}_k(\mathbb{R}^n)$	47
3.4 Estimation of a Karcher mean of a set of Grassmann elements.	51
3.5 Illustration of ζ function and how to capture the spatio-temporal Euclidean feature vector from parametrized trajectory on Riemannian manifold.	57
4.1 Overview of the proposed approach: top – modeling the shape and its dynamics using a subspace representation; bottom – classification of space representations using the SRC algorithm.	63
4.2 3D static facial shape representation using the mean curvature. From left to right, the pre-processed 3D face, the mean curvature computed on the 3D mesh, and the normalized curvature-map are reported.	65
4.3 Visual illustration of two subspaces (i.e., points on the Grassmann manifold) using their singular vectors derived from SVD <i>orthogonalization</i> on sequences of $\omega = 50$ frames (<i>angry</i> , top row – <i>disgust</i> , bottom row). From left to right, the 5-dominant left singular-vectors (subspace of order 5) of the original data are shown. The first column represents the common shape description over the sequence. While the remaining columns capture the dominant facial motions of the face.	66

4.4	Information Y_k captured by the first k singular vectors returned by SVD as a function of λ . Results for different window size are reported.	68
4.5	Comparing the similarity of two 3D dynamic subsequences after presenting them as two subspaces P_i, P_j of dimension k on \mathbb{R}^n	69
4.6	(a) Each row represents a sample mean subspace dimension computed on the subsequences of the same person with different expressions. The first 6 dominant singular-vectors are used to represent the sequences in each case. Three different window size are instead considered passing from the top to the bottom row ($\omega = 6, 25, 50$, respectively) where ω refers to number of 3D frames in the original 3D sequence; (b) The energy (i.e., $\ \bar{v}\ $) minimized in Algorithm 1 for estimating the mean subspace.	70
4.7	Visual illustration of mean subspaces. In every row of the six, we have one subsapce computed from subspaces belonging to 10 different person but they were acting the same expression. Each row represents one of the six universal facial expressions, namely, from top to bottom: <i>Angry, Disgust, Fear, Happy, Sad</i> and <i>Surprise</i>	72
4.8	Trade-off between accuracy and latency (fraction of the video seen) for different Grassmann metrics/distances in the ED and EI settings.	77
4.9	EI Experiment: Trade-off between accuracy (RR%) and latency.	80
4.10	Full 3D static model from the database with and without texture information	84
4.11	The 3D dynamic sequences acquired under different conditions: a) neutral; b) expressive; c) talking; d) internal occlusion by hand; e) external occlusion by sunglasses; f) walking and g) multiple persons.	85
4.12	Overview of 4D to 4D FR approach under adverse conditions.	86
4.13	Each column shows instances belong to different subjects clustered together due to their nearby poses.	87
5.1	Dimensional Arousal-Valence chart of human emotions.	92
5.2	Dynamic depth data representation as trajectories on the Grassmann manifold $\mathcal{G}_k(\mathbb{R}^n)$. The streams of depth data at the left, are mapped to associated trajectories on the Grassmannian (right).	93
5.3	Three examples of the <i>Geometric Motion History</i> feature vectors extracted using the proposed framework.	97
5.4	Online early detection score for happiness emotion from dynamic data	98
5.5	From left to right: color image; 3D landmarks; and depth image.	100

5.6	The instantaneous speed along a trajectory on Grassmannian manifold computed for a pain depth flow for different values of $\delta = 1, 3, 6$	101
5.7	The visualization of velocity vectors first components between subspaces of one trajectory with their corresponding 2D texture images. The color maps show where the deformation happens in the face and its direction. Colors around green mean no deformation; from green to red: deformation in the positive z axis direction and from green to blue deformation in the negative z direction. The degree of the color indicates the deformation intensity.	102
5.8	Illustration of LDH computation from the velocity vectors (red arrows) between subspaces (green triangles) of the same trajectory. Taking the first component of the velocity vector, and dividing the first component into 5×5 blocks, computing the dual value histogram for every batch and concatenate them together to have the LDH_t . Concatenating LDH for a ω frames gives rise the GMH feature vector, input of the SO-SVM algorithm.	103
5.9	Cam3D Kinect database: Example depth frames with their corresponding 2D texture image of different emotional states.	105
5.10	ROC and AMOC curves for <i>Happiness</i> (top) detection and <i>Thinking/Unsure</i> detection over Stiefel and Grassmann manifolds.	108
5.11	ROC curves comparison for <i>Happiness</i> and <i>Thinking/Unsure</i> detection over the Grassmann manifold using the upper body and the face only.	109
5.12	ROC and AMOC curves for <i>Happiness</i> detection over the Grassmann manifold for two different window size (i.e., $\omega = 5$ and $\omega = 20$).	110
5.13	BP4D Database: Examples of the eight different spontaneous expressions (tasks) included in the database	111
5.14	Illustration of AU activation during a physical pain video. The horizontal axis gives the frame index in the video, and the vertical axis provides the activation (i.e. of value 1) or non-activation of the AU (i.e. of value 0).	112
5.15	ROC curve for the landmarks method. The left plots show the ROC curves after pose normalization for $\delta = \{1, 3, 6\}$, while the right plots show the performance obtained without pose normalization.	114
5.16	ROC and AMOC curves for comparison between pain detection using landmarks and depth representation.	115
5.17	ROC and AMOC curves for comparison between pain detection using <i>Local Deformation Histogram (LDH)</i> and Grassmann distances-based <i>GMH</i>	116

DEDICATION AND ACKNOWLEDGEMENTS

My efforts towards this thesis would not have been completed without the precious contribution of lots of people.

First of all, I would like to express my deep gratitude to **Prof.Mohamed Daoudi**, my PhD supervisor, for giving me the chance to work under his guidance for three years. His support, guidance and patience gave me the driving force to go forward through my PhD project. He was always available with his long experience to stand next to me to overcome any obstacle or challenge. I learned from Pro.Daoudi the importance of how to define precisely the scientific challenges in a research project, how to emphasize my effort on the right place, and that new ideas not that valuable without strong and coherent experimental validation.

Also, I would like to thank **Dr.Boulbaba Ben Amor**, my PhD co-supervisor sincerely for all his efforts and attention paid in all levels of my thesis. His advises, suggestions and everyday communication were very supportive and helpful for me and they let my work always have better shape and more valuable meaning. The most important skills, I have learned during my work with Dr.Ben Amor are how to position and link our new research ideas with the state of the art works and the patience to go through every single detail of a problem to figure out the best solution. Also, the art of illustrating complex scientific ideas in elegant and simple way for the community by writing a scientific papers or giving a talk and presentation.

My thanks also go for **Dr.Stefano Berretti** from University of Florence in Italy for his cooperation and involvement in my PhD project. In spite of the distance, the scientific meetings and discussions with Dr.Berretti always end with more clear picture in my mind about the problem and more deep thoughts about the best way to address it. His professional and academic touches had an important effect on my work. I leaned a lot from him during the three months mobility period under his direct supervision in MICC Lab in University of Florence.

A great thank for my all PhD committee members for their time and efforts they made to make my PhD defense, and a special thanks for my PhD thesis reporters for their valuable comments and feedbacks that draw my attention to important and detailed aspects. I would like to thank all our research group **3D SAM** members, Dr.Hazem Wannous, Dr.Hassen Drira, Prof.Jean Phillipe Vandeborre, Dr.Paul Auain Desrosiers and all people in CRTIStAL Lab and Telecom Lille Engineering School.

A special thanks for my graduated PhD colleagues Dr.Rim Slama and Dr. Xia Baiqiang, and current PhD students Maxime Devane, Vinecent Leon, Quentin Poloche

and Meng Meng for the great and friendly research atmosphere we had together during three years. My great thanks for all my friends: May Kahoush, Ali Mickael, Ibrahim Hatem, Ragheed Alhydar, Achille Mickael who stood always next to me. Their moral support and compassion helped me a lot reach the end of my PhD successfully.

At last, i would like to thank all of my family members especially my brother Jafar for their priceless support and love.

This thesis has been funded by *Institut Mines-Telecom* under the program **Futur et Ruptures**

TABLE OF SYMBOLS

Table 0.1: List of symbols used and their definition in the thesis

Symbol	Definition/Explanation
$SO(n)$	Special Orthogonal Group of \mathbb{R}^n
$T_\mu(M)$	Tangent space to the manifold M at point μ
$\ A\ _F$	Frobenius norm of the matrix A
$\mathcal{G}_k(\mathbb{R}^n)$	Grassmann Manifold of k -dimension subspaces of \mathbb{R}^n
$\mathcal{L}_k(\mathbb{R}^n)$	Stiefel Manifold of orthogonal matrices of size $n \times k$
\mathcal{X}, \mathcal{Y}	Subspaces on Grassmann manifold
\log_μ	Logarithm map projects Grassmann elements to T_μ
\exp_μ	Exponential map returns vector on T_μ to Grassmann manifold
$dist(.,.)$	distance on manifold
d_{Geo}	Geodesic distance
d_{proj}	Projection distance
d_{BC}	Binet-Cauchy distance
d_{Max}	Max Correlation distance
d_{Min}	Min Correlation distance
d_{Pro}	Procrustes distance
d_{Geo}	Geodesic distance
\mathbb{D}	Dictionary of atoms D_i
ω	window size (number of frames in 3D sequence)

INTRODUCTION

1 The human facial analysis is a major field of research in computer vision and pattern
2 recognition. The high interest in human faces comes not only from its ability to reveal
3 the person's identity [102] or the demographic information (gender, age, ethnicity, etc.)
4 [57], but also because it is considered as an important emotional and awareness com-
5 munication channel, which reflects some of our cognitive activities and well-being [76]
6 (sickness, stress, fatigue, . . .). One of the most important applications of face analysis
7 is identity recognition because it spans several applications, such as law enforcement,
8 surveillance systems, access control, etc. [158]. The non-intrusive nature of human faces
9 is its main advantage against other biometrics, like iris, fingerprint, voice, and hand
10 geometry, which makes it more acceptable from end-users. That is, in face-based recog-
11 nition (commercial) systems, there is no need to ask the person to make any physical
12 contact with the system, just being constantly in front of the camera for a few seconds
13 is enough. Recently, significant efforts have been paid to recognize people identity from
14 recorded footages without any cooperation from their side by using surveillance cameras
15 as done in the *Multiple Biometric Grand Challenge MBGC*¹ [129], it was also subject of
16 several evaluation contests [21, 102] and recent research studies [41]. All these studies
17 argue that robust face recognition in real-world conditions is still a distant goal.

18 From another perspective, the human face is considered as the major non-verbal
19 communication channel between human beings that shows a person's emotional states
20 via different facial expressions. The pioneering study conducted by *Paul Ekman* and

¹<http://www.nist.gov/itl/iad/ig/mbgc.cfm>

21 his colleagues [44] approved the universality of six facial expressions (happiness, anger,
22 sadness, fear, disgust, and surprise), where people from different cultures show the same
23 facial expressions for the same feelings [24]. The strong acceptance of this affirmation in
24 psychology opened the door to computer vision researchers to argue the discovery and con-
25 sider it to design their automated facial expression analysis algorithms. However, since
26 the human emotional states are more complicated than these basic six expressions in real
27 world scenarios, researchers have focused recently on the automatic recognition of com-
28 plex affects, such as thinking, hesitating, nervousness, etc. A more realistic annotation for
29 human emotional states recognition is proposed, known as arousal-valence continuous
30 human emotions charts [111]. In this annotation, the valence dimension indicates if the
31 emotional state is positive or negative and its degree. The arousal dimension indicates
32 the degree of activation of this state. To have an automatic recognition system, several
33 studies confirmed that incorporating the body, like its posture and movements with the
34 facial information can give a better understanding for human affects [94, 135]. Thus,
35 facial expressions classification and emotional state detection draw increasing attention
36 for several fields [3, 100], like in psychology, healthcare, robotics, and human-machine
37 interaction.

38 Our faces also can provide a strong evidence about our cognitive state, like the degree
39 of attention and physical state, pain and fatigue. Several applications started to appear
40 in computer vision to improve human-machine interaction, like attention assessment
41 application in online learning environment [58], fatigue detection for drivers from eye
42 movement and head gesture [98], physical pain detection [10], stress detection [81], etc.

43 **1.1 Motivation and challenges**

44 Facial visual data analysis started several decades ago with 2D still color (or grayscale)
45 images and the use of this data permitted to fulfill some applications, such as face recog-
46 nition under strictly constrained conditions [153]. 2D still images show poor performance
47 in spontaneous facial expression analysis and action units recognition, since they lack
48 the temporal information [11]. Also, performance of 2D face recognition in real world
49 scenarios based on still images, like surveillance system [13], face detection [116] and
50 face recognition in the wild [144, 159] decreases significantly due to several challenges
51 like: illumination variation, pose variation, self-occlusions by hands, hair or the face
52 itself (when changing the head pose), external occlusions by objects, like sunglasses or
53 scarf, scale variation and facial deformations.

54 All of these challenges motivated researchers to exploit 2D dynamic (video) data
55 to solve such problems because: (i) the additional spatial information available in 2D
56 videos can compensate the low-quality facial images, since we might have the face from
57 different point of views or different distances; (ii) the temporal information resides in
58 the 2D videos more effective in facial expressions and action units classification, since
59 they are by nature dynamic actions. Even in face recognition application, using 2D
60 video data can improve to certain limits the performance against previously mentioned
61 challenges. Evaluations, such as MBGC, investigated unconstrained face recognition
62 from still images and videos (2D), and showed distinctly that face recognition in adverse
63 conditions is still a distant goal [11]. A second alternative is given by the availability of 3D
64 acquisition systems, which opened the way to develop new solutions to face recognition
65 and expression classification from 3D data. Since 3D face recognition approaches use the
66 3D geometry of the face, they have the advantage of being robust against illumination
67 and pose variations [22]. However, most of the existing solutions are tested on datasets
68 collected under well-controlled settings using either static acquisition systems, like laser
69 scanners [101] or dynamic stereo-vision systems for 3D acquisition [128]. In general,
70 such systems need offline processing to obtain the 3D face model. These limitations
71 made current 3D approaches inconvenient for realistic scenarios [65]. More recent
72 advancements of 3D acquisition technologies, like structured-light and time-of-flight
73 scanners, made 3D dynamic systems available in the market at a lower cost. In spite of
74 all these benefits, the streams of 3D images (depth, meshes, unstructured point clouds,
75 etc.) present serious drawbacks, such as missing data when using a single-view capture
76 system, depth acquisition noise, changes of spatial resolution, size of space-time data
77 (non-availability yet of spatio-temporal compression techniques), which require the use
78 of adapted methodologies and appropriate tools to handle these issues. My thesis is
79 put forward in that context and proposes new compact representations and efficient
80 algorithms for processing and analyzing 4D (i.e., 3D+t) data, for the purpose of face
81 recognition and emotion detection.

82 After deciding the static data representation, one important choice will be the rep-
83 resentation of their temporal evolution to perform efficient processing and address the
84 above-mentioned problems. An emerging solution widely explored in 2D domain is map-
85 ping the original videos into a matrix manifold featuring suitable properties for the
86 analysis [88]. Among these matrix domains, the Grassmann (space of k -dimensional
87 linear subspaces of the Euclidean space \mathbb{R}^n (called the ambient space) emerges as an
88 interesting choice. In particular, one can cite: (i) its ability to produce compact low-rank

89 representation for the original video data, which can handle missing and noisy data.
90 Instead of performing feature extraction, as proposed in several works, our aim is to
91 transform the original data and keep the possibility to (faithfully) reconstruct it back
92 from the derived representation; (ii) it simplifies the computational complexity of compar-
93 ing two dynamic 3D videos by performing it using a small number of inner products; (iii)
94 the advanced statistical inference tools recently developed to fit the nonlinear structure
95 of these Riemannian domains [59, 132]. For these reasons, our modeling of the temporal
96 evolution of human 3D faces is based on mapping the original 4D data to Grassmann
97 manifolds. Based on this idea, we introduce several contributions in this thesis.

98 **1.2 Thesis contributions**

99 In this thesis, we have studied the contribution of 3D facial dynamics (i.e., temporal
100 evolution) for identity recognition and spontaneous emotion detection. Our study leads
101 to several questions of two kinds, methodological and practical. The questions related to
102 the methodology to be adopted are – (1) which representation is the most suitable for
103 analyzing 3D faces and their dynamics? (2) How to compare 3D video clips under pose
104 variations, missing and noisy data in an efficient way? (3) How the problem of dense
105 correspondence over the 3D video can be resolved? (4) Is it possible to produce statistical
106 summaries, like the mean, which allow us to perform data clustering efficiently? The
107 practical questions are as follows – (1) Can the 3D facial deformations exhibited in our
108 daily-life reveal our identity? (2) How to perform sequential (partial) analysis of 3D facial
109 sequences to allow real time emotion detection?

110 In the following, we summarize our methodological and practical contributions, when
111 considering (separately) the target applications. We recall that, when the same geometri-
112 cal framework related to the subspace representation is common for the applications, two
113 differences could be highlighted in a higher level. In fact, in 4D face recognition we adopt
114 a **dictionary (of subspace) representation** coupled with sparse coding techniques,
115 where a **trajectory (curve) representation** on Grassmann manifolds associated with
116 an early event detector is proposed for (early) spontaneous emotion detection.

117 **Face recognition from dynamic 3D data**

118 In this part, we investigate the contribution of the temporal evolution of 3D faces
119 (i.e., their shape’s dynamic deformation) in identity recognition using 4D data. To this

120 end, we adopt an (optimized) subspace representation of the flows of curvature-maps
121 computed on 3D facial frames, after normalizing their pose. Such representation allows
122 us to embody the shape as well as its temporal evolution within the same subspace
123 representation. Then, we use recently-developed techniques of dictionary learning and
124 sparse coding over the space of fixed-dimensional subspaces, called Grassmann manifolds,
125 to perform face recognition. To show the effectiveness of the proposed method, we have
126 conducted extensive experiments on the BU-4DFE dataset, and we discuss here obtained
127 results with respect to current literature. Besides, two classification methods have been
128 proposed: a Grassmann Nearest-Neighbor classifier (GNNC) involving geometric mean
129 subspaces for subject classes, and a Grassmann Sparse Representation Classifier (GSRC)
130 performed on the sparse representations of the subspaces. While the latter is inspired by
131 an extrinsic solution, the former is an intrinsic solution. The GSRC is computationally
132 cheaper and achieves better accuracy compared to GNNC. It also scores competitive
133 performance with respect to the approaches previously proposed. Our evaluations showed
134 clearly that considering the face shape’s behavior over time improves the face recognition
135 accuracy under both expression-specific and non-specific settings. We also investigated
136 the proposed geometric approach on challenging face recognition scenarios under pose
137 variation and other challenges, like facial expressions, talking, walking, internal and
138 external occlusion from our collected database.

139 **Spontaneous emotions detection in 4D data**

140 We propose a unified framework for the purpose of online emotion detection, such as
141 happiness or physical pain, in-depth videos. Our approach consists of mapping the videos
142 onto the Grassmann manifold (i.e., the space of k -dimensional linear subspaces) to build
143 time-parameterized trajectories. To do that, depth videos are decomposed into short-
144 time clips, each approximated by a k -dimensional linear subspace, which is in turn a
145 point on the Grassmann manifold. Considering the temporal evolution of subspaces
146 gives rise to a precise mathematical representation of trajectories on the underlying
147 manifold. Extracted spatio-temporal features based on computing the velocity vectors
148 along the observed trajectories, termed Geometric Motion History (or GMH), are fed into
149 an early event detector based on Structured Output SVM, thus enabling online emotion
150 detection. Experimental results obtained on the publicly available Cam3D Kinect and
151 BP4D-Spontaneous database validate the proposed solution. When the first database
152 has served to exemplify the proposed framework on depth sequences of the upper part
153 of the body (depth-bodies) from depth-consumer cameras, the same framework is also

154 applied to high-resolution and long 4D-faces for physical pain detection, using the second
155 database.

156 **New full 3D/4D face dataset**

157 In addition to the contributions presented above, we have collected a new 3D/4D FR
158 database of 58 subjects, which presents the following features: (1) It includes the most
159 common face recognition challenges in real-world like scenarios, such as pose variation,
160 facial expressions, talking, walking, multiple persons in the scene, internal and external
161 occlusions, which have not been included in any 4D database so far; (2) The low-resolution
162 of the 3D scans is more convenient to simulate 4D face acquisition under less constrained
163 conditions; (3) Free head movement is permitted during recording the 3D videos on
164 the subject due to the wide field-of-view of the used 3D scanner. In addition to the 3D
165 facial sequences (uncontrolled), we have also collected, for each subject, a full 3D static
166 model with high-resolution (up to 50k vertices), with the texture mapped on it. We have
167 conducted preliminary experiments on this dataset, in addition to our evaluation on
168 publicly available datasets – BU-4DFE [148], Cam3D [90], and BP-4D Spontaneous
169 emotion dataset [152].

170 **1.3 Organization of the manuscript**

171 After this general introduction, the rest of the thesis consists of four chapters and a
172 general conclusion, as follows:

173

174 **Chapter 2** provides a comprehensive state-of-the-art on dynamic face analysis from
175 different imagery channels, with a particular emphasis on approaches which use 4D data.
176 We first motivate the shift from 2D to 3D, then to 4D data, for both target applications
177 face recognition and emotion classification and detection. A particular focus will be given
178 to the recently-developed approaches, which exploit 4D data (meshes, depth images,
179 point clouds, etc.) in a facial analysis.

180

181 In **Chapter 3**, we first recall essential background materials of the Grassmann ge-
182 ometry (distances, tangent space, geodesic, velocity vector, Karcher mean computation,
183 etc.), then we derive our representations using (1) dictionary of subspaces and related
184 tools, such that the sparse coding and dictionary learning, and (2) trajectory of subspaces

185 representation and sequential analysis tools. The exploitation of these representations
186 will be investigated in the next two chapters, respectively.

187
188 **Chapter 4** presents our geometric framework for face recognition from 3D dynamic
189 videos, which is based on sparse coding on Grassmann manifold and its comparison with
190 baseline algorithms and previous studies. Experimental evaluation and discussions on
191 the publicly-available BU-4DFE database are reported. In this chapter, we also describe
192 our new Full 3D/4D face dataset and open the horizon to 4D face recognition in uncon-
193 strained conditions, with some preliminary experimental results.

194
195 In **Chapter 5**, trajectory analysis on Grassmann and Stiefel manifolds is presented
196 with two applications: First, the early detection of spontaneous emotional states from
197 depth videos of the upper part of the body. The importance of incorporating the upper part
198 of the body with the facial data is exemplified here using the segmented Kinect Cam3D
199 dataset. Second, the application of our framework to early detection of spontaneous
200 physical pain affect from high-resolution 3D facial videos is presented. An experimental
201 illustration and comprehensive discussion of the ability of trajectories on Grassmann
202 manifolds to model 4D facial data is given in this chapter.

203
204 **Chapter 6** summarizes the main contributions, states the main limitations of the
205 proposed approaches and opens some perspectives and future directions.

STATE-OF-THE-ART ON DYNAMIC FACE ANALYSIS

2.1 Introduction

206 Face analysis represents a major scope of study in computer vision and pattern recogni-
207 tion fields due to its wide range of applications in biometrics, human machine interaction,
208 affective computing, etc. The design of any proposed solution in this domain related
209 strongly to the availability of the imaging systems in the first place. In the last few
210 years, 3D dynamic acquisition systems with both high- and low-resolution became avail-
211 able at affordable prices on the market. This technological innovation opened a new
212 direction in front of facial analysis to exploit the richness of the new modality (3D+t
213 or 4D). Researchers in computer vision needed to answer the fundamental questions
214 concerning 3D dynamic systems like: what is the main additive values such new imaging
215 systems carry into facial analysis problems? To which extent, using 3D dynamics can
216 solve challenges that 2D (static/dynamic) and 3D static systems can't solve? What are the
217 main limitations and constraints related to the adoption of such systems in automatic
218 facial analysis solutions?

219 The starting point to find answers was collecting new databases that include the basic
220 challenges and problems needed to be solved in facial analysis domain. Till now, more
221 attention was paid to facial expressions analysis and human affects understanding from
222 3D dynamics, than face recognition problem. Another important aspect we would like
223 to highlight here is the new trend in facial expression and emotional states recognition
224 approaches to move from acted (or posed) to spontaneous and realistic, which are harder

225 to solve, but more useful and valuable for real-world applications. Also, to make the facial
226 expressions and emotional states and affects, like physical pain detection, much more
227 useful in action, moving into early recognition and detection is very important. Early
228 recognition and detection means that the proposed automatic system should be able to
229 recognize the expression and give a decision as early as possible (i.e., with low-latency)
230 and not to wait until the end of the state. Investigating these challenges and what
231 performance 3D dynamic data have under such conditions is a major interest for our
232 work in this thesis.

233 In this chapter, we review most significant contributions made in face analysis from
234 dynamic data, in particular using 3D imaging systems. A review of face recognition
235 from 3D dynamic data is presented in Sect. 2.2, and for emotion recognition in Sect. 2.3.
236 A short review for spontaneous emotion detection and classification from 2D videos is
237 presented in Sect. 2.4. Sect. 2.6 reviews the literature on physical pain recognition from
238 facial data. In Sect. 2.7, a review on early event detection from dynamics data is drawn.
239 The most important 3D dynamic facial databases in the community are discussed with
240 a comparison in Sect. 2.8. In Sect. 2.9, we conclude and discuss where our work in this
241 thesis stands according to the literature.

242 **2.2 Face recognition from dynamic data**

243 Dynamic face recognition approaches started with 2D color image modality. The main
244 motivations for using the 2D videos for such problem come from the fact that dynamic
245 faces can overcome real-world challenges. For example, (i) **the pose variation:** the
246 availability of dynamic sequence from different poses for the individual can help to
247 obtain a complete information for the face; (ii) **noise or missing data:** The 2D facial
248 sequences can compensate such problems partially by its information richness; and the
249 (ii) **facial temporal dynamic:** which can improve the identity recognition process.

250 There are four categories for face recognition from 2D/3D video: 1) image set-based
251 approaches (called also multiple-instance), where the order of the images through the
252 time is ignored (i.e. the motion information is not considered here); 2) motion-based ap-
253 proaches where only the motion information is considered; 3) super-resolution approach
254 which consists to fuse several 2D/3D frames of low resolution to build higher resolution
255 image; and 4) sequence-based approaches, where the image order is considered since
256 they exploit the spatio-temporal information together to make the recognition process.
257 Even though face recognition approaches from 2D videos can give better performance

258 under illumination, pose variation and occlusion than 2D still, they can improve only to
259 a certain limit. A complete survey about face recognition from 2D videos can be found in
260 [11].

261 From another perspective, the advancement in imaging technologies made the 3D
262 static scanning systems available on the market for research and industrial applica-
263 tions. The availability of such 3D static imaging systems led to a quantum leap in facial
264 analysis applications, because of its efficiency in solving profound challenges in 2D
265 static and dynamic domains, which are illumination change and pose variation. Also,
266 it opens the door in front of merging the 2D texture information and the 3D geometry
267 of human faces for robust face recognition solutions. 3D static solutions show higher
268 performance than 2D static and dynamic solutions under pose variation, illumination
269 changes and in the presence of occlusion (we refer the reader to [2] for a comprehen-
270 sive discussion). In the last few years, 3D dynamic imaging systems started to appear
271 combining the advantages of dynamic information alongside the 3D information in two
272 main models: 1) high-resolution, but expensive, 3D dynamic acquisition systems, like the
273 Di4D acquisition system. This system gives high- temporal and spatial resolutions and
274 needs to make the acquisition under highly conditioned environment. It also requires an
275 offline reconstruction process; 2) the low-resolution depth-consumer cameras, such as
276 the Microsoft Kinect, which give depth data in low-resolution at 30fps in real-time, and
277 are available at affordable price even for personal use. An overview of 3D dynamic facial
278 sequences analysis is depicted in Fig. 2.1.

279 In the following sections, we review the state-of-the-art approaches based on this
280 taxonomy, where a first level of categorization is made based on the target applications.

281 **2.2.1 Motion-based approaches**

282 Starting from the fact of human face is a dynamic surface by nature i.e. besides its
283 constant shape feature it has its motion which is an important non-verbal communication
284 channel. The face non-rigid dynamic can be categorized into a) the speech production
285 movement, b) the facial expression and c) the eye gaze changes. Several studies from the
286 psychology field addressed the question of: **How facial motion information affect**
287 **face recognition process in human perception?** Actually, even some studies in the
288 literature claimed that the motion information has no effect on the recognition process
289 such as [33],[23], several other studies revealed evidence and findings that approve that
290 the recognition could be improved in certain context [125],[108]. From the cognitive

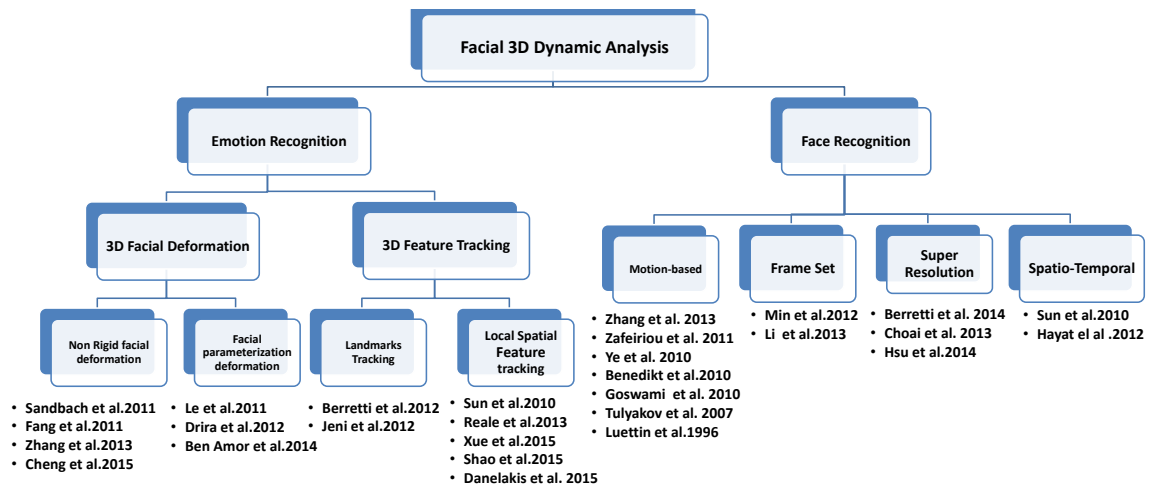


Figure 2.1: Taxonomy of 3D dynamic facial sequences analysis approaches in the two main targeted applications; face recognition and emotion classification.

291 point-of-view the motion information can support the identity recognition from facial
 292 sequences and there are two main directions here:

- 293 • The first direction of physiological studies posit that people depend firstly on the
 294 face structure static feature since it is consistent during the time and the they
 295 dynamic non-rigid facial deformations are not granted to be repeated reliably but
 296 the motion information can play a role in recognition when the quality of the face
 297 is degraded. Knight et Johnston [75] conducted a study to evaluate the role of
 298 the motion information and they found that the dynamic of the face gives better
 299 recognition when the quality of the shape is degraded significantly but not when
 300 the face image in a good quality. LANDER et al. [77] study showed that motion
 301 information improve the recognizing in low quality image and for famous faces
 302 more than others since the facial subtle changes need more time to be learned.
- 303 • The second direction posits that the additional views available from seeing the
 304 human motion information help the observer to infer the 3D structure of the face
 305 which is based on structure-from-motion concept. Also, they claim that the non-
 306 rigid deformation on the facial image gives cues about the 3D structure of the face.
 307 Pike et al.[104] study showed that seeing a human face in motion gives better
 308 recognition than in static or by seeing an image set that doesn't preserve the order
 309 of the deformation through the time and the motion information is more than a

310 sum of multiple view of one static face image.

311 In computer vision community it was agreed that one of the challenges of the face
312 recognition in 2D and 3D domain is its sensitivity to facial expression variations and
313 several approaches are proposed to build expression-invariant face recognition systems
314 such as Chang et al.[29]. Recently and inspired by works of physiology that approved
315 that possibility to have idiosyncratic models from facial motions several works start to
316 appear to investigate the efficiency of considering the facial dynamics as a biometric
317 signature. Most of the works in this direction focus on speech production lips movement
318 tracking over the time where few of them started to appear more recently that study
319 the facial deformation which is not related to speech production. One of the first works
320 on speech-related motion investigation as a behaviometrics is proposed by Luettin, et
321 al.[87]. In this work the lips boundary and the intensity of the mouth area is tracked
322 over 2D video to build spatio-temporal descriptor using HMM. The authors approve
323 the possibility of identifying the speaker in both text dependent and text independent
324 scenarios. Goswami et al. [54] proposed a method that models the appearance and the
325 dynamics features of the lips region for speaker verification. The promising results
326 obtained in this study made using the moving lips as a primary biometric modality is
327 acceptable after it was seen as a soft-biometric before. An extension for this work is
328 presented in [28]. Benedikt et al. investigated in [17] the uniqueness and permanence of
329 facial action units that comes from verbal and non-verbal facial actions. Evaluation is
330 conducted on 3D videos and it showed that the speech-related action units gives better
331 performance in identification and verification than the speech-unrelated such as smile
332 and disgust. Zhang et al. [152] proposed to distinguish between twins faces using the
333 facial motion information extracted from their talking profiles. This study shows that the
334 talking profile can be a good biometric for twins identification. Several works appeared
335 to address the person identity recognition out of lips motion such as [107] [54], [47].

336 For speech-unrelated works that take the whole facial region deformation as a
337 biometric, one of the earliest works that approved the feasibility of using facial motion
338 as a biometric is presented in [34]. In [156], Zhang et al. proposed to capture the an
339 elastic strain pattern which describes the anatomical and bio-mechanical characteristics
340 of the facial tissue . This extracted pattern can serve as a new biometric to identify
341 the person. This elastic strain pattern computed by applying finite elements method
342 and the experimental study is conducted on a small 3D face dataset. Tulyakov et al in
343 [131] modeled the facial motion information by computing the displacement between
344 corresponding facial keypoints in two different images of the same person one in neutral

345 state and the other in the apex of the expression state. The resulted pattern out of this
346 distances showed that it can be used as a biometric for person verification on two datasets.
347 Zafeiriou and Pantic in [149] also conducted a study to evaluate the efficiency of using
348 the motion information out of smile/laughter spontaneous episode on a small dataset
349 for person identification. Authors compute a motion complex vector fields between the
350 neutral frame and the apex frame using the Free Form Deformation (FFD) algorithm
351 and used complex data reduction technique such as complex LDA and PCA. The obtained
352 results give evidence that the spontaneous smile/laughter facial expression is able to
353 verify the identity of the person automatically. Previously mentioned works used facial
354 motion as biometrics are limited to certain type of facial expressions such as smile, Ye et
355 al.[147] proposed more general motion-based face recognition approach. In this method,
356 author extracted identity evidence from various types of facial motions in a local manner
357 and it is called Local Deformation Profile (LDP).

358 **2.2.2 Frame-set approaches**

359 One approach to exploit 3D dynamic data is by applying fusion at the decision level,
360 which gives a more robust recognition process where the order of frames is not taken
361 into account. These approaches that use more than one 3D frame for the person to learn
362 his/her identity can improve the recognition. An example of such methods is proposed
363 in [96], where a real-time 3D face recognition system using multiple RGB-D instances
364 is presented. This approach shows that exploiting majority voting between multiple
365 instances for short time, from 0.5 to 4 seconds, gives 100% recognition rate, while using
366 the same approach on single depth image achieves 97.9% on a real-world small dataset of
367 20 subjects. Li et al. [79] proposed an algorithm for face recognition under varying poses,
368 expressions, illumination and disguise from depth and color flows. For every subject,
369 there are 89 RGB-D images under different combinations of pose, illumination, facial
370 expressions and occlusion. 18 RGB-D images for every subject under different conditions
371 used for learning two dictionaries one for depth and another for texture information
372 separately, then a fusion is made at the decision level. The testing probe is one of the
373 remaining samples. This work shows that using a set of images that covers different
374 conditions for learning the subject class can give better recognition rate than using only
375 one. Also, fusing the depth and the color channels gives better results of 96.7% compared
376 to the result of the depth channel taken alone of 88.7%.

377 **2.2.3 Super-resolution approaches**

378 Another approach to deal with 3D dynamic data is to register the 3D depth or 3D available
379 meshes to build a **super-resolution** face with higher quality and details. Thus, one
380 can obtain better recognition rate than using single 3D frames to decide. The fusion
381 here happened at the data level to have higher resolution data. Several works adopted
382 this method for face recognition from 3D dynamic data, like in [20] where Berretti et al.
383 investigated the impact of 3D facial scans resolution on the recognition rate by building
384 super-resolution 3D models from consumer depth camera. A sequence of depth frames
385 has been preprocessed, aligned and finally merged to create a super-resolution 3D face.
386 Comparing this synthetic 3D face with 3D high-resolution model captured by *3dMD*
387 system shows that using the reconstructed (super-resolution) model outperforms single
388 depth or high-resolution models acquired using a high-resolution system. In a similar
389 way, Choi et al. in [32] have proposed a comparison study, in face recognition problem,
390 between three methods – 1) single depth frame vs. set of depth frames, 2) single depth
391 frame vs. another set of depth frames, 3) 3D model vs. 3D model, where this 3D model is
392 constructed by registering a set of depth frames. The experimental results on a small
393 dataset consisted of 20 RGB-D videos of 10 subjects show that 3D vs. 3D model approach
394 gives the higher recognition rate. Hsu et al. [64] showed that super-resolution method
395 can improve the recognition rate across pose variation. The 3D model captured from a
396 depth sequence can help to have different 2D texture images of the probe in different
397 pose settings to match the gallery texture image poses, which leads to better recognition
398 rate. The main limitation of this method is the consuming time of the registration-merge
399 process. Also, it might require annotated landmarks.

400 **2.2.4 Spatio-temporal approaches**

401 Since human face is a 3D surface with high dynamics features by nature, the spatio-
402 temporal representation that can encompass both the 3D shape features and its motion
403 traits through the time will be the most natural modeling and it is believed that it allows
404 more efficient face analysis. This believe is supported by the success achieved in face
405 recognition approaches that incorporated the dynamic traits with the static features but
406 in 2D video such as [43], [83]. Also, several works start to appear recently that succeed
407 to exploit the motion facial information as a biometric for identification and verification
408 tasks out of 2D [147],[149] and 3D videos such as [17].

409 In this category, the 3D dynamic data should be aligned and tracked precisely through

410 time to build a spatio-temporal descriptor. Here, unlike the frame set approaches, the
411 frame order and alignment is critical to have a robust representation. In [128], Sun et
412 al. proposed a spatio-temporal approach that uses a generic deformable 3D face model
413 to track facial deformations in both space and time. To have an accurate temporal
414 representation of the face deformation over time, a vertex tracking technique is applied
415 to adapt the 3D generic model with each (static) scan. Thus, each 3D scan can be modeled
416 by a spatial-temporal feature vector that describes the shape and the motion information
417 to have an efficient representation. Two types of Hidden Markov Models (HMM) are
418 trained – a Temporal (T-HMM), which models the motion information (inter-frame),
419 and the Spatial (S-HMM) that model the geometrical face information on the same
420 face (intra-frame). The two HMMs are combined to have (ST-HMM) at the decision-
421 level. This approach applied on face recognition on 60 subjects of BU-4DFE dataset
422 in Expression-dependent and -independent settings and it gives 97.89% and 94.14%,
423 respectively. The main limitation of this approach is its high computational (time) cost
424 especially for the vertex tracking step, which also needs a set of 22 landmarks annotation
425 to be done. In their work, Sun et al. have made a comparative study with 2D-video
426 and 3D static face recognition and have shown clearly the usefulness of the dynamic
427 3D data in face recognition. More recently, in [61] Hayat et al. proposed an automatic
428 face recognition approach from 3D videos on BU-4DFE database. After automatic face
429 detection, cropping and alignment of static frames, 3D scans are converted into depth
430 frames. The face depth videos are divided into 4×4 non-overlapping video cuboids. A
431 dynamic version of Local binary pattern (LBP) descriptor called (TOP-LBP) computed
432 on each dynamic cuboids in three spaces (XY), (XT) and (YT), where X, Y is the depth
433 frame dimension and T is the time dimension. LBPs-TOP computed from all video
434 cuboids are concatenated to form a feature vector for the complete video using multi-
435 class support vector machine (SVM) algorithm. Evaluating this method on all BU-4DFE
436 database using 10-fold cross validation gives 92.68% of recognition rate. The promising
437 results obtained from this spatio-temporal approaches show clearly the importance of
438 including the temporal information beside the spatial in the 3D domain to have higher
439 recognition rates. The main drawbacks reside in the tracking solution, which is very slow
440 and sensitive to noise and missing data.

441 According to the very few works on 3D dynamic face recognition, this direction in face
442 recognition is still not well explored. The results obtained from current literature state
443 the importance of the temporal information with the spatial information. To address
444 these issues in current spatio-temporal methods, we proposed to use in this thesis an

445 optimized **subspace representation**. The main advantages of this choice are its ability
446 to keep the spatial and temporal information as singular vectors, it provides compact
447 and lower dimension representation of the high dimension original data, which makes
448 3D video classification and comparison faster, and it is a faithful representation since we
449 can always come back to the original data from the subspace basis. The mathematical
450 notation for this representation is introduced in the next Chapter 3 and our 4D face
451 recognition approach presented in Chapter 4.

452 **2.3 Emotion recognition from dynamic data**

453 The non-verbal channel plays an important role in human-to-human communication,
454 especially in feelings and emotional states recognition. This statement is confirmed in
455 the study proposed by Mehrabian et al. [95], which states that in some context the visual,
456 vocal and verbal elements participate in 55%, 38%, and 7% in feelings and attitude
457 communication, respectively. Such studies motivated researchers in computer vision
458 and affective computing to develop automated systems for emotional states and human
459 affects detection and understanding from facial expressions and body language visual
460 data [151]. The dynamic nature of facial expressions of human face motivated to model
461 and analyze this problem in 2D videos in an early stage. The challenges that affect
462 2D videos, especially the pose variation and illumination changes, can hinder accurate
463 facial expression analysis. More comprehensive survey of video-based facial expression
464 analysis, challenges and limitations can be found in [97, 114].

465 The problems of pose variations and illumination changes can be solved in 3D
466 modality, which had a great advancement in last few years where several 3D dynamic
467 databases were collected for facial expression and action units recognition as discussed
468 later in detail. In addition to this technological feasibility of studying facial expressions
469 in 3D dynamic space, the human face itself is a 3D dynamic surface by nature. Several
470 approaches appeared in last few years in the literature addressing the problem of
471 automatic facial expressions analysis from 3D dynamic data, either from high-resolution
472 3D data or low-resolution depth data. The methodologies used in these approaches
473 fall in two main groups – the 3D feature tracking approaches, and the second group
474 including the 3D deformation based approaches, which depend on estimating the non-
475 rigid deformation between static 3D frames themselves or by fitting a generic model.

476 **2.3.1 3D feature tracking approaches**

477 In this category of 3D dynamic facial sequences analysis, there are two methods. The
478 first one is called local feature tracking. In this method, the 3D facial scans are divided
479 into small patches around keypoints or landmarks, a local 3D feature is extracted from
480 each patch and tracked along the video to have a spatio-temporal descriptor. The second
481 method is called landmarks tracking approach. It focuses only on the keypoints or
482 landmarks themselves not on the facial patches around them, where some distances
483 between predefined landmarks on the facial scan are computed and tracked over the
484 time to model the 3D facial dynamics data.

485 **Local feature tracking approaches**

486 Tracking the local spatial information on 3D faces through the video is one of the most
487 common methodologies. Selecting the local descriptor is a critical point, and the 3D scans
488 alignment is very important.

489 One of the earliest studies that addressed facial expression recognition from 3D
490 dynamic scans is proposed by Sun et al. [128], which was applied for 3D dynamic face
491 recognition and it is discussed in the previous section. The same approach was applied
492 to classify the six facial expressions on the frame level using LDA classifier. The average
493 recognition rate is 83.7%, which is better than the results obtained from 2D videos
494 and 3D static approaches on the same database. More recently, Reale et al. [105] from
495 the same group have proposed a 4D spatio-temporal descriptor called *Nebula* for 4D
496 facial expressions and movement analysis. The starting point to build this descriptor is
497 aligning the 3D frames precisely, and creating a local spherical voxel around the starting
498 frame points, through the time. The curvature is computed for the points of this voxel
499 and they are assigned into different label values to create the feature vector. Besides
500 the curvature value, the least curvature polar angles are computed alongside the value
501 to create the proposed spatio-temporal representation, which can be sensitive to the
502 speed of performing the facial expression or the action unit. A histogram for each facial
503 region is created from the three computed values (curvature value and the two polar
504 angles) concatenating all histograms' regions to have the final feature vector. This new
505 4D descriptor is evaluated on BU-4DFE database for facial expression recognition and
506 on BP4D-Spontaneous database for action units detection, and the reported results show
507 that it outperforms previous spatio-temporal descriptors. This dynamic feature vector
508 is computed on a subsequence of N frames, unlike the other vectors that are computed

509 between two frames, which can speed-up the performance.

510 Furthermore, in [143] Xue et al. proposed a descriptor to analyze 3D expression
511 sequences changing over time. The facial area is divided into spherical patches of radius
512 r around 68 annotated landmarks. Applying Discrete Cosine Transform (DCT) on the
513 three dimensions of the data results in a spatio-temporal representation for the 3D
514 facial patch through the time (called 3D-DCT). Concatenating the 3D-DCTs for all facial
515 patches gives the final facial representation for the 3D subsequence of size N . Passing
516 these high-dimensional feature vector into *minimal redundancy maximal relevance*
517 (*mRMR*) allows to keep the most relevant features. Then, a nearest neighbor classifier is
518 applied to recognize the six facial expressions on BU-4DFE database, which gives 78.8%
519 recognition rate on average. The results obtained from this work state that producing
520 the spatio-temporal features from subsequences is more appropriate than extracting it
521 from frame-to-frame deformation method.

522 In order to investigate the performance of 3D dynamic facial analysis on low-
523 resolution depth data, Shao et al. [118] produced three different resolution depth videos
524 from 3D videos of BU-4DFE database. In this work, the authors proposed to divide the
525 facial area at both the gray scale (obtained from 2D color images) and the depth video (ob-
526 tained from 3D scans) into spatio-temporal cuboids, then applying LBP-TOP descriptor
527 on the volume data to have a robust representation for every cuboid. Pooling the feature
528 vectors obtained from the grayscale and the depth cuboids together allows learning
529 codebooks that represent dynamic facial expression videos by few feature vectors using
530 sparse coding. Conditional Random Fields learning algorithm is used to classify the
531 six expressions, and it obtains 83.07%, 79.38%, 69.1% for the six expressions using the
532 three different decreasing resolutions, respectively. Addressing the same problem with 8
533 landmarks only, Danelakis et al. in [37] proposed a geometrical descriptor called Heart
534 Kernel Signature (HKS). This descriptor is computed around each landmark on the 3D
535 mesh itself and on the normal vectors estimated at each vertex, then concatenating the
536 set to build a spatial feature vector of the scan. Applying a wavelet-based transformation
537 on these spatial features over time gives rise to the spatio-temporal representation.
538 Evaluation results on BU-4DFE dataset show theirsuperiority against many others.

539 **Landmarks tracking approaches**

540 In this method, the 3D face is represented only by the landmarks position themselves
541 and some distances among them. Tracking this simple spatial representation through the
542 video gives the spatio-temporal representation used to classify the expression embedded

543 in the data. Berretti et al. [19] addressed the problem of facial expression recognition by
544 proposing a real-time landmark tracking approach for analyzing 4D data. The method
545 starts by detecting the nose tip first, then automatically detecting other facial landmarks
546 around the mouth and eyes regions. A set of distances between mouth region areas, nose
547 and mouth borders, and eyes area is computed to describe each 3D facial scan. These
548 distances are normalized in two steps to be independent of the person. Finally, a HMM
549 classifier is used for recognition evaluation on three expressions (Happy, Angry and
550 Surprise) out of BU-4DFE database and achieves 76.3% classification rate on average.
551 Another landmark-tracking-based approach is proposed by Jeni et al. [67] that addressed
552 the independent person facial expression problem under pose variation in 2D and 3D
553 dynamic facial data. In this method, the difference between landmarks of the neutral
554 frame and the others through the video is measured and passed to multi-class SVM
555 classifier. Evaluation on CK+ 2D video and BU-4DFE datasets shows interesting results.
556 In this method, selecting stable landmarks tracking algorithm is very important for
557 robust facial expression recognition performance.

558 **2.3.2 3D facial deformation approaches**

559 The main idea behind approaches in this category is the fitting accuracy performed
560 between 3D frames and the reference to be able to measure the temporal evolution
561 through the time. They are divided into two methods: the non-rigid facial deformation
562 and the parametrized facial deformation.

563 **Non-Rigid facial deformation approaches**

564 The principle of these methods is the ability to capture the temporal deformation of the
565 3D facial scans by fitting a reference model to the 3D frames of the video. For example,
566 in [112] a fully automatic approach for analyzing facial expression is introduced. After
567 preprocessing and alignment of 3D frames of one video, the motion temporal information
568 obtained by computing the Free Deformation Model (FDD) initially presented in [110]
569 between successive frames and a quad-tree decomposition is applied to the resulted
570 FDDs vectors to have more accurate feature description. Feature selection and training
571 step are implemented in the same time using GentleBoost classifiers one for onset and
572 another for offset segments. The temporal modeling is performed using HMMs, where
573 the full expressions is considered as one HMM of 4 steps: the expression starts with
574 *neutral*, then *onset*, *apex* and ends with *offset*. This approach is evaluated on three

575 expressions (Happy, Angry, Surprise) available in BU-4DFE database and a comparison
576 with 2D video data is conducted. Obtained results, 81.93% recognition rate, show that
577 3D dynamic data gives a higher performance. An extension of this work is presented in
578 [113].

579 A fully automatic 4D facial expression analysis approach is presented in [46]. In this
580 work, Fang et al. proposed a new 4D data registration approach that preserves temporal
581 coherence between successive scans and robustness against outliers. The LBP-TOP
582 descriptor initially proposed in [157] is implemented on the difference maps between
583 3D video frames and the first frame. Evaluation on BU-4DFE database gives 74.63%
584 on the six expressions, it gives 96.71% when it is tested on three expressions (Angry,
585 Happy and Surprise) and it gives 95.75% when it is tested on (Happy, Sad and Surprise).
586 A Similar approach was proposed by the same authors in [45]. Different registration
587 algorithms are evaluated including ICP (Iterative Closest Point) and more advanced
588 mesh matching techniques, like MeshHOG and Spin Images with application to facial
589 expression recognition from 3D static and dynamic scans. Since template fitting used in
590 these approaches is important especially under facial expressions, recently, Cheng et al.
591 [31] proposed a new algorithm to adapt a 3D model to a high-resolution depth scan. This
592 fitting algorithm, called Active non-rigid ICP, can handle the highly deformable nature
593 of the face by learning statistical models for local regions. Combining these statistical
594 models with non-rigid Iterative Closet Point (ICP) algorithm, which is used also in [8],
595 is implemented to have robust fitting. Evaluating the performance of the new fitting
596 algorithm is approved by its higher performance on facial expression recognition from
597 BU-4DFE database especially in strongly deformed scans, like in surprise expression.

598 **Facial parameterization-based approaches**

599 In [39] and [15], the authors proposed a Riemannian framework, which allows dealing
600 with 3D face registration and pose normalization. The authors started a parameterization
601 based on radial curves emanating from the nose tip with fixed rotation angle between
602 them. These curves allow to capture the geometry of the 3D face where every curve
603 consists of fixed number of points. To capture the dynamic facial deformation through
604 the video, they used Riemannian method for shape analysis of curves to compute the
605 Dense Scalar Fields (termed DSF). This DSF is the tangent vector field between the
606 corresponding curves that belong to two different 3D faces after considering each curve as
607 an element of a Riemannian manifold. Two classification schemes are proposed (1) using
608 a multi-class Random Forest algorithm applied on the mean deformations and (2) HMM

609 classifier applied on the motion. The authors provided evaluations on BU4DFE database
610 with an average recognition rate of 93.21%. In [78], Le et al. presented a spatio-temporal
611 method, which uses the planar iso-level curves as 3D face parameterization. These level
612 curves give the spatial information of the 3D facial scan, and they used the Chamfer
613 distance between corresponding curves of successive frames to capture the temporal
614 evolution over time. Resulted features represent a spatio-temporal information, and
615 they are passed to a HMM classifier. The evaluation results reported on happy, sad and
616 surprise expressions gives 92.22% in average recognition rate from BU-4DFE dataset. A
617 recent and more comprehensive survey on facial expression recognition from 3D video
618 sequences is published in [38].

619 **2.4 Spontaneous emotion recognition**

620 Within the efforts dedicated to bring spontaneous facial expressions from 2D to 3D,
621 databases started recently to appear considering this aspect. For example, in [7] Sherin
622 et al. presented a Kinect based facial expressions database for recognizing seven acted
623 and spontaneous expressions of 32 subjects. Zhang et al. [152] presented a high-resolution
624 3D dynamic spontaneous facial expression database with 3D and 2D textured videos
625 for 41 subjects. Mahmoud et al. [90] created a 2D texture and depth video database for
626 complex mental states including, in addition to the face, the upper part of the body. In
627 particular, incorporating these latter data in the dataset can help in understanding the
628 complex emotional and affect states.

629 Several works appeared in last few years addressing the spontaneous facial expres-
630 sions classification. In [36], Cruz et al. proposed a bio-inspired approach for spontaneous
631 facial emotion analysis. Authors of this work were motivated by the cognitive principle
632 according to which the human vision system pays more attention to the parts of the
633 scene with the highest dynamics. This approach implemented this principle by unfixed
634 video down-sampling rate. The results confirmed that temporal video down-sampling
635 according to the temporal change is more efficient than uniform rate down-sampling
636 and faster than using the full video frame rate. This method is limited mainly by the
637 influence of the accuracy of the apex labeling on the performance. Abd El Meguid et
638 al. [3] proposed a fully automatic framework for spontaneous facial expressions detection
639 and classification using random forest classifier. This framework works independently
640 of the training dataset, and in unconstrained scenarios with pose and illumination
641 variation, also providing real-time performance. In [103], an aggression detection out

642 of other spontaneous facial expressions framework is presented by PiŃtkowska and
643 Martyna. Senechal et al. [117] present an algorithm to detect spontaneous asymmetric
644 facial expressions, like (smark) out of natural symmetric facial expressions from 2D
645 videos. In [150], Zeng et al. proposed a one-class classification problem to distinguish
646 between emotional facial expressions and non-emotional ones. A kernel subspace method
647 is applied to model the facial expressions with support vector data description classi-
648 fier and validated on Adult Attachment Interview (AAI) database [109]. Kamarol et
649 al. [72] proposed a new spatio-temporal feature extraction method with application to
650 spontaneous facial expressions classification, which outperforms the state of the art
651 feature extraction methods in term of classification rate and computational time. Liu
652 and Yin [82] proposed a new descriptor for spontaneous facial expression analysis, but
653 using thermal video images. More detailed and comprehensive surveys on automatic
654 human affect detection and recognition from facial expressions are available in [25, 114].

655 From this review, one can note **the increasing interest in this research direc-**
656 **tion, recently.** This thesis investigated this problem as it will be presented in Chapter 5.

657 **2.5 Subspace representation for face classification**

658 Subspace representation for dynamic facial information either for image sets or for image
659 sequences (videos) showed a great success in this field of computer vision. Shigenaka
660 et al. [119] proposed a Grassmann distance mutual subspace method (GD-MSM) and
661 Grassmann Kernel Support Vector Machine (GK-SVM) comparison study for the face
662 recognition problem from a mobile 2D video database. In [89], Lui et al. proposed a
663 geodesic distance based algorithm for face recognition from 2D image sets. In this
664 work, they exploited the canonical correlation analysis between two subspaces and
665 used geodesic distance to consider the whole geometry of the subspace in the similarity
666 score. Experiments conducted on 2D face image datasets show better recognition for
667 this approach over others. More recently, Wang et al. [66] proposed learning projection
668 distance on Grassmann manifold for face recognition from image sets. Every image
669 set is represented as a Gaussian distribution over the manifold to model the data
670 overall distribution, not only the image sets information, which results in an improved
671 recognition. Turaga et al. [132] presented a statistical method for video based face
672 recognition. These methods use subspace-based models and tools from Riemannian
673 geometry of the Grassmann manifold. Intrinsic and extrinsic statistics are derived
674 for maximum-likelihood classification applications. In [60], Harandi et al. proposed a

675 Grassmann Discriminant Analysis (GDA) approach, which is an extension of the Linear
676 Discriminant Analysis (LDA) algorithm to work with nonlinear structures. A graph
677 embedding framework is used in this work to build two within-class and between-class
678 similarity graphs, which move the classification problem from non-linear Grassmann
679 manifold into vector linear space. The application of this approach to face recognition
680 and object classification shows good results.

681 From these presented works, the subspace representation of the 2D facial image sets
682 or sequences showed a high performance and robustness against noise, missing data.
683 Besides, it reduced the computational costs of comparing two image sets in many to
684 many scenario and converted it into two low dimensional linear subspaces comparison.
685 All of that, gives us the motivation to explore the performance of subspace representation
686 for modeling 3D dynamic data for the first time.

687 **2.6 Physical pain detection in videos**

688 Physical pain detection and estimation from facial images attracted more attention
689 recently due to its important applications in healthcare systems, clinical treatment
690 especially for people in a coma, under surgery or suffering from speech organs disor-
691 ders. Lucey et al. [85] presented a facial video database (known as UNBC-McMaster
692 Shoulder Pain Expression archive) for people suffering from shoulder pain with action
693 unit coding on the frame level of the video. The same authors extended the work in [86],
694 by proposing an Active Appearance Model (AAM) system that can detect the frame
695 with pain expression out of others in 2D texture videos. A full automatic pain intensity
696 estimation approach from 2D image sequences from UNBC-MacMaster database is
697 presented by Kaltwang et al. [71]. In [74], Khan et al. proposed a new facial descrip-
698 tor called pyramid local binary pattern (PLBP), with application to pain detection on
699 UNBC-Macmaster database. Their approach gives near real-time performance, with
700 high recognition rate. Unlike previously mentioned works, Sikka et al. [122] proposed
701 sequence level spatial-temporal descriptor instead of frame level to exploit the advantage
702 of temporal information in the 2D video in combination with bag-of-words framework.
703 This approach gives better results on MacMaster Shoulder Pain database approving the
704 positive effect of temporal information on recognizing pain.

705 Since the works listed above are based on 2D images, they are affected by pose
706 and illumination variations, which can be solved by moving to 3D imaging systems.
707 Following other facial computer vision problems, pain recognition may be considered

708 in 3D facial databases. In BP4D-Spontaneous 3D dynamic database [152], there is one
709 task of spontaneous physical pain experience for 41 subjects. Zhang et al. [154] proposed
710 a pain-related action units detection on BP4D database using binary edge feature
711 representation. This approach exploits the available temporal information alongside the
712 3D facial scans as well as their robustness against pose variation. A more comprehensive
713 survey on pain detection from facial expressions can be found in [10].

714 From the review above, it emerges the importance of the early detection aspect for
715 several applications, especially computer machine interaction, and **the very limited**
716 **works that addressed this problem for spontaneous facial expression from 3D**
717 **dynamic data. This was the main motivation to orient part of the work in this**
718 **thesis to explore the opportunities and limitations that 3D dynamic data have**
719 **for a such complex scenario.**

720 **2.7 Early event detection in videos**

721 The majority of video analysis methods propose expression classification based on the
722 observation of the entire 3D dynamic sequence (i.e., a decision is taken once the full
723 sequence is observed). In these works, no emphasis is placed on the responsiveness, i.e.,
724 on the capability to produce a correct classification just from a partial observation, as
725 short as possible, of the sequence. This latter capability is indeed expected to be of great
726 relevance to real contexts of application. Studying the trade-off between the accuracy
727 and observation size for rapid recognition is an important topic in a wide spectrum of
728 applications, ranging from video security to clinical treatments. This aspect has been
729 investigated through several studies, in different domains and from different perspectives.
730 Indeed, the trade-off between the accuracy and observation size for rapid recognition is
731 an important topic in a wide spectrum of real applications. Schindler and Van Gool [115],
732 first investigated this aspect by evaluating how many frames were required to enable
733 action classification in RGB-videos. They found that short action snippets with as few
734 as 1–7 frames were almost as informative as the entire video. This aspect has been
735 addressed in few works. Su et al. [126] presented a high-frame-rate 3D facial expressions
736 recognition system, based on an early AdaBoost classifier, but the test dataset was
737 limited to few subjects and the facial expressions were posed, with a very high temporal
738 resolution. The six basic expressions are collected five times for the same person with
739 100 fps as a temporal resolution. The concatenated animations of facial markers position
740 in the 3D space are used as a feature vector after refining them by wavelet spectral

741 subtraction. In [127], Su and Sato proposed an early recognition framework based on
742 RankBoost with application to facial expression recognition. Starting from the fact that
743 the intensity of the facial expression generally increases from the onset to the apex
744 monotonically, this increase is learned by weak rankers in the same temporal order.
745 Applying the weight propagation on the weak rankers, the early recognition system is
746 built. Results are reported on the Cohn-Kanade (CK) 2D video dataset, and on a small
747 3D high temporal resolution dataset of six subjects.

748 More recently, Hoai and De la Torre [63] proposed a learning formulation for early
749 event detection. Their maximum-margin framework is devised for training temporal
750 event detectors capable of recognizing partial events, thus enabling early detection with
751 minimal latency. Their method extends the Structured Output SVM to accommodate
752 sequential data. They showed the effectiveness of the framework for detecting facial
753 expressions, recognizing hand gestures, and classifying human activities from video
754 sequences.

755 **2.8 Dynamic facial datasets**

756 In this section, a comprehensive survey for the spontaneous dynamic 2D and 3D dataset
757 oriented for facial expressions problems will be survey and the most important 3D
758 dynamic (4D) facial analysis datasets.

759 **2.8.1 Spontaneous dynamic facial expression datasets**

760 Facial expressions classification and emotional states detection remained for long-time
761 focusing on acted facial expressions due to the difficulty of collecting and annotating
762 spontaneous and natural facial expression databases. Recently, more attention has been
763 paid to the analysis of spontaneous facial expression and emotion detection. Several
764 databases have been collected for this purpose as reviewed hereafter.

765 The FeedTUM database [137] proposed by Wallhoffet et al. who tried to solve the
766 problem of deliberated facial expression in dynamic databases. So, it gathered the basic
767 six emotions from 18 different individuals. To achieve spontaneous facial expressions,
768 they played video clips or still images after a short introduction phase instead of telling
769 the person to play a role. This includes that head moves in all directions are also
770 allowed. Videos are captured using Sony XC-999P camera that gives images with size of
771 640×480 pixels, a color depth of 24 bits and a frame rate of 25 frames per second. Due

772 to capacity reasons, the images were converted into 8 Bit JPEG-compressed images
773 with a size of 320×240 . The DaFEx database [12] proposed by Battocchi et al. is a
774 database created with the purpose of providing a benchmark for the evaluation of the
775 facial expressibility of Embodied Conversational Agents (ECAs). DaFEx consists of 1008
776 short videos containing emotional facial expressions of the 6 Ekman's emotions plus the
777 neutral expression. The facial expressions were recorded by 8 Italian professional actors
778 (4 male and 4 female) in two acting conditions ("utterance" and "no- utterance") and at 3
779 intensity levels (high, medium, low). For capturing videos, a Canon MV360i was placed
780 on tripod is used. After a post-processing step, final data saved in .avi format yielding
781 a final size on screen of 360×288 pixels. To overcome the challenges of illumination
782 variation in imaging conditions, Wang et al in [139] created NVIE 2D videos, which
783 contain visible and thermal infrared images for natural and posed database for six basic
784 expressions of 100 subjects. Two cameras have been used for this task, a DZ-GX25M 2D
785 visible camera with 30 fps as temporal resolution which gives 704×480 image sizes. A
786 SAT-HY6850 infrared camera with 25 frames per second as temporal resolution, which
787 gives images of size 320×240 and wave band $8 - 14 \mu m$. The LIRIS-ACCEDE database
788 proposed by Baveye et al. in [14] is a large 2D videos database collected from public
789 available films and movies with extensive annotation for affective content analysis. It
790 contains 9,800 clips that last between 8 to 12 seconds extracted from 160 different
791 movies. This database is annotated in Arousal-Valence space by experts and available for
792 public use. The MAHNOB-HCI multimodal database is proposed in [123] by Soleymani
793 et al. It contains facial videos, voice data, eye gaze data and peripheral/central nervous
794 system physiological signals for 27 subjects. Spontaneous emotions induced by showing
795 videos to the participants. Facial visual data captured using two imaging systems, one
796 Allied Vision Stingray F-046C, a color camera, and five Allied Vision Stingray F-046B,
797 monochrome cameras. The temporal resolution for all cameras is 60 fps and the spatial
798 resolution is 780×580 .

799 In [92], Mavadati et al. created a spontaneous action units intensity database called
800 DISFA. There are 27 subjects in this database that were collected using a high-resolution
801 ($1,024 \times 768 pixels$) BumbleBee point gray stereo-vision system at 20 frames per sec-
802 ond under uniform illumination. Action units' intensity levels are annotated using a
803 scale from 0 (action unit not activated) to 5 (maximum intensity) by two FACS expert
804 coder. 66 landmarks were annotated using an Active Appearance Model (AAM) method.
805 In [93], Mckeown collected an audio-visual database, SEMAINE, for spontaneous ef-
806 fective states by interaction between an operator and the participant consisted of 20

807 subjects. The operator plays four different roles to evoke four different emotional states
808 for the participants. A high-resolution imaging system is used, which consists of five
809 synchronized cameras that record by 50 fps as temporal resolution and 780×580 as
810 spatial resolution. Annotation is made on five dimensions – Valence, Activation, Power,
811 Anticipation/Expectation – with the addition of Overall Emotional Intensity. SMIC is a
812 spontaneous micro-expression database proposed in [80] by Xiaobai et al. It contains 164
813 micro-expression 2D video clips that belongs to 16 subjects which can be a benchmark for
814 micro-expressions detection and recognition approaches. 16 movies are used to induce
815 the spontaneous emotions of the participants. A high speed (HS) camera (PixeLINK
816 PL-B774U, 640×480) of 100 fps was used to collect the database in addition to another
817 normal speed 25 fps imaging system, which consists of a normal visual camera and a
818 near infrared camera of spatial resolution 640×480 both.

819 Within the efforts dedicated to bring spontaneous facial expressions from 2D into 3D,
820 new databases started to appear recently considering this aspect. Mahmoud et al. in [90]
821 collected a set of 108 audio/video segments of natural complex mental states of 7 subjects.
822 Each video is acquired with the Kinect camera, including both the appearance (RGB)
823 and depth information. The data capture natural facial expressions and the accompanied
824 hand gestures. The emotional states are: Agreeing, Bored, Disagreeing, Disgusted, Excite,
825 Happy, Interested, Sad, Surprised, Thinking and Unsure. This database was collected
826 using two cameras: the HD cameras provide 720×576 pixel resolution color images
827 at 25 fps and the Kinect sensor provides a color image and a disparity map, which
828 is the inverse of depth values, at 30 fps. In [7], depth spontaneous facial expressions
829 VT-KFER database is proposed for acted and spontaneous facial expressions. It includes
830 7 expressions, which are happiness, sadness, surprise, disgust, fear, anger, and neutral
831 for 32 subjects. A set of 121 automatically detected facial landmarks is provided with
832 the depth frames with their correspondence on 2D texture images. The Microsoft Kinect
833 camera was used in the acquisition.

834 From works summarized in Table 2.1, we can notice the increasing interest is moving
835 from acted facial expressions and action units into the spontaneous ones, which are
836 closer to real world scenarios, but more challenging for automatic recognition and
837 detection. Also, most of the works induced the spontaneous emotions by showing specific
838 videos in front of the participants, other techniques hiring professional actors, taking
839 videos from movies or making interaction with an operator. Most recently, **spontaneous**
840 **facial emotion analysis brought into 3D domain** by collecting depth and 3D high-
841 resolution spontaneous datasets.

Table 2.1: Overview of spontaneous facial expressions and action units datasets.

Reference	# Subject	Type	Imaging Systems	Purpose
FeedTUM [137]	18	2D video	Sony XC-999P	FER
DaFEx [12]	8 actors	2D video	Canon MV360i	FER
NVIE [139]	100	2D video/ Infrared	DZ-GX25M / HY6850	FER
LIRIS-ACCEDE [14]	NA	2D video	from movies	FER
MAHNOB-HCI [123]	27	2D video	Vision Stingray F-046C	FER
DISFA [92]	27	2D video	BumbleBee stereo-vision	Aus
SEMAINE [93]	20	2D video	Color and Gray cameras	FER
SMIC [80]	16	2D video	HS PixeLINK PL-B774U / Near Infrared camara	Micro FER
Depth Corpus [90]	7	2D video/ Depth	HD cameras / MS Kinect 1.0	ESR
VT-KFER [7]	32	2D video/ Depth	MS Kinect 1.0	FER
BP4D [152]	41	3D video/ 2D video	Di3D system	FER/ AUs

842 2.8.2 3D dynamic facial databases

843 In recent years, several facial 3D dynamic databases have been introduced to analyze
844 the dynamic nature of human faces, mainly for expression/emotion and action units
845 recognition. The BU-4DFE dataset, collected by Yin et al. [148] consists of 4D faces
846 (sequences of 3D faces). The database included 101 subjects and was created using
847 the Di4D (Dimensional Imaging) passive stereo-photogrammetry imaging system. It
848 contains sequences of the six prototypical facial expressions with their temporal segments
849 (neutral-onset-apex-offset-neutral) with each sequence lasting approximately 4 seconds.
850 The temporal and spatial resolution is 25 fps and 35,000 vertices, respectively. The
851 main limits of this database are that it contains posed facial expressions, and restricted
852 acquisition environment (well-controlled illumination and frontal view of the subject's
853 face), which makes it far from real scenarios. Cosker et al. [35] presented the first
854 database that contains coded examples of dynamic 3D Action Units (AUs) in D3DFACS.
855 There are 10 subjects in this dataset, including 4 FACS experts, and they were asked to
856 perform 38 AUs in various combinations. Totally, there are 519 AUs sessions at 60 fps as
857 temporal resolution. Each action unit consisting of 90 frames approximately. An FACS
858 expert coded the peak of each sequence. It is more oriented for AUs recognition, captured
859 under highly conditioned framework with posed facial expressions, too. The Hi4D-ADSIP

Table 2.2: Comparison of existing 4D Face databases.

Database	# Subjects	Temporal Resolution	Spatial Resolution	Illumination condition	Pose variation
Bu4DFE: [148]	101	25 fps	35k	Controlled	Limited
BP4D-Spon: [155]	41	25 fps	40k	Controlled	Limited
D3DFACS: [35]	10	60 fps	30k	Controlled	No
Hi4DADSIP:[91]	80	60 fps	20k	Controlled	Limited

860 database, presented by Matuszewski et al. in [91] is a 3D dynamic facial database,
 861 which contains facial articulation. Both, the temporal resolution, 60 fps, and the spatial
 862 resolution, 2352×1728 pixels per frame, are highly recorded using the Di4D system. In
 863 total, there are 80 subjects in this dataset with 3360 sequences. Subjects have various
 864 age, gender and race. The seven basic facial expressions are included with seven facial
 865 articulations. The main reason to include these articulations is to support the clinical
 866 research on facial dysfunctions. The facial expression recognition algorithm was applied
 867 to validate the part of the database containing standard facial expressions. Two different
 868 algorithms in static and dynamic mode are applied. In addition, a psycho-physical
 869 experiment that was used to formally evaluate the accuracy of recorded expressions is
 870 conducted. Where the first dataset is publicly available, the two last ones are private.

871 Finally, Zhang et al. [155] have created a high-resolution spontaneous 3D dynamic
 872 facial expression Database, called BP4D-Spontaneous. Also, for this dataset, the Di4D
 873 system was used for the acquisition, but the expressions are not posed; instead they are
 874 spontaneously conveyed by the participants. Expressions include happiness or amuse-
 875 ment, sadness, surprise, embarrassment, fear or nervous, physical pain, anger or upset
 876 and disgust. There are 41 participants in this database. For each subject, 3D and 2D
 877 videos lasting about 1 minute for each scenario are captured. Manually annotated action
 878 units (FACS AU) by a certified FACS coders, automatically tracked facial landmarks
 879 and head pose in 3D/2D videos are provided with the database. Table 2.2 presents a
 880 comparison between existing dynamic 3D face datasets and the dynamic part of our
 881 3D-4D database.

882 From this summary, one can note the following points – the great recent interest of
 883 the community in facial analysis from **dynamic data** is motivated by the importance of
 884 the new dimension (time) for better understanding of facial expressions, emotions and
 885 action units; Most of these datasets are designed for **facial expressions and/or action**
 886 **units** problem and do not address face recognition.

887 **2.9 Conclusion**

888 In this chapter, we have reviewed prior work to facial analysis from dynamic data, in
889 particular for two applications – face recognition and emotion classification. A taxonomy
890 of current literature is first presented, then a set of papers have been discussed in each
891 category. From this review, one can first note the novelty of the topic – exploiting 4D
892 data for face understanding. Only very few research groups have made advanced studies
893 and have confirmed the interest of using sequences of 3D facial shapes instead of video
894 data. However, the proposed approaches are computationally expensive in general and
895 often need 3D landmarks annotation and tracking. The most promising representations
896 and methodologies are derived from 3D (static) approaches, such that template fitting
897 and non-rigid registration, which are time-consuming and sensitive to noisy and missing
898 data. The above-mentioned challenges have motivated us, in this thesis, to focus on
899 representations suitable for dynamic data based on subspace methods as a first modeling
900 level. In a next level, two major representations based on **dictionaries** and **trajectories**
901 are proposed for dictionary learning and sequential analysis, respectively.

902 In the next chapter, we shall introduce essential mathematical materials of Grass-
903 mann manifolds and computational tools needed to introduce our contributions.

GEOMETRIC FRAMEWORK FOR MODELING 3D FACIAL SEQUENCES

3.1 Introduction

904 From the previous chapter, one can note the important aspects and motivations, which
905 lie behind our choice to work on 3D dynamic facial sequences for face recognition and
906 early detection of spontaneous emotional states and affects. Inside, the very first and
907 important question, which needs to be answered is – **Which representations of static
908 and dynamic shapes are more suitable to study such problems?**

909 In this chapter, we start presenting the dynamic 3D data and the subspace represen-
910 tation adopted in our solutions. In Sect. 3.2, we introduce the subspace representation
911 and why it is selected in this work. The notation of Grassmann manifold is given with
912 the definitions of several distances and metrics in Sect. 3.3. Sect. 3.4 presents statistical
913 learning algorithms that are very important to manipulate and classify the original dy-
914 namic data from the subspace representation. The dynamic representing of 3D sequences
915 as trajectories on Grassmann and Stiefel manifolds and how to model spatio-temporal
916 information from these trajectories using distances and velocity vectors are presented in
917 Sect. 3.5. Finally, we conclude the chapter in Sect. 3.6.

918 3.2 Which data of interest?

919 In Fig. 3.1, we show an example of 3D sequence acquired by a single-view structured-light
 920 3D scanner with a large field-of-view. One can appreciate the deformations of the 3D
 921 scan over time. In addition, the frames present different poses of the body, and include
 922 undesirable parts, such as the neck, the shoulders, etc.

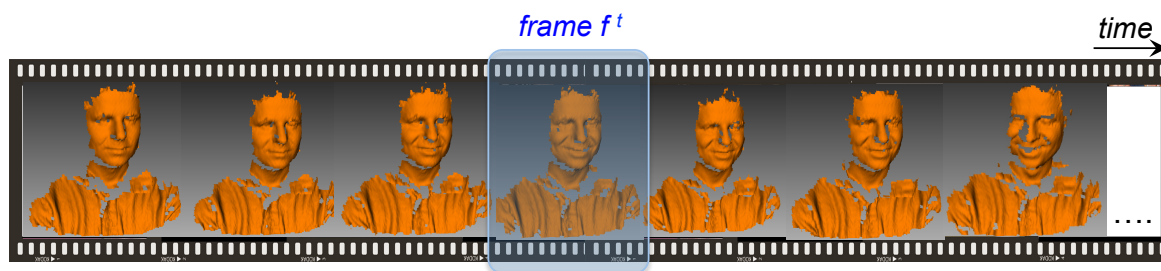


Figure 3.1: Equally-spaced 3D frames of a sample dynamic facial sequence (of the author) conveying a happiness expression. The sequence shows some challenges, such as pose variations, incomplete data and noise.

923 Actually, from the state-of-the-art, we note the two main categories to model 4D
 924 facial scans are: First, 3D feature tracking, which depends basically on the accuracy
 925 of detecting landmarks through the video; Second, the 3D deformation of facial scans
 926 by comparison with reference model or another scan. These two methodologies can be
 927 affected badly when applying them on noisy 3D facial data captured under unconstrained
 928 scenarios. Starting from this point and encouraged by the results achieved in 2D dynamic
 929 facial analysis, we decided to use the subspace representation to model 3D videos in
 930 this work. The compactness of this representation derives from projecting the high
 931 dimensional data in low-dimensional representation while keeping the informative part,
 932 being able at the same time of discarding noise and compensate missing data. If needed,
 933 one can come back from the new compact representation into the original data due to its
 934 faithfulness.

935 Now, let us consider two 3D facial videos V_1, V_2 , we want to know for example if they
 936 belong to the same person class (for identity recognition) or they convey the same emotion
 937 (facial expression recognition). The main question here is: **How can we measure the**
 938 **similarity between these two videos?** This similarity measure is the first step for
 939 going further toward classification and statistical learning algorithms. By modeling these
 940 two videos as k dimensional linear subspaces \mathcal{X}, \mathcal{Y} on \mathbb{R}^n , these subspaces lie naturally

941 in space of linear subspaces, which is a special Riemannian manifold called Grassmann
942 manifold. Over this non-flat manifold, the length of the shortest path between two
943 elements (subspaces) is well defined as a geodesic distance. Several techniques have
944 been developed in the literature in order to find a linear projection of high-dimensional
945 data into a lower finite dimension linear subspace. The main motivation for adopting
946 this representation is its ability to reveal a hidden principle structure of the raw data,
947 compensating for missing parts and discarding noise. Principle Component Analysis
948 (PCA) [68] is one of the most common approaches for dimensionality reduction, and it
949 has been used early for face recognition in the *Eigenfaces* approach [133]. Another data
950 reduction technique related to PCA is the Singular Value Decomposition (SVD). SVD is
951 often used when the informative data are more related to the global structure than the
952 variation, so keeping the mean can be meaningful in these cases whereas it is removed
953 in PCA method.

954 A great interest has been paid recently to matrix manifolds and their use to solve com-
955 puter vision problems [88]. Advanced mathematical and statistical learning algorithms
956 have been already defined on these manifolds. Learning approaches solved the problem of
957 non-linearity representation by intrinsic methods that start from the fact these manifolds
958 have a linear structure locally [132] or extrinsic approaches that embed the non-linear
959 manifold into another manifold with a linear structure [59]. The principle of modeling
960 real world data in low-dimensional linear subspaces approved its efficiency in numerous
961 applications, like object recognition from image sets and videos [132], spatio-temporal
962 dynamic system representation [9], image analysis and filtering [134], object tracking
963 [84], etc. More recently, several learning approaches on manifold appeared that address
964 the spatio-dynamic modeling as a trajectory on the manifold, which showed efficient
965 performance on several computer vision applications, like in action classification [9, 16].
966 The ability to represent a sequence of subspaces as a parameterized trajectory by the
967 time can be an excellent solution for emotional states and complex affects detection from
968 3D dynamic data.

969 **3.3 Geometry of Grassmann manifolds**

970 The Riemannian manifold by definition is a nonlinear topological structure that has a
971 Euclidean space property locally with a defined metric that can give a similarity measure
972 between two elements on the manifold. Let us have two sets of points A and B in one
973 space, and the relation between their elements is equivalence, i.e., every certain set of

974 points from set A is equivalent to one specific point in set B . This relation defines the
 975 group B as a quotient of group A . Following this quotient principle, the geometry of
 976 Stiefel $\mathcal{L}_k(\mathbb{R}^n)$ and Grassmann $\mathcal{G}_k(\mathbb{R}^n)$ manifolds will be presented as a quotients of the
 977 special orthogonal group $SO(n)$.

978 3.3.1 Special orthogonal group

979 The generalized linear group $GL(n)$ of $n \times n$ non-singular matrices forms a differentiable
 980 manifold. Even though the differentiable manifold is not a vector space, it can be consid-
 981 ered subsets of Euclidean space locally. Later, we will see the importance of this property
 982 of local linearity for adapting the Euclidean mathematical and statistical tools to these
 983 manifolds. Since the $GL(n)$ is a differentiable manifold and a group at the same time, it
 984 forms a Lie Group $LG(n)$. The Special Orthogonal Group $SO(n)$ obtained by considering
 985 the subset of orthogonal matrices with determinant $+1$. Thus, $SO(n)$ is a submanifold of
 986 $LG(n)$ and keeps Lie Group structure.

The first step towards doing differential calculus on a manifold is to specify the tangent space. For the identity matrix I , which is an element of $SO(n)$, the tangent space $T_I(SO(n))$ is the set of all $n \times n$ skew-symmetric matrices given by:

$$(3.1) \quad T_I(SO(n)) = \{X \in \mathbb{R}^{n \times n} \mid X + X^T = 0\}.$$

Definition 3.3.1. The *Tangent Space* $T_O(SO(n))$ at any point $O \in SO(n)$ is a rotation of the identity matrix tangent space $T_I(SO(n))$, and it is given formally as:

$$(3.2) \quad T_O(SO(n)) = \{OX \mid X \in T_I(SO(n))\}.$$

987 After defining the tangent space, let us define an inner product for any $X, Y \in$
 988 $T_O(SO(n))$ where $\langle X, Y \rangle = tr(XY^T)$ and tr is the sum of the diagonal elements in
 989 the matrix, the group $SO(n)$ becomes a Riemannian manifold. Starting from the bi-
 990 invariant Riemannian structure obtained, it is possible to measure the length of paths
 991 on a manifold.

Definition 3.3.2. Let us have two points $O_1, O_2 \in SO(n)$, the *Riemannian Metric* between these two points can be defined as the infimum of the length of all smooth paths on $SO(n)$, which has O_1 as a beginning and O_2 as an end given by:

$$(3.3) \quad d(O_1, O_2) = \inf_{\{\alpha: [0,1] \rightarrow SO(n) \mid \alpha(0)=O_1, \alpha(1)=O_2\}} \int_0^1 \sqrt{\left\langle \frac{d\alpha(t)}{dt}, \frac{d\alpha(t)}{dt} \right\rangle} dt.$$

992 The path $\hat{\alpha}$, which achieves the above minimum is a geodesic between O_1 and O_2
 993 on $SO(n)$. This geodesic can be computed from the matrix exponential as well. It is
 994 important to highlight that the geodesic here is a constant speed curve defined by its
 995 initial velocity and it is different from the geodesic distance, which is a Riemannian
 996 distance between two points on the Grassmann manifold.

Definition 3.3.3. Let us have a matrix A of size $n \times n$, the *Matrix Exponential* of A
 $\exp(A)$ can be computed as follows:

$$(3.4) \quad \exp(A) = I + \frac{A}{1!} + \frac{A^2}{2!} + \frac{A^3}{3!} + \dots$$

997 Starting from this equation, it is possible to define geodesics on $SO(n)$ as follows:
 998 Let us have an orthonormal matrix $O \in SO(n)$ and any skew-symmetric matrix X ,
 999 $\alpha(t) = O \exp(tX)$ is the unique geodesic in $SO(n)$ passing through O with velocity vector
 1000 OX at $t = 0$.

1001 The exponential map is very important for statistics on the manifold, because it
 1002 allows moving a point from the tangent space to the manifold.

Definition 3.3.4. If M is a Riemannian manifold and $p \in M$, the *Exponential Map*
 $\exp_p : T_p(M) \rightarrow M$, is defined by $\exp_p(v) = \alpha_v(1)$, where α_v is a geodesic starting at p . In
 the case of $SO(n)$, the exponential map $\exp_O : T_O(SO(n)) \rightarrow SO(n)$ is given by:

$$(3.5) \quad \exp_O(X) = O \exp(X),$$

1003 where the exponential map of O is the multiplication between O and its matrix exponen-
 1004 tial.

1005 3.3.2 Stiefel manifold

1006 **Definition 3.3.5.** *Stiefel manifold* is a set of k -dimensional orthonormal bases in \mathbb{R}^n
 1007 where $1 \leq k \leq n$.

Since every basis is represented by a matrix of size $n \times k$ with orthonormal columns,
 this set can be seen as a quotient space of $SO(n)$ as follows: We can consider $SO(n - k)$
 as a subgroup with smaller rotations on $SO(n)$ by defining an embedding function
 $\phi_1 : SO(n - k) \rightarrow SO(n)$ as:

$$(3.6) \quad \phi_1(W) = \begin{bmatrix} I_k & 0 \\ 0 & W \end{bmatrix} \in SO(n).$$

Now, we consider $O_1, O_2 \in SO(n)$ to be equivalent, i.e., $O_1 \sim O_2$, if $O_1 = O_2 \phi_1(W)$ for some $W \in SO(n-k)$, where $\phi_1(SO(n-k))$ represents the rotations of $SO(n)$, which rotates only the last $(n-k)$ components in \mathbb{R}^n and keeping the first (k) without any rotation. Thus, we defined a new equivalence relation between orthogonal matrices of size $n \times n$, where they are identical if the first k columns are identical regardless of the rest $(n-k)$ columns, and this class is given by:

$$(3.7) \quad [O]_\alpha = \{O\phi_1(W) \mid W \in SO(n-k)\}.$$

Since all $[O]_\alpha$ have the same k first columns, we represent all elements of $[O]_\alpha$ by one submatrix $U \in \mathbb{R}^{n \times k}$. So, **Stiefel manifold** of dimension k is the set of these equivalence elements, i.e., a quotient space of the Special Orthogonal group $SO(n)$ and it is given simply by:

$$(3.8) \quad \mathcal{L}_k(\mathbb{R}^n) = SO(n)/SO(n-k).$$

Definition 3.3.6. One possibility to define a *Stiefel metric* between two elements of this manifold is given by the Frobenius norm. Consider two elements of Stiefel manifold $X, Y \in \mathcal{L}_k(\mathbb{R}^n)$. The *Frobenius metric* is defined by:

$$(3.9) \quad d_{stiefel}(X, Y) = \|X - Y\|_F$$

1008 where $\|\cdot\|_F$ is the standard Frobenius norm, where $\|A\|_F = \sqrt{\text{tr}(AA^t)}$.

1009 3.3.3 Grassmann manifolds

1010 **Definition 3.3.7.** The *Grassmann manifold* is the set of all k -dimensional subspaces
 1011 of \mathbb{R}^n . Since that every $n \times k$ orthonormal matrix and all its rotations on $SO(n)$, that
 1012 make different element of Stiefel manifold, represent the same subspace on Grassmann
 1013 manifold.

To define a structure of quotient space for Stiefel manifold $\mathcal{L}_k(\mathbb{R}^n)$, let us consider $S(k) \times S(n-k)$ as a subgroup of $SO(n)$ defined by the function $\phi_2 : (SO(k) \times SO(n-k)) \rightarrow SO(n)$ as:

$$(3.10) \quad \phi_2(W_1, W_2) = \begin{bmatrix} W_1 & 0 \\ 0 & W_2 \end{bmatrix} \in SO(n).$$

$O_1 \sim O_2$ if $O_1 = O_2 \phi_2(W_1, W_2)$ for some $W_1 \in SO(k)$ and $W_2 \in SO(n-k)$ O_1 and O_2 are equivalent if the first k columns of O_1 are rotations of the first k columns of O_2 and the

same for the rest $(n - k)$ columns. An equivalence class is given by:

$$(3.11) \quad [O]_\beta = \{O\phi_2(W_1, W_2) \mid W_1 \in SO(k), W_2 \in SO(n - k)\}.$$

Then, the set of all these equivalence classes form the Grassmann manifold $\mathcal{G}_k(\mathbb{R}^n)$ and it can be given formally as a quotient space of Special Orthogonal Group $SO(n)$:

$$(3.12) \quad \mathcal{G}_k(\mathbb{R}^n) = SO(n)/(SO(k) \times SO(n - k)).$$

Consequently, it is a quotient space of Stiefel manifold $\mathcal{L}_k(\mathbb{R}^n)$:

$$(3.13) \quad \mathcal{G}_k(\mathbb{R}^n) = \mathcal{L}_k(\mathbb{R}^n)/SO(k).$$

1014 From this definition for the Grassmann manifold, our adopted representation of
 1015 the 3D dynamic facial sequence of m frames lies naturally on these two manifolds.
 1016 This achieved after applying dimension-reduction technique on the original data, like
 1017 k -singular value decomposition ($k - SVD$).

1018 The main motivation for dealing with Grassmann manifold as a quotient space of
 1019 the special orthogonal group $SO(n)$ is that it allows us to inherit systematically the well
 1020 defined geodesics and tangent planes of the $SO(n)$.

1021 **Definition 3.3.8.** The *Tangent Space* of a Grassmann manifold $\mathcal{G}_k(\mathbb{R}^n)$ can be induced
 1022 directly from the tangent space of the $SO(n)$ since it is a quotient space of it as follows:

1023 Let us have M/L as a quotient space of M under the action of a group $L \subset M$. Now,
 1024 for any point $p \in M$, a vector $v \in T_p(M)$ can be considered as tangent to M/L , since it
 1025 is perpendicular to the tangent space $T_p(pL)$ where $T_p(pL)$ is a subspace of $T_p(M)$.
 1026 Following the same principle, we define the tangent space of $\mathcal{G}_k(\mathbb{R}^n)$, while $M = SO(n)$
 1027 and $L = \phi_2(SO(k) \times SO(n - k))$ with ϕ_2 given in Eq. 3.10.

The tangent space $T_I(L)$ is considered as a subspace of $T_I(SO(n))$ by defining the embedding function ϕ_T :

$$(3.14) \quad \phi_T(A_1, A_2) = \begin{bmatrix} A_1 & 0 \\ 0 & A_2 \end{bmatrix} \in T_I(SO(n)).$$

The tangent vectors to $SO(n)$ and perpendicular to the space $(T_{I_k}(SO(k)) \times T_{I_{(n-k)}(SO(n-k))})$ can be considered the tangent of $\mathcal{G}_k(\mathbb{R}^n)$ after multiplication on right by matrix $J \in \mathbb{R}^{n \times k}$, which includes the first k columns of $I_n \in \mathbb{R}^{n \times n}$. The tangent space at $[J]$ is given by:

$$(3.15) \quad T_{[J]} = \left\{ \begin{bmatrix} 0 \\ B^T \end{bmatrix} \mid B \in \mathbb{R}^{k \times (n-k)} \right\}$$

If we have $[U] \in \mathcal{G}_k(\mathbb{R}^n)$, and $O \in SO(n)$, then $U = O^T J$. The tangent space at $[U]$ is given by:

$$(3.16) \quad T_{[U]}(\mathcal{G}_d(\mathbb{R}^n)) = \{O^T G \mid G \in T_{[J]}(\mathcal{G}_k(\mathbb{R}^n))\}$$

1028 3.3.4 Exponential and logarithm map on Grassmann manifolds

1029 Since the Grassmann manifold is a quotient space of special orthogonal group $SO(n)$, it
 1030 inherits the definition of exponential map that projects a point from the manifold into the
 1031 tangent vector space and its inverse, the logarithm map, that returns the point from the
 1032 tangent space to the manifold. These two algorithms are essentials to solve statistical
 1033 learning and optimization problems on Grassmann manifold by intrinsic manner. In
 1034 [50], Gallivan et al. presented efficient computational methods to implement these two
 1035 algorithms.

1036 **Definition 3.3.9.** Let us have two subspaces $\mathcal{X}_1, \mathcal{X}_2 \in \mathcal{G}_k(\mathbb{R}^n)$ represented by two matri-
 1037 ces X_1, X_2 of size $n \times k$. We need a method to calculate the velocity parameter V that
 1038 travels from \mathcal{X}_1 to \mathcal{X}_2 in the unit time called the *velocity matrix*.

1039 The algorithm proposed by Gallivan et al. in [50] to compute this structure is given
 1040 by:

1041 1. Compute the $n \times n$ orthogonal completion Q of X_1 .

1042 2. Compute the thin decomposition of $Q^T X_2$ given by:

$$1043 \quad Q^T X_2 = \begin{bmatrix} Y_1 \\ Y_2 \end{bmatrix} = \begin{bmatrix} M_1 & 0 \\ 0 & M_2 \end{bmatrix} = \begin{bmatrix} \Gamma(1) \\ \Sigma(1) \end{bmatrix} V_1^T.$$

1044 3. Compute the angles given by the *arcsin* and *arccos* of the diagonal elements of Γ
 1045 and Σ respectively. Form the diagonal matrix Θ containing θ s on its diagonal,

1046 4. Compute $V = M_2 \Theta M_1$.

1047 **Definition 3.3.10.** Let us have a $\mathcal{X} \in \mathcal{G}_k(\mathbb{R}^n)$, which is represented by an orthogonal
 1048 matrix X of size $n \times k$ with a direction matrix $A \in \mathbb{R}^{(n-k) \times k}$ that gives the direction
 1049 of the geodesic flow. The geodesic path $\beta(t)$ of X at each time instance (t) is given by:
 1050 $\beta(t) = Q \exp(tA) J$ Where $Q \in SO(n)$ and $Q^T X = J$ and $J = [I_k; O_{n-k,k}]$ called a *moving*
 1051 *geodesic*.

1052 The main steps to sample the geodesic path $\beta(t)$ presented in [50] are:

- 1053 1. computing the completion matrix of X , Q of size $n \times n$ by QR decomposition of X .
- 1054 2. Apply SVD to decompose the direction matrix $A = USV^T$.
- 1055 3. Compute the diagonal matrices $\Gamma(t)$ and $\Sigma(t)$ of size $k \times k$ from diagonal elements of
- 1056 S , such that $\gamma_i(t) = \cos(t\theta_i)$ and $\sigma_i(t) = \sin(t\theta_i)$, where Θ is the diagonal elements
- 1057 of S (the principle angles).
- 1058 4. $\beta(t) = \begin{bmatrix} U\Gamma(t) \\ -V^T\Sigma(t) \end{bmatrix}$ for various values of $t \in [0, 1]$.

To illustrate these algorithms on Grassmann, let us have μ as an element of $\mathcal{G}_k(\mathbb{R}^n)$, the tangent space defined on the manifold at this point is T_μ . Using the logarithm map, we can project point $X_1 \in \mathcal{G}_k(\mathbb{R}^n)$ to the vector space T_μ to have V_1 tangent vector. This operation can be defined as:

$$(3.17) \quad \log_\mu : \mathcal{G}_k(\mathbb{R}^n) \rightarrow T_\mu(\mathcal{G}_k(\mathbb{R}^n))$$

Also, we can project V_2 from the vector space to the Grassmann manifold to have X_2 element using the inverse operation (exponential map), which is given by:

$$(3.18) \quad \exp_\mu : T_\mu(\mathcal{G}_k(\mathbb{R}^n)) \rightarrow \mathcal{G}_k(\mathbb{R}^n)$$

1059 Fig. 3.2 depicts these ideas on the Grassmann manifold.

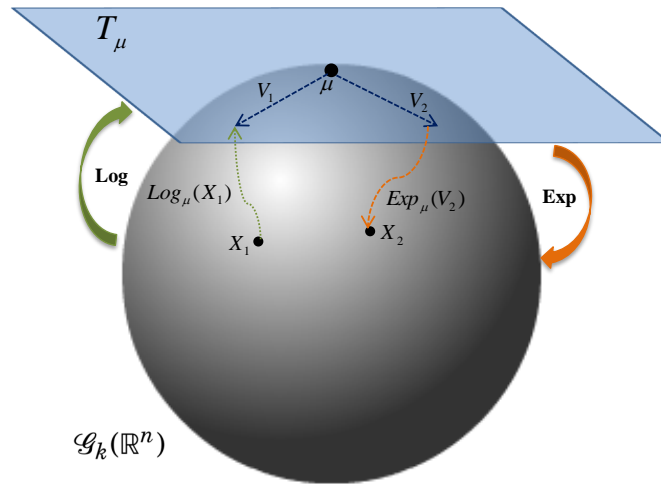


Figure 3.2: Illustration of a tangent plane at point μ and tangent vectors with their map to the Grassmann manifold with Exponential and Logarithm map functions.

1060 **3.3.5 Distances on Grassmann manifolds**

1061 The idea of using the Grassmann manifold representation is that a subsequence of 3D
 1062 or depth scans can be cast to a matrix representation, and thus mapped to a unique
 1063 point on the manifold. In this way, computing the similarity between two subsequences
 1064 is transformed to the problem of computing a Riemannian distance between two points
 1065 on the manifold.

1066 It is important to differentiate between *distance* and *metric* terms on Grassmann.
 1067 The term *distance* is used to refer to similarity measure between two subspaces, which
 1068 has a non-negative value and invariant to any rotation of the subspace basis.

1069 **Definition 3.3.11.** Let us have a function $d : \mathcal{G}_k(\mathbb{R}^n) \times \mathcal{G}_k(\mathbb{R}^n) \rightarrow \mathbb{R}$, d is a *Grassmann*
 1070 *Distance* if $d(\mathcal{X}, \mathcal{Y}) = d(\mathcal{X}R_1, \mathcal{Y}R_2)$, $\forall R_1, R_2 \in SO(k)$.

1071 The *metric* is a distance, but it should satisfy the following conditions for any
 1072 $\mathcal{X}_1, \mathcal{X}_2, \mathcal{X}_3 \in \mathcal{G}_k(\mathbb{R}^n)$

- 1073 1. $d(\mathcal{X}_1, \mathcal{X}_2) \geq 0$,
- 1074 2. $d(\mathcal{X}_1, \mathcal{X}_2) = 0$ if and only if $\mathcal{X}_1 = \mathcal{X}_2$,
- 1075 3. $d(\mathcal{X}_1, \mathcal{X}_2) = d(\mathcal{X}_2, \mathcal{X}_1)$,
- 1076 4. $d(\mathcal{X}_1, \mathcal{X}_2) \leq d(\mathcal{X}_2, \mathcal{X}_3) + d(\mathcal{X}_1, \mathcal{X}_3)$.

1077 More specifically, let \mathcal{X}, \mathcal{Y} denote a pair of subspaces of dimension k on $\mathcal{G}_k(\mathbb{R}^n)$. The
 1078 Riemannian distance between \mathcal{X} and \mathcal{Y} is the length of the shortest path connecting
 1079 the two points on the manifold (i.e., the geodesic distance). The problem of computing
 1080 this distance can be solved using the notion of *Principle Angles or Canonical Correlation*,
 1081 introduced by Golub and Loan [52] as an intuitive and computationally efficient way for
 1082 defining the distance between two linear subspaces.

In fact, there is a set of principal angles $\Theta = [\theta_1, \dots, \theta_k]$ ($0 \leq \theta_1, \dots, \theta_k \leq \pi/2$), between the subspaces \mathcal{X} and \mathcal{Y} (see Fig. 3.3), recursively defined as follows:

$$(3.19) \quad \theta_k = \cos^{-1} \left(\max_{u_k \in \mathcal{X}} \max_{v_k \in \mathcal{Y}} \langle u_k^T, v_k \rangle \right),$$

1083 where u_k and v_k are the vectors of the basis spanning, respectively, the subspaces \mathcal{X}
 1084 and \mathcal{Y} , subject to the additional constraints: $\langle u_k^T, u_k \rangle = \langle v_k^T, v_k \rangle = 1$, being $\langle \cdot, \cdot \rangle$ the inner
 1085 product in \mathbb{R}^n ; and $\langle u_k^T, u_i \rangle = \langle v_k^T, v_i \rangle = 0$ ($\forall k, i : k \neq i$).

1086

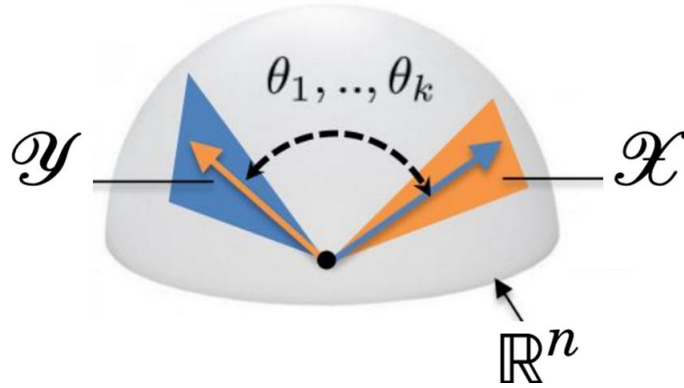


Figure 3.3: Principal angles $\Theta = [\theta_1, \dots, \theta_k]$ computed between two linear subspaces \mathcal{X} and \mathcal{Y} of the Grassmannian $\mathcal{G}_k(\mathbb{R}^n)$.

In other words, the first principal angle θ_1 is the smallest angle between all pairs of unit basis vectors in the two subspaces and the *cosine* of the first principle angles is the first canonical correlation. The k^{th} principal angle and canonical correlation are defined in a similar manner. Based on the definition of the principal angles, the geodesic distance between \mathcal{X} and \mathcal{Y} can be defined as [42]:

$$(3.20) \quad d_{Geo}^2(\mathcal{X}, \mathcal{Y}) = \|\Theta\|_2 = \sum_i^k \theta_i^2.$$

Accordingly, the geodesic distance could be interpreted as the magnitude of the smallest rotation that takes \mathcal{X} to \mathcal{Y} . Given the matrices X, Y , where $\mathcal{X} = \text{Span}(X)$ and $\mathcal{Y} = \text{Span}(Y)$, the principle angles can be computed by applying SVD on the matrix $X^T Y$ as follows:

$$(3.21) \quad X^T Y = \mathcal{U}(\cos \Theta)\mathcal{V}^T,$$

1087 where $\mathcal{U} = [u_1, \dots, u_k]$, $\mathcal{V} = [v_1, \dots, v_k]$, and $\cos \Theta = \text{diag}(\cos \theta_1, \dots, \cos \theta_k)$. The principle
 1088 angles are ordered in non-decreasing form as follows:

$$0 \leq \theta_1 \leq \dots \leq \theta_k \leq \pi/2.$$

1089 consequently, the canonical correlation is in non-increasing order:

$$1 \geq \cos \theta_1 \geq \dots \geq \cos \theta_k \geq 0.$$

1090 This distance is used to measure the similarity between two linear subspaces, even
 1091 though with two different dimensions, permitting to smooth the effect of noisy data, at
 1092 the same time showing robustness with respect to acquisition variations.

1093 Based on the notion of principle angles, several other distances and metrics on the
 1094 Grassmann manifold were proposed in the literature. The most used distances and
 1095 metrics are given below with a discussion about their different geometrical meaning.

Projection metric: It is defined as the l_2 norm of sin of the principle angles between two subspaces:

$$(3.22) \quad d_{proj}^2(\mathcal{X}, \mathcal{Y}) = \sum_{i=1}^k \sin(\theta_i)^2 = k - \sum_{i=1}^k \cos^2(\theta_i).$$

This distance can be computed easily from the product of $X^T Y$. From equation.3.21, the relation between SVD and $X^T Y$ we can get:

$$(3.23) \quad d_{proj}^2(\mathcal{X}, \mathcal{Y}) = k - \sum_{i=1}^k \cos^2(\theta_i) = k - \|X^T X - Y^T Y\|_F^2,$$

1096 where $\|\cdot\|_F^2$ is the Frobenius norm on the matrix.

1097 This Projection distance is a Grassmann distance because it is invariant to different
1098 representations and it is a metric as well.

1099

Binet-Cauchy distance: It is defined as a function of the product of canonical correlations:

$$(3.24) \quad d_{BC}(\mathcal{X}, \mathcal{Y}) = (1 - \prod_i^k \cos^2 \theta_i)^{1/2}.$$

It is computed from from the SVD of $X^T Y$ as:

$$(3.25) \quad d_{BC}^2(\mathcal{X}, \mathcal{Y}) = 1 - \prod_i^k \cos^2 \theta_i = 1 - \det(X^T Y)^2,$$

1100 This distance is a Grassmann distance and a metric as well.

1101

Max Correlation: It is based on using only the smallest principle angle θ_1 , which gives the largest canonical correlation as:

$$(3.26) \quad d_{Max}(\mathcal{X}, \mathcal{Y}) = (1 - \cos^2 \theta_1)^{1/2} = \sin \theta_1.$$

1102 It is a Grassmann distance but not a metric since it can be 0 even though the two
1103 subspaces are not the same, so this can be a limitation for its use.

1104

Min Correlation: It is the opposite of *Max Correlation*, where it is based on only the largest principle angle θ_k , which gives the lowest canonical correlation.

$$(3.27) \quad d_{Min}(\mathcal{X}, \mathcal{Y}) = (1 - \cos^2 \theta_k)^{1/2} = \sin \theta_k.$$

It can also be rewritten as:

$$(3.28) \quad d_{Min}(\mathcal{X}, \mathcal{Y}) = \|X^T X - Y^T Y\|_2,$$

1105 where $\|\cdot\|_2$ is the matrix l_2 norm given by:

$$\|A\|_2 = \max_{x \neq 0} \frac{\|Ax\|_2}{\|x\|_2}, \quad A \in \mathbb{R}^{m \times n}.$$

1106 This distance is a Grassmann distance and satisfies the metric conditions.

1107

Procrustes distance: It is defined as the minimum distance between all possible subspaces spanned by two bases as:

$$(3.29) \quad d_{Proc}(\mathcal{X}, \mathcal{Y}) = 2 \left(\sum_{i=1}^k \sin(\theta_i/2) \right)^{1/2}.$$

It can also defined as:

$$(3.30) \quad d_{Proc}(\mathcal{X}, \mathcal{Y}) = \min_{R_1, R_2 \in \mathbb{O}(0)} \|XR_1 - YR_2\|_F.$$

1108 By definition, the Procrustes distance is invariant under different representations
1109 and furthermore is a valid metric.

1110

1111 The selection of the best distance for an application depends mainly on the data
1112 nature. For example, *Max Correlation* can be a good choice when the subspaces are
1113 scattered, and the data is noisy, and then we can depend on the largest canonical
1114 correlation only. The *Min Correlation* gives an opposite performance, since it uses the
1115 smallest canonical correlation. Thus, it can be a good choice when the subspaces are
1116 very close to each other and there is a slight difference among them. *Binet-Cauchy*
1117 *distance* performance is close to *Min Correlation* since it seeks for the smallest possible
1118 distance even though it uses all principle angles. Distances like Geodesic, Projection and
1119 Procrustes, give intermediate performance between the Max and the Min correlation
1120 distances. An experimental analysis for all of these metrics on 4D face recognition
1121 problems will be presented for 4D face recognition problem in the next Chapter 4.

1122 These measures capture different aspects of the distance on the manifold and can
1123 help to explore the data distribution in the subspace represented by the singular vectors
1124 for recognition and classification tasks.

1125 3.4 Statistical learning on Grassmann manifolds

1126 The subspace representation of 3D dynamic sequences as elements on Grassmann
1127 manifold and how to measure similarity using different distances and metrics have been

1128 introduced in the previous section. Now, the most important concept is how statistical
 1129 learning approaches can be adapted to work properly on such non-linear structure in
 1130 order to combine advantages of subspace modeling with the statistical learning tools.
 1131 There are two main directions for statistical learning on Grassmann manifold in the
 1132 literature:

1133 **Intrinsic Method** – This method relies on the basic idea of mapping the points of
 1134 the Grassmann manifold into a fixed tangent space using the logarithm map function
 1135 (i.e., a vector space) [27, 141]. The main constraint of this method is the computation
 1136 of logarithm map function, which does not have an explicit formula in the case of
 1137 Grassmann manifolds. This makes its estimation numerically not too accurate, especially
 1138 for the points far from the tangent space position and also it is time consuming. We will
 1139 discuss basic intrinsic methods like Karcher mean and k-means learning on Grassmann
 1140 later on.

1141 **Extrinsic Method** – To avoid intrinsic method limitations, this method consists to
 1142 embed the Grassmann manifold into a larger Euclidean space by predefined projection
 1143 mapping function, like in [124] and [136]. Here the computation is relatively simple by
 1144 comparison to intrinsic but the non-uniqueness embedding solution can lead to non-
 1145 uniqueness of statistics. The adaptation of the well-known dictionary learning and sparse
 1146 coding on Euclidean to work properly on non-flat Grassmann manifold will be presented.

1147 The implementations of these two types of learning on Grassmann with experimental
 1148 analysis on face recognition from 4D data are presented in the next Chapter.

1149 3.4.1 Sample (Karcher) mean computation

1150 As mentioned above, an important tool in shape (and its temporal evolution) analysis
 1151 is given by the computation of statistical summaries. For a set of given subspaces
 1152 $\mathbb{P} = \{\mathcal{P}_i\}_{i=1}^m$, where $\mathcal{P}_i \in \mathcal{G}_k(\mathbb{R}^n)$ (i.e., points on the underlying manifold), a sample mean
 1153 μ is a point on the Grassmannian, which minimizes the mean squared error [73] with
 1154 respect to the canonical metric d_{Geo} previously defined in Eq. 3.20.

1155 This algorithm starts by initializing the mean to the first subspace in the set initially,
 1156 then it uses the *Log Map* algorithm to project all \mathbb{P} elements on the tangent space of the
 1157 current mean point as depicted in Fig. 3.4. Then, computing the average vector from
 1158 all tangent vectors of the data points. The current mean moved in the direction of the
 1159 average vector by a certain step to have the new mean after projecting it back on the
 1160 manifold by using *Exp Map* algorithm. This loop is repeated till the convergence of the

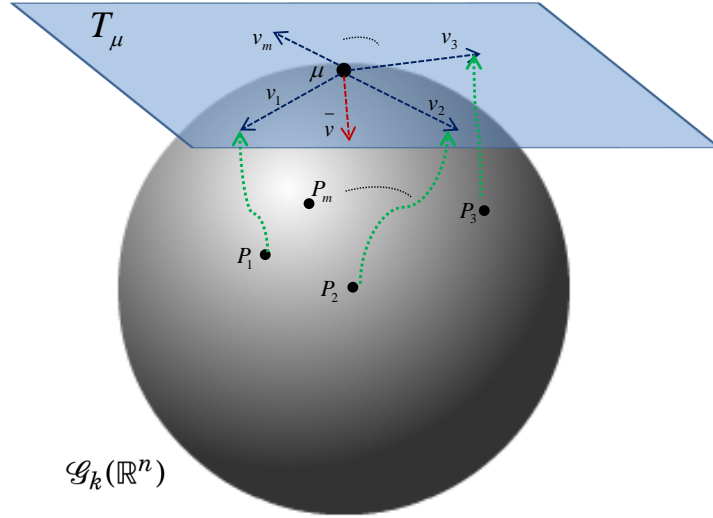


Figure 3.4: Estimation of a Karcher mean of a set of Grassmann elements.

1161 average vector norm to a predefined value. The steps to compute μ are summarized in
 1162 Algorithm 1.

Algorithm 1 – Mean Sample Estimation over $\mathcal{G}_k(\mathbb{R}^n)$

Require: $\mathbb{P} = \{\mathcal{P}_i\}_{i=1}^m$, where $\mathcal{P}_i \in \mathcal{G}_k(\mathbb{R}^n)$, $\epsilon > 0$ typically $\epsilon = 0.5$; τ : Threshold value

Initialize $\mu_0 \leftarrow \mathcal{P}_0$, $i \leftarrow 0$

repeat

 Compute $v_i \leftarrow \exp_{\mu_i}^{-1}(\mathcal{P}_j)$ for $j = 0, \dots, m$

 Compute the average tangent vector $\bar{v} \leftarrow \frac{1}{m} \sum v_i$

 Move μ_i according to $\mu_{i+1} \leftarrow \exp_{\mu_i}(\epsilon \bar{v})$

$i \leftarrow i + 1$

until ($\|\bar{v}\| \leq \tau$)

Ensure: μ the estimated mean of \mathbb{P} set

1163 **3.4.2 Grassmann k-means algorithm**

1164 Karcher mean is an efficient statistical tool on Grassmann manifold, where more im-
 1165 portant learning algorithm can be based on it. The K-means unsupervised learning
 1166 algorithm defined on Euclidean vector space can be extended to address the non-linear

1167 structure of Grassmann manifold depending on Karcher mean. Let us have a set of m sub-
 1168 spaces $\mathbb{P} = \{\mathcal{P}_i\}_{i=1}^m$ on Grassmann manifold. It is required to group these subspaces in N
 1169 classes according to their similarity measure by finding the mean of them $(\mu_1, \mu_2, \dots, \mu_N)$.
 1170 The same expectation Minimization EM-algorithm used in Euclidean k-means is used
 1171 here on minimizing the geodesic distances squares. First, an assignment of classes
 1172 means is done randomly from the subspaces set. Every subspace will be assigned to the
 1173 nearest class center in Expectation step, and the Karcher mean is computed for every
 1174 class members in Minimization step. These two steps are repeated a certain number of
 1175 times, which should be predefined according to the nature of the data. These steps are
 1176 summarized in Algorithm 2.

Algorithm 2 – K-means clustering on $\mathcal{G}_k(\mathbb{R}^n)$

Require: $\mathbb{P} = \{\mathcal{P}_i\}_{i=1}^m$, where $\mathcal{P}_i \in \mathcal{G}_k(\mathbb{R}^n)$, N : Number of classes, M : Max number of iterations

Initialize the classes center randomly $(\mu_1^0, \mu_2^0, \dots, \mu_N^0)$, $i \leftarrow 0$

repeat

 Compute the distance between \mathbb{P} members and cluster centers

 Assign every \mathcal{P}_i the closest cluster

 Re-computer clusters centers $(\mu_1^i, \mu_2^i, \dots, \mu_N^i)$ using Algorithm 1

$i \leftarrow i + 1$

until ($j = M$)

Ensure: The N cluster centers: $(\mu_1^M, \mu_2^M, \dots, \mu_N^M)$

1177 3.4.3 Sparse coding and dictionary learning

1178 Recently, the sparse coding and dictionary learning showed a great success in several
 1179 related topics like signal processing [142], image classification [51, 160] and face recog-
 1180 nition [140, 145], where a given signal or image can be approximated effectively as a
 1181 combination of few members (atoms) of a learned dictionary. The success of sparse coding
 1182 in several computer vision problems motivated to extend this learning approach from
 1183 vector space to nonlinear manifolds, like Grassmann [50, 132], in order to represent
 1184 a subspace as the combination of few subspaces of a dictionary. However, in so doing,
 1185 the main issue is the non-linearity of the Grassmann manifold, which implies using
 1186 tools from differential geometry. Since this often requires intensive computation, these
 1187 solutions are less attractive for 2D and 3D video modeling and analysis.

The problem of *sparse coding* has been solved in \mathbb{R}^n Euclidean space by minimizing the following quantity, which includes a coding cost function with a penalty term related to the sparsity of the result:

$$(3.31) \quad l(x, \mathcal{D}) = \min_y \|x - \mathcal{D}y\|_2^2 + \lambda \|y\|_1$$

where $x \in \mathbb{R}^n$ is the sample signal to be coded, \mathcal{D} is a dictionary (a $n \times N$ matrix being N the number of training samples) with atoms $D_i \in \mathbb{R}^n$ in its columns, and λ the sparse regularization parameter. The vector $y \in \mathbb{R}^N$ is the new latent sparse representation of the original data, which contains many zeros. The problem of *dictionary learning* consists of minimizing the total coding cost for all the samples $\{x^t \in \mathbb{R}^n\}_{1 \leq t \leq N}$ of the training set, over all choices of codes and dictionaries as follows:

$$(3.32) \quad h(\mathcal{D}) = \min_{\{x^t, \mathcal{D}\}} \frac{1}{N} \sum_{t=1}^N l(x^t, \mathcal{D}).$$

1188 In order to combine advantages of subspace modeling with the powerful sparse coding
 1189 representation, it is essential to handle the non-linearity of the Grassmann manifold. An
 1190 *extrinsic method* consists to embed the Grassmann manifolds into a smooth sub-manifold
 1191 of the space of symmetric matrices [146], as will be adopted in this work. This embedding
 1192 is performed by a projection mapping function already used in [124] and [136].

1193 Formally, let's have a set of points, for example subspaces that represent 3D dynamic
 1194 facial sequences in this work, $\mathbb{X} = \{X_i\}_{i=1}^m$, where $Span\{X_i\} \in \mathcal{G}_k(\mathbb{R}^n)$. We need to be
 1195 able of representing each point (subspace) as a linear combination of a few atoms of a
 1196 dictionary of subspaces $\mathbb{D} = \{D_1, D_2, \dots, D_j\}$ using the sparse coding technique.

1197 For any $\mathcal{X} = Span(X) \in \mathcal{G}_k(\mathbb{R}^n)$ the mapping $\mathcal{D} : \mathcal{G}_k(\mathbb{R}^n) \rightarrow Sym(\mathbf{n})$, such that $\mathcal{D}(\mathcal{X}) =$
 1198 $XX^T = \hat{X}$ is computed.

The mapping function \mathcal{D} is isometric, as it preserves the curve length between the Grassmann manifold and the manifold of Symmetric matrices $Sym(\mathbf{n})$ [62]. A natural choice of metric on the manifold of symmetric matrices $Sym(\mathbf{n})$ is the Frobenius inner product. For any $Span(X), Span(Y) \in \mathcal{G}_k(\mathbb{R}^n)$, $Frobenius(X, Y) = Tr(\hat{X}, \hat{Y}) = \|X^T Y\|_F^2$. With this embedding, Eq. (3.31) can be rewritten by considering the embedding \hat{X} of a given query subspace \mathcal{X} :

$$(3.33) \quad l(\mathcal{X}, \mathcal{D}) = \min_y \|\hat{X} - \hat{\mathcal{D}}y\|_F^2 + \lambda \|y\|_1,$$

1199 where $\hat{\mathcal{D}}$ denotes the dictionary with atoms elements of $Sym(\mathbf{n})$ and y the sparse repre-
 1200 sentation. This convex optimization problem is solvable as a vectorized sparse coding
 1201 problem, as depicted in Algorithm 3.

Algorithm 3 – Sparse Coding on $\mathcal{G}_k(\mathbb{R}^n)$

Require: A given dictionary $\mathbb{D} = \{\mathcal{D}_i\}_{i=1}^N \in \mathcal{G}_k(\mathbb{R}^n)$ where $\mathcal{D}_i = \text{Span}(D_i)$ of size N . Query subspace

$$\mathcal{X} \in \mathcal{G}_k(\mathbb{R}^n) = \text{Span}(X)$$

for $i, j \leftarrow 1$ to N **do**

$$\mathbb{K}(\mathbb{D})_{i,j} \leftarrow \|D_i^T D_j\|_F^2$$

end for

$$\mathbb{K}(\mathbb{D})_{N \times N} = U \Sigma U^T$$

$$A = \Sigma^{1/2} U^T$$

for $i \leftarrow 1$ to N **do**

$$\mathcal{K}(X, \mathbb{D})_i \leftarrow \|X^T D_i\|_F^2$$

end for

$$x^* \leftarrow \Sigma^{-1/2} U^T \mathcal{K}(X, \mathbb{D})$$

Ensure: $y^* \leftarrow \arg \min_y \|x^* - Ay\|^2 + \lambda \|y\|_1$

In Algorithm 3, the training set of (labeled) subspaces is considered as the dictionary \mathcal{D} of size N (i.e., the training set size); (i) A similarity matrix between dictionary elements $\mathbb{K}(\mathcal{D})$ is computed based on the Frobenius inner product; (ii) Singular Value Decomposition (SVD) is applied to \mathbb{K} (i.e., $\mathbb{K} = U \Sigma V^T$) to compute the A matrix, which is the weighted singular vectors of \mathbb{K} ; (iii) The similarity matrix $\mathcal{K}(X, \mathcal{D})$ between testing and training samples is computed on the induced space. The decomposition of Eq. (3.33) shows that the sparse coding problem can be formulated as:

$$(3.34) \quad l(\mathcal{X}, \mathcal{D}) = \min_y \|x^* - Ay\|^2 + \lambda \|y\|_1,$$

1202 where $x^* = \Sigma^{-1/2} U^T \mathcal{K}(X, \mathcal{D})$.

1203 We can see that this algorithm ends up by representing every subspace by a linear
 1204 feature vector called a sparse code. This sparse code allows us to reconstruct the related
 1205 subspace from a dictionary of subspaces. Thus, we are in a Euclidean space and sev-
 1206 eral learning and classification algorithms will be available to classify this new linear
 1207 representation of the subspace as will be discussed in the next Chapter 4.

1208 3.5 Trajectories on Riemannian manifolds

1209 In the previous section, we discussed the subspace representation of 3D dynamic facial
 1210 sequences and its ability to capture the global structure and the variation over time of the

1211 dynamic face. In some cases, the 3D dynamic video is divided into shorter subsequences
1212 and every one is modeled as a separate subspace to overcome some problems, like pose
1213 variation or high variability in facial surface. The statistical tools could be applied to this
1214 multiple-instances representation, like Karcher mean, k-means clustering and sparse
1215 coding are useful if the order of the subsequences is not important, like in face recognition
1216 problem. In other cases, the important information is not only in the subsequences, but
1217 also in the temporal evolution of the facial data over time from on subspace to another.
1218 This temporal information can be captured from the difference between successive sub-
1219 spaces that belong to the same video. For example, in the case of emotional state that
1220 is conveyed through a complete video. Here, keeping the order of subsequences and the
1221 ability to extract difference between ordered subspaces is very important to obtain the
1222 spatio-temporal description of this emotional state. Now, it is important to define: **How**
1223 **can we capture the spatio-temporal information conveyed through the com-**
1224 **plete 3D video that is represented as a set of subspaces?** The proposed solution
1225 in this work is by considering the set of subspaces as a parametrized trajectory on Rie-
1226 mannian manifold by time. Here, every subspace represents an instance (t). Considering
1227 such trajectory of subspaces gives us the ability to measure and capture the temporal
1228 evolution through time between neighboring subspaces of the trajectory or according to
1229 a reference subspace. The concept of time-parametrized curves (trajectories) analysis on
1230 Riemannian manifold introduced in [69] and applied to several computer vision problems,
1231 like action recognition [9] and 3D action recognition [16]. In the latter paper, Ben Amor et
1232 al. have addressed the problem of action/activity recognition from skeletal data (acquired
1233 using Kinect-like cameras). They have proposed a suite of geometric tools for processing
1234 static and dynamic shapes as elements and trajectories in the well-known Kendall shape
1235 space (which provides invariance to scale, translation and rotation), respectively. The
1236 main ingredient introduced in [16] is an elastic metric for aligning pairwise (or multiple)
1237 trajectories.

1238 3.5.1 Trajectories on Grassmann manifolds

1239 As far as Grassmann trajectories are concerned in the present study, let $t \rightarrow \mathcal{T}(t)$
1240 be a parameterized curve on $\mathcal{G}_k(\mathbb{R}^n)$, and $V(t)$ the velocity (tangent) vector following
1241 the geodesic path between $\mathcal{X}(t)$ and $\mathcal{X}(t + \delta)$. The tangent vector is an element of
1242 $T_{\mathcal{X}(t)}(\mathcal{G}_k(\mathbb{R}^n))$. Note that the parameter t denotes the time in our target application
1243 as follows. If $[f^0, \dots, f^s]$ denotes a 3D sequence acquired in the time interval $[0, s]$,
1244 consequently, the underlying trajectory represents the full (or partial) available time-

1245 space observations in the same time-interval. This provides a precise mathematical
 1246 representation of trajectories on the Grassmannian, and allows deriving interesting
 1247 quantities to analyze flows of 3D or depth sequences for human emotion detection as
 1248 it will be investigated in Chapter 5 for early detection of spontaneous emotional states.
 1249 If needed, one can define the space of trajectories easily by $\mathcal{G}_k(\mathbb{R}^n)^{[0,s]}$, and extend the
 1250 distance definition of the Grassmannian to this space by integrating d_{Geo} (Eq. (3.20))
 1251 over the parameter interval $[0, s]$. This is actually a proper distance between trajectories
 1252 defined on the Grassmann manifold.

1253 After solving the problem of representing, we need to define a mapping function ζ as
 1254 follows:

1255 **Definition 3.5.1.** For any $\mathcal{X}_1, \mathcal{X}_2 \in \mathcal{G}_k(\mathbb{R}^n)$, the mapping $\zeta : \mathcal{G}_k(\mathbb{R}^n) \times \mathcal{G}_k(\mathbb{R}^n) \rightarrow \mathbb{R}^m$ such
 1256 that $\zeta(\mathcal{X}_1, \mathcal{X}_2) = Z$ where $Z \in \mathbb{R}^m$ and $m \ll n$.

1257 Scanning the trajectory $\mathcal{T}(t)$ through time t using this $\zeta(t)$ function and concatenating
 1258 the feature over time results in the final spatio-temporal feature vector of the 3D dynamic
 1259 video in Euclidean space of $\mathbb{R}^{m \times s}$, where s is the size of $\mathcal{T}(t)$. Thus, we can implement
 1260 Euclidean classification methods, like the Structured Output Support Vector Machine
 1261 (SO-SVM) for the sequential analysis and classification of such features by the time
 1262 as will be addressed in Chapter 5. Figure 3.5 illustrates this mapping function of time
 1263 parametrized trajectories on Riemannian manifold into Euclidean space.

1264 In this work, two methods to define ζ will be presented: the first depending on the in-
 1265 stantaneous speed between trajectory elements, and the second depending on computing
 1266 the velocity vector between the trajectory elements to capture more information than
 1267 the speed.

1268 3.5.2 Instantaneous speed along trajectories

1269 One intuitive alternative to analyze trajectories on Stiefel or Grassmann manifolds is to
 1270 consider the evolution of their instantaneous speed. In particular, given an observed por-
 1271 tion of the trajectory in the time interval $[0, t]$, the instantaneous speed can be computed
 1272 as the distance between neighboring points $\mathcal{X}(t)$ and $\mathcal{X}(t + \delta)$ along the trajectory. In this
 1273 case, the function ζ substituted by Geodesic distance (d_{Geo}) on Grassmann manifold and
 1274 the Stiefel distance (the Frobenius norm) on Stiefel manifold with parameter δ as a con-
 1275 stant integer, $\delta = \{1, 2, 3 \dots\}$. These distances can be concatenated in a one-dimensional
 1276 vector characterizing the temporal evolution along the trajectories.

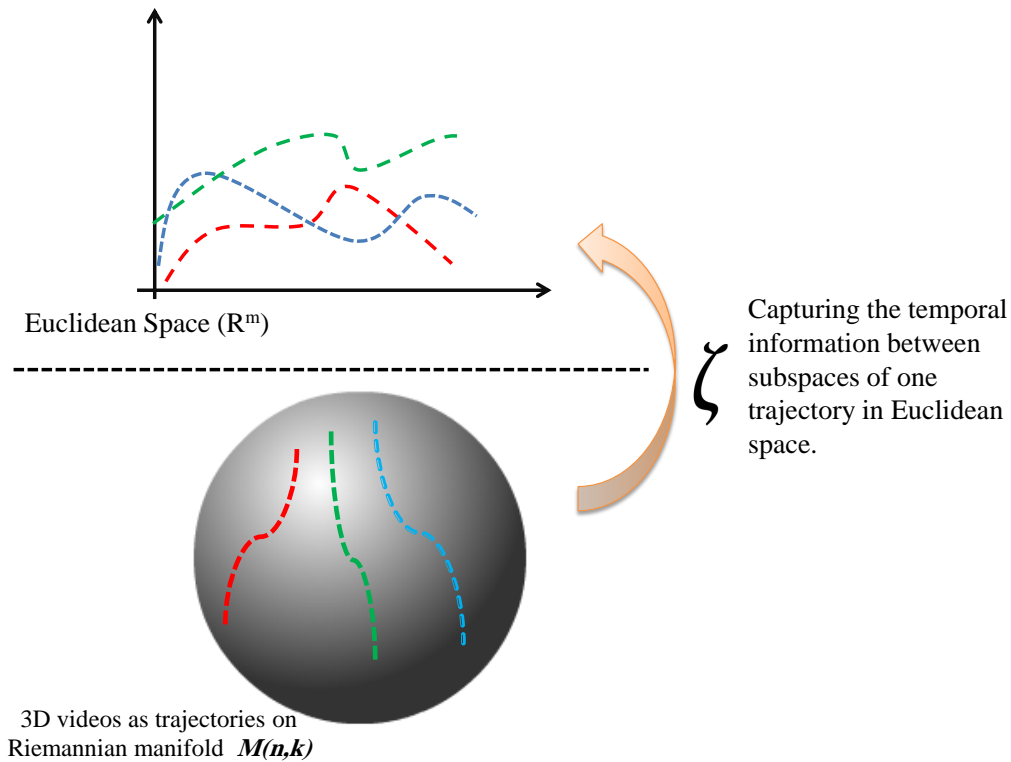


Figure 3.5: Illustration of ζ function and how to capture the spatio-temporal Euclidean feature vector from parametrized trajectory on Riemannian manifold.

1277 One can view this quantity (geodesic distance between subspaces of the same tra-
 1278 jectory) as the norm of the shooting (initial velocity) vector between subspaces. Thus,
 1279 the feature vector of instantaneous speed along the trajectories captures the rhythm
 1280 (temporal) and amplitude (spatial) of the facial deformations, which could be of great
 1281 interest for emotion detection. However, this quantity is limited to study the amplitude
 1282 of the deformation (as a single scalar) for each frame. A natural way to get more complete
 1283 idea about the (spatial) deformations is to use the velocity vector itself (instead of its
 1284 norm). Next section provides a detailed description of the velocity vector and its use in
 1285 physical pain detection will be presented in Chapter 5.

1286 3.5.3 Transported velocity vector fields of trajectories

1287 The quantities presented in the previous approach allow us to quantify the motion's
 1288 amplitude and the temporal rhythm along the trajectories defined on Riemannian
 1289 manifolds like Grassmann and Stiefel. To show how the full motion information (face
 1290 deformation/body and head gestures) one should look at the fields of velocity vectors

1291 instead of their norms, along the trajectories on Grassmann manifolds. However, these
 1292 velocity vectors belong to different tangent spaces ($V(t) \in T_{\mathcal{X}}(\mathcal{G}_k(\mathbb{R}^n))$). One possible
 1293 solution to this issue is to translate the velocity vector fields to the same and fixed
 1294 tangent space (e.g., the identity tangent space $\mathcal{S} = span\left(\begin{bmatrix} I_k \\ 0 \end{bmatrix}\right)$) which is given: $\mathcal{T}_i(t)$

Definition 3.5.2. Let us have a trajectory of subspaces $t \leftarrow \mathcal{T}(t)$ on Grassmann manifold $\mathcal{G}_k(\mathbb{R}^n)$, and let V be a tangent vector defined along the geodesic path $\mathcal{T}(\cdot)$. Then, V said to be *Parallel transported*: along $\mathcal{T}(\cdot)$ if:

$$(3.35) \quad \nabla_{\mathcal{T}(\cdot)} V = 0$$

1295 for all t , where $\mathcal{T}(\cdot)$ refers to the tangent vector to $\mathcal{T}(\cdot)$ at t [4].

1296 Overall, after computing the velocity vectors $\dot{\mathcal{X}}(t)$ between neighboring points on the
 1297 trajectory, $\mathcal{X}(t)$ and $\mathcal{X}(t + \delta)$, we use the parallel transport on Grassmann manifold to
 1298 translate it to the fixed tangent space. Repeating this operation for all velocity vectors
 1299 along the trajectory results in an equivalent representation in a vector space (the
 1300 tangent space attached to the identity element) to compute $V(t)_{\mathcal{X} \rightarrow \mathcal{S}}$. Hence, the obtained
 1301 transported velocity vector field reflects the way the motions are exhibited by the face or
 1302 the body.

1303 One can view the field of (transported) velocity vectors as a basic dynamic model to
 1304 characterize the motion along Grassmann trajectories. That is, each velocity vector is by
 1305 definition the first derivative of the geodesic path between subspaces, taken at the initial
 1306 point of the geodesic. It is important to note that one can recover the initial trajectory
 1307 knowing the velocity vector field and the initial point of the trajectory. Finally, a more
 1308 complex dynamic model could be derived by including, in addition, the velocity vector
 1309 fields the acceleration vector fields, and so on.

1310 3.6 Conclusion

1311 In this chapter, we have introduced a compact subspace representation of 3D videos and
 1312 the motivation behind adopting it in our work. The technique of computing subspace from
 1313 original data is discussed as well as the new nonlinear domain obtained from the linear
 1314 subspaces of our data, called Grassmann manifold. The mathematical background and
 1315 the geometrical properties of the underlying manifold such the the definition of metrics
 1316 metrics on it to compare subspaces, the local linearity of this manifold, which induces the

1317 intrinsic learning approaches using tangent spaces. Also, the extrinsic learning method
1318 by embedding the non-flat manifold into another smooth manifold with a linear structure
1319 are discussed. Performing advanced learning, like sparse coding and dictionary learning,
1320 which can present several benefits (efficiency, ...) in classification and recognition are
1321 presented.

1322 Also, how this Riemannian structure can support the sequential (partial) model-
1323 ing/analysis of 3D dynamic data as time-parametrized curves of subspaces, and how
1324 we are able to capture the temporal information resides through these trajectories on
1325 the manifold to get relevant spatio-temporal representations. In the next chapter, we
1326 will introduce our approach to study the contribution of facial dynamics to the face
1327 recognition problem. Application and experimental illustrations of the mathematical
1328 tools introduced in this chapter will be used in the next one.

FACE RECOGNITION FROM 4D DATA

4.1 Introduction

1329 As a first targeted application of the Grassmann representations, in particular the
1330 dictionary representation (presented in Section 3.4.3 of the previous Chapter), the
1331 present chapter introduces our 4D face recognition approach. The main task addressed
1332 here is to study the contribution of facial 3D shape’s evolution over time in identity
1333 recognition. This topic is new and a few studies exist [128] until now, where the majority
1334 of current approaches exploit the 3D static shape of the face with a lack of investigation
1335 of its behavioral biometric. Moving from shape analysis of 3D static faces to dynamic
1336 faces (4D faces) gives rise to several new challenges related to the nature of the data
1337 and the processing algorithms. **1) Which static and dynamic shape representation
1338 is the most suitable for 4D face analysis? 2) How can the temporal dimension
1339 contribute in face recognition? 3) How efficient is it to compute statistical
1340 summaries on dynamic 3D faces? 4) From a perspective of face classification,
1341 which relevant features and classification algorithms can be used? 5) What
1342 are the challenges that unconstrained face recognition meets when working
1343 on 3D dynamic data?**

1344 In this chapter, we aim to answer the above questions, by proposing a comprehensive
1345 framework for modeling and analyzing 3D facial sequences (4D faces), with an exper-
1346 imental illustration in face recognition from 4D sequences. The rest of the chapter is
1347 organized as follows – after an overview of the proposed solution presented in Sect. 4.2,

1348 in Sect. 4.3 the methodology of modeling 4D faces on Grassmann manifold is introduced;
1349 Our 3D dynamic face recognition framework is presented in Sect. 4.4; Experimental
1350 results and their discussions are given in Sect. 4.5. A new dataset for 4D face recognition
1351 in adverse conditions with preliminary evaluation experiment is presented in Sect. 4.6.
1352 Our conclusions and main findings out of the proposed approach are drawn in Sect. 4.7.

1353 4.2 Overview of the proposed solution

1354 Most of the recent face recognition approaches use sets of 2D still images (with different
1355 illumination or pose) or 2D videos as a data source. Besides, the subspace representa-
1356 tion showed promising results with possible methodological and application extensions
1357 related to the geometry of the underlying manifolds (i.e., Grassmann manifolds), such
1358 as domain adaptation [53], multiple motion segmentation [26], video clustering [121],
1359 filtering [106] and others [88]. Also, advanced classification techniques, which lie on
1360 the non-linear nature of the data have been proposed, such as the extrinsic solutions
1361 to the problem of sparse coding and dictionary learning on Grassmann manifold [59].
1362 On the other side, the use of the 3D facial shape for recognition purposes has been well
1363 explored [18, 40], in particular with the availability of the FRGC dataset and related
1364 experiments [101]. In contrast, little attention has been paid to the role of the shape
1365 dynamics (behavior) in identity recognition. In particular, Sun et al. [128] developed a
1366 vertex-flow tracking method to enable face recognition from temporal sequences of 3D
1367 face scans. In this method, they have showed the usefulness of 4D faces in the recog-
1368 nition process, instead of 2D videos and static 3D shapes. However, this approach is
1369 computationally expensive.

1370 Following this new and promising line of research, we conducted a comprehensive
1371 study to investigate the role of 3D face dynamics in face recognition. To this end, as
1372 illustrated by the pipeline in Fig. 4.1, after a preprocessing step, we compute 3D surface
1373 curvature from each 3D static mesh of a sequence, and project it to a 2D map (called
1374 curvature-map). A sequence of curvature-maps is then shaped in a matrix form by
1375 reshaping the 2D maps to column vectors. A (compact) k -Singular Value Decomposition
1376 (k -SVD) is used to produce the subspace basis from the first k singular vectors, that is
1377 regarded as a point on a Grassmann manifold. These vectors build our spatio-temporal
1378 signature, which will be used in the recognition process in combination with both intrinsic
1379 and extrinsic classification methods on the underlying manifold. In particular, extrinsic
1380 methods based on sparse coding and dictionary learning achieved the best performances.

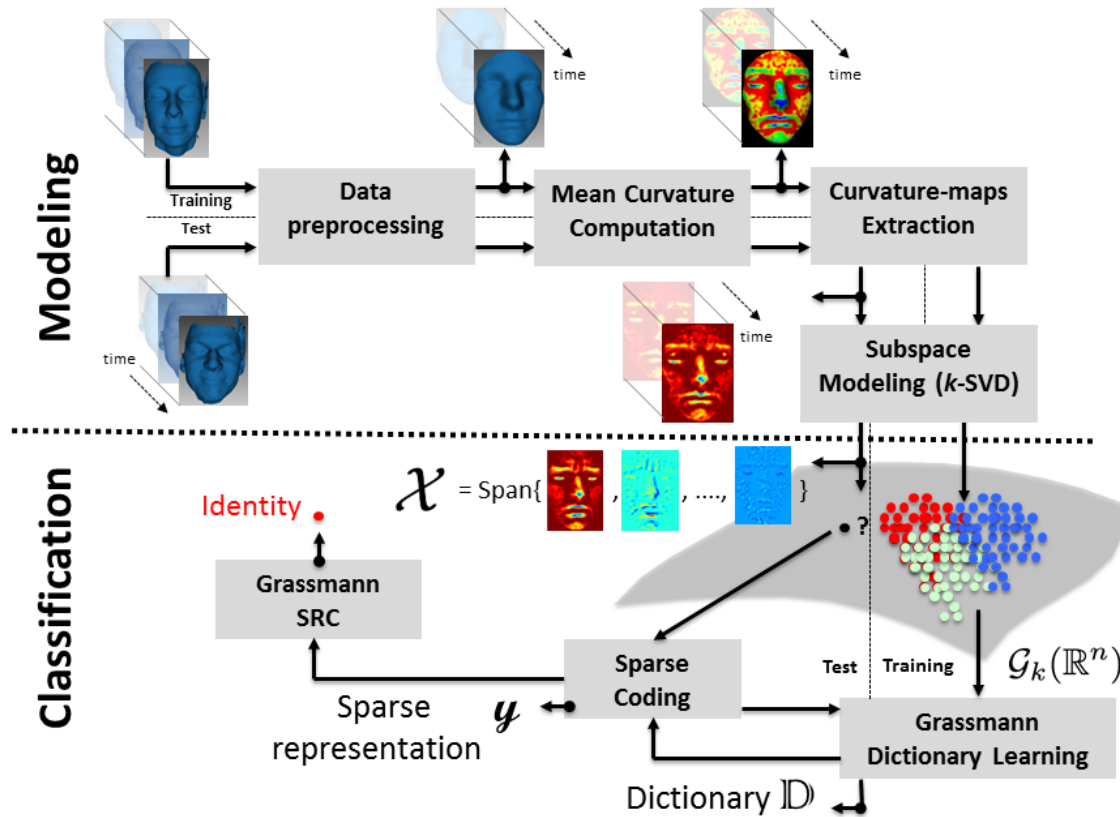


Figure 4.1: Overview of the proposed approach: top – modeling the shape and its dynamics using a subspace representation; bottom – classification of space representations using the SRC algorithm.

1381 Figure 4.1 shows the above-mentioned method based on sparse coding and dictionary
 1382 learning. The main contributions in this part of the thesis are:

- 1383 - A fully automatic and computationally cheap face recognition approach using
 1384 4D data. To the best of our knowledge, this is the first study in the literature,
 1385 which explores the subspace modeling methodology with advanced geometric and
 1386 learning tools for 4D facial domain. Thus, a comprehensive framework is proposed
 1387 and validated, which spans from the description of the 3D static shape and the
 1388 modeling of its dynamics to an adequate classification schema;
- 1389 - An in-depth investigation of the 3D shape dynamics contribution to face recognition
 1390 is conducted, either in the case the facial expression is controlled or not.
- 1391 - Instead of using the conventional autoregressive and moving average (ARMA)

- 1392 model for spatio-temporal analysis, which separates the appearance of visual data
1393 and their temporal evolution, our goal is to keep the shape and its motion in the
1394 same representation for identity recognition. The latter data is then represented
1395 by an optimized subspace, using the k -SVD orthogonalization procedure. The
1396 (optimized) subspace representation is suitable to process 3D data, which usually
1397 present missing parts (holes) and noise due to the acquisition process;
- 1398 - An extensive experimental analysis, involving the BU-4DFE dataset and three
1399 classification schemes based on intrinsic and extrinsic methods: (1) A nearest-
1400 neighbor (NN) algorithm performed on the Grassmann manifold with respect to
1401 the (subjects) classes mean; (2) a variant of Grassmann Discriminant Analysis
1402 (GDA), called Graph-embedding GDA [60]; (3) A Sparse Representation-based
1403 Classification (SRC) derived from the Grassmann Dictionary Learning (GDL)
1404 approach [140][59].
 - 1405 - A new 3D/4D dynamic database of 58 subjects is collected in our laboratory to
1406 explore 4D face recognition problem in diverse conditions such as pose variation,
1407 expressions, talking, walking, internal and external occlusions and several persons
1408 in the scene. A preliminary evaluation on this new database has been conducted.

1409 **4.3 Modeling 4D-faces on Grassmann manifold**

1410 The idea of modeling multiple instances of visual data, like set of images or video se-
1411 quences, as linear subspaces for classification and recognition tasks has revealed its
1412 efficiency in many computer vision problems [56, 132, 133]. The advantages of using this
1413 compact low-dimensional for 3d dynamic data representation can be summarized in its
1414 robustness against noise or missing parts in the original data; The ease of comparing
1415 two subspaces instead of two sets of 3D scans in Euclidean space; and the availability
1416 of computational tools from differential geometry makes working on non-linear data
1417 structure (e.g., the space of k -dimensional subspaces) possible and allows managing
1418 the non-Euclidean nature of these subspaces. Accordingly, in this work, we adopt the
1419 subspace representation solution for analyzing 4D facial sequences. To our knowledge,
1420 this is one of the earliest investigations on modeling the temporal evolution of 3D facial
1421 shapes with application to face recognition. Studying the effects of these two aspects
1422 together is still an open problem in computer vision domain.

1423

1424 In the proposed solution, we consider 3D scans of the face acquired continuously
 1425 via a dynamic 3D scanner, thus producing a temporal 3D sequence with the dynamic
 1426 evolution of the 3D face. Using these data, the proposed approach is designed to exploit
 1427 the spatio-temporal information. To achieve this goal, a subspace modeling technique is
 1428 applied as follows: (i) The 3D scans are preprocessed by cropping the facial region from
 1429 the rest of the scan, then pose normalization, denoising via smoothing, and holes filling
 1430 are performed; (ii) The mean curvature on 3D surfaces is computed, so that a flow of
 1431 curvature-maps is produced by projection; (iii) The k -SVD orthogonalization procedure
 1432 is applied to subsequences of the curvature-maps to obtain an orthonormal basis span-
 1433 ning an optimized subspace. This subspace represents an element of a Grassmannian
 1434 manifold.

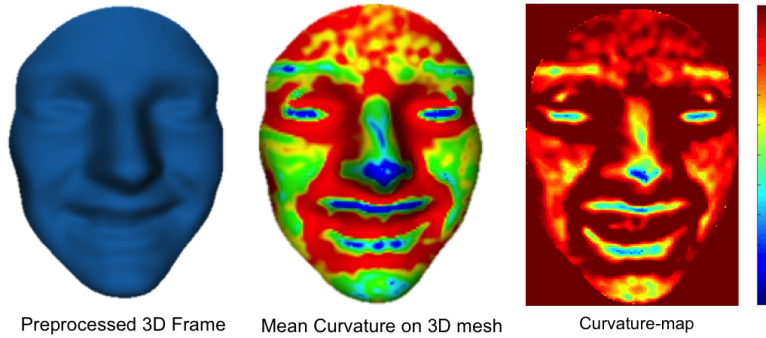


Figure 4.2: 3D static facial shape representation using the mean curvature. From left to right, the pre-processed 3D face, the mean curvature computed on the 3D mesh, and the normalized curvature-map are reported.

1435 The first step of this framework is illustrated in Fig. 4.2. On the left, the preprocessed
 1436 face scan is reported; The mean curvature computed on the mesh is reported in the
 1437 middle. The curvature map projected on a 2D image of size $\hat{n} \times \hat{m}$ is shown on the right.
 1438 This latter map extracted for each frame of a sequence constitutes the data source for our
 1439 spatio-temporal analysis. More formally, let S_m be a 3D dynamic face sequence with m
 1440 frames. A subsequence of $\omega < m$ frames is indicated with $S_\omega = \{f_1, f_2, \dots, f_\omega\}$, where each
 1441 f_i is a curvature-map of linearized size $n = \hat{n} \times \hat{m}$, that is $S_\omega \in \mathbb{R}^{n \times \omega}$, and ω is regarded
 1442 as the *window size*. Applying the k -SVD orthogonalization procedure where $S_\omega = U\Sigma V^T$,
 1443 and the k first columns of U matrix provide the dominant k -left singular vectors of S_ω .
 1444 The subspace spanned by these vectors is an element of the Grassmann manifold $\mathcal{G}_k(\mathbb{R}^n)$.

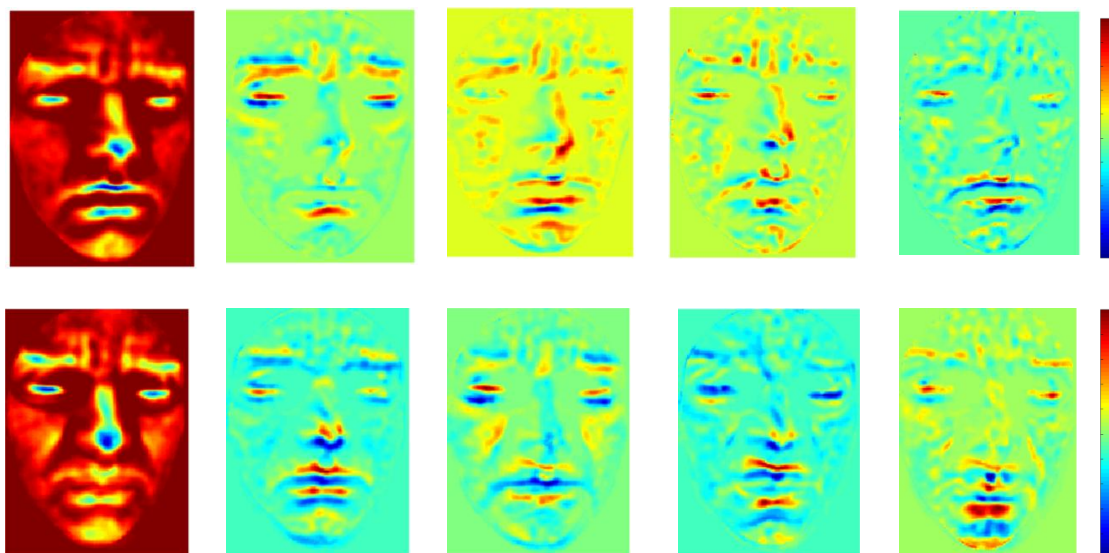


Figure 4.3: Visual illustration of two subspaces (i.e., points on the Grassmann manifold) using their singular vectors derived from SVD *orthogonalization* on sequences of $\omega = 50$ frames (*angry*, top row – *disgust*, bottom row). From left to right, the 5-dominant left singular-vectors (subspace of order 5) of the original data are shown. The first column represents the common shape description over the sequence. While the remaining columns capture the dominant facial motions of the face.

Figure 4.3 shows, as color maps, the matrices representing the subspaces computed from two different 3D facial sequences. It can be appreciated that a subspace (k first dominant left singular vectors of the original matrix of data) can be viewed as the mean shape computed over the subsequence (leftmost images), followed by the dominant deformations (remaining images on the right). These deformation images are different from each other, and change in respect to the expression exhibited by the face (*angry* in the first row, and *surprise* in the second). The histogram equalization is used here (except for the images in the left column) to highlight the location of the deformation areas, using cold to warm colors. Colors in between reflect the most stable areas of the curvature-maps over the 3D video. The singular value decomposition technique provides us a measure to evaluate the importance of the information that every singular vector carries in relative to the original data. This evaluation can be obtained from the singular values which are the diagonal elements of the matrix Σ . Equation 4.1 gives the percentage of the information resides in every first k vectors, thus we can decide the threshold to stop

considering the left ones, which is 90% in our case:

$$(4.1) \quad Y_k = \frac{\sum_{i=1}^k \lambda_i}{\sum_{i=1}^{\omega} \lambda_i},$$

1445 where λ_i is the singular value corresponding to singular vector U_i .

1446 In Fig. 4.4, we report the percentage of the information kept (after the matrix fac-
1447 torization) as a function of the number of singular vectors for different window size
1448 $\omega \in \{6, 10, 15, 20, 25\}$ given in Eq. 4.1.

1449 From Fig. 4.4, the amount of information increases by considering more singular
1450 vectors, till arriving to 100% by using all of them. Interestingly, in all the cases, about
1451 90% of the information of a sequence is captured by considering less than half of the
1452 singular-vectors. This observation suggests us the identity information mainly resides in
1453 the few first dominant singular vectors. While the remaining components contain the
1454 noise and redundant information. From this illustration and discussion, the concept of
1455 compact and low dimensional representation appears clearly.

1456 4.4 Identity recognition algorithms

1457 To perform face recognition from the 3D facial shapes and their temporal evolution, the
1458 flow of curvature-maps is first divided into clips (subsequences) of size ω . Then, each clip
1459 is modeled as an element of Grassmann manifold via k -SVD orthogonalization. More
1460 formally, given a sequence of curvature-maps $\{m_0, \dots, m_t\}$, a predefined size of a sliding
1461 window ω , and a fixed order of subspaces k , the idea is to consider the maps under
1462 the temporal interval $[t - \omega + 1, t]$ and to compute the corresponding subspace \mathcal{X}_t . This
1463 results in a collection of subspaces, elements of Grassmann manifold, which represent
1464 the 3D video sequence (after curvature computation).

1465 The main goal of such representation is to capture the 3D shape of the face as well as
1466 its dynamics (spatio-temporal description) to perform face recognition. In the following,
1467 we present two classification methodologies are used in this work: The Grassmann
1468 Nearest Neighbor classifier (GNNC) based on one of the distances defined on Grassmann
1469 manifold have been defined in Sect. 3.3.5. This classification method involves the Karcher
1470 mean subspace estimation (Algorithm 1) to compute a representative target subspace for
1471 each subject class; The second method uses Grassmann Sparse Representation (GSR)
1472 classifier adapted to classify the testing subspaces depending on their sparse codes
1473 implemented as detailed in Sect. 3.4, Algorithm 3.

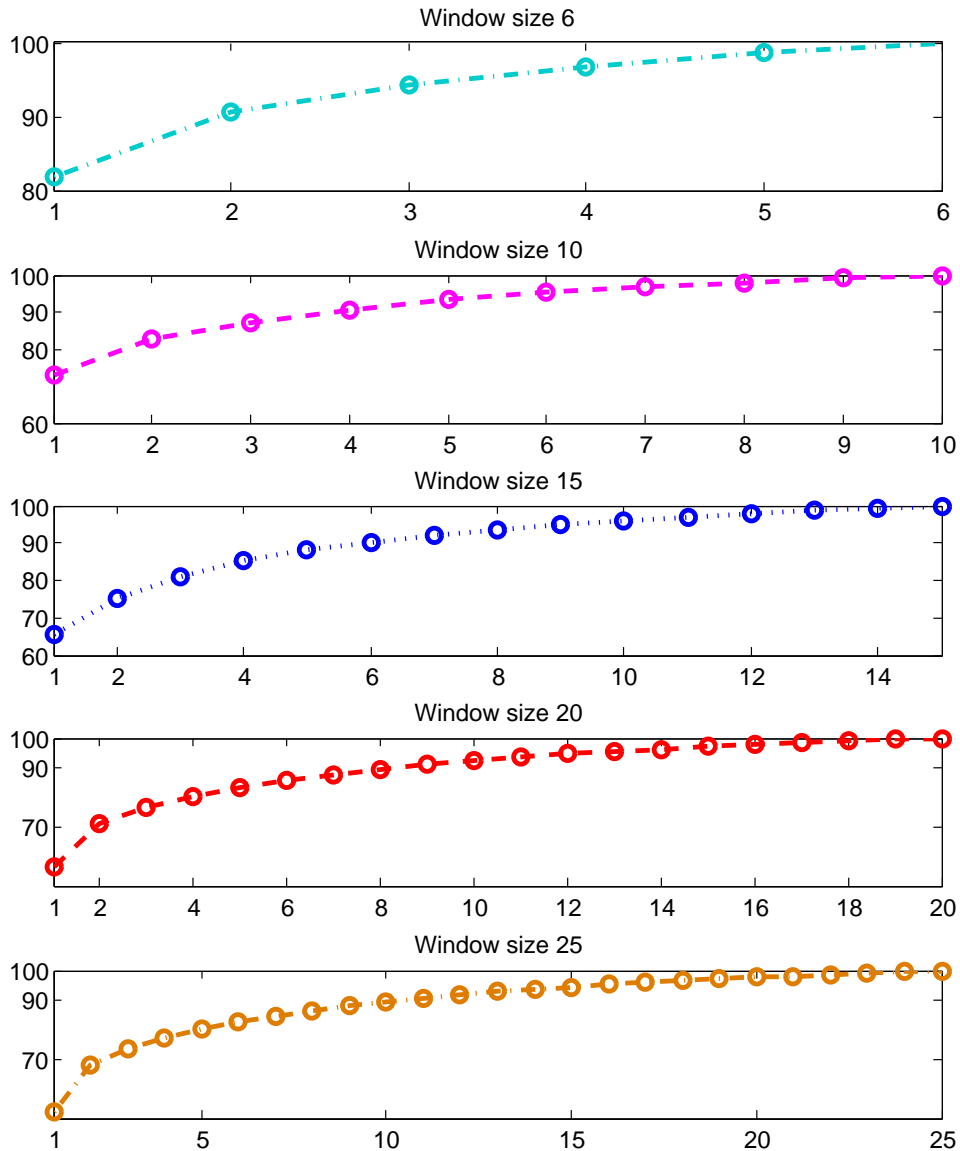


Figure 4.4: Information Y_k captured by the first k singular vectors returned by SVD as a function of λ . Results for different window size are reported.

1474 **4.4.1 Grassmann Nearest-Neighbor Classifier (GNNC)**

1475 In this approach, for each subject a mean (representative) subspace is computed out
 1476 of the subspaces that belong to the same subject in the training set (i.e., more than
 1477 one subsequence is used in the training for each individual) by applying Karcher mean
 1478 Algorithm 1. These means constitute the gallery subspaces used for recognition. Accord-
 1479 ing to this, given a probe subspace $\mathcal{X} = Span(X)$, it is compared against the gallery

1480 mean subspaces using one of the distances defined on the Grassmann manifold (see
 1481 Sect. 3.3.5). Finally, the probe subspace is assigned to one class using the Grassmann
 1482 Nearest-Neighbor classifier. Figure 4.5 illustrates the idea of computing the principal
 1483 angles between subspaces, which are served to compute the distances.

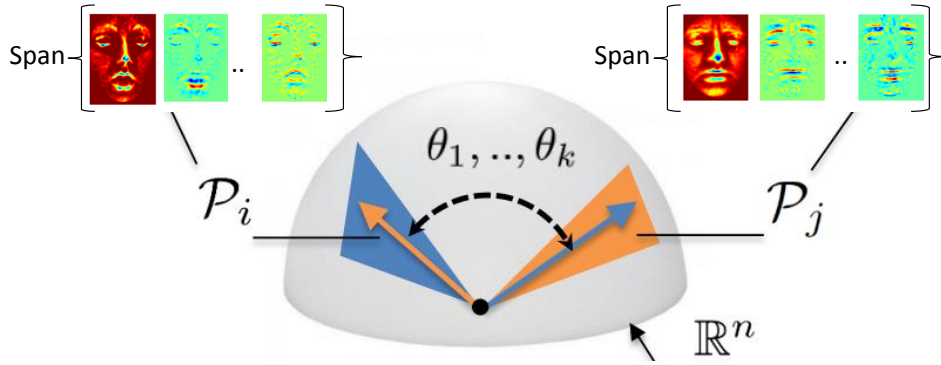


Figure 4.5: Comparing the similarity of two 3D dynamic subsequences after presenting them as two subspaces P_i, P_j of dimension k on \mathbb{R}^n .

1484 Learning one mean subspace for the subject (class) as a representative makes the
 1485 recognition much faster than using an exhaustive search that compares the probe against
 1486 all the subspaces in the training. Algorithm 4 summarizes the classification steps, where
 1487 the mean subspace estimation is performed off-line. While the comparison of the probe
 1488 subspace to the gallery subspaces is performed online.

Algorithm 4 – Grassmann Nearest-Neighbor Classification

Require: Set of training subspaces $\mathbb{X} = \{\mathcal{X}_i\}_{i=1}^m \in \mathcal{G}_k(\mathbb{R}^n)$ where $\mathcal{X}_i = Span(X_i)$, belong to C classes, the query sample $\mathcal{Y} = Span(Y) \in \mathcal{G}_k(\mathbb{R}^n)$

for $i \leftarrow 1$ to C **do**

 Compute the Karcher mean μ_i using Algorithm 1

end for

for $i \leftarrow 1$ to C **do**

$d_i(\mathcal{Y}) = \text{dist}(\mathcal{Y}, \mu_i)$ // one of the distances of Sect. 3.3.5

end for

Ensure: $\text{Identity}(\mathcal{Y}) \leftarrow \arg \min_i (d_i(\mathcal{Y}))$

1489 In this algorithm, $\text{dist}(\cdot, \cdot)$ denotes one of the Grassmann distances defined in Sect. 3.3.5.
 1490 A comparison study of these distances performance is presented in the experimental
 1491 evaluation in Sect. 4.5

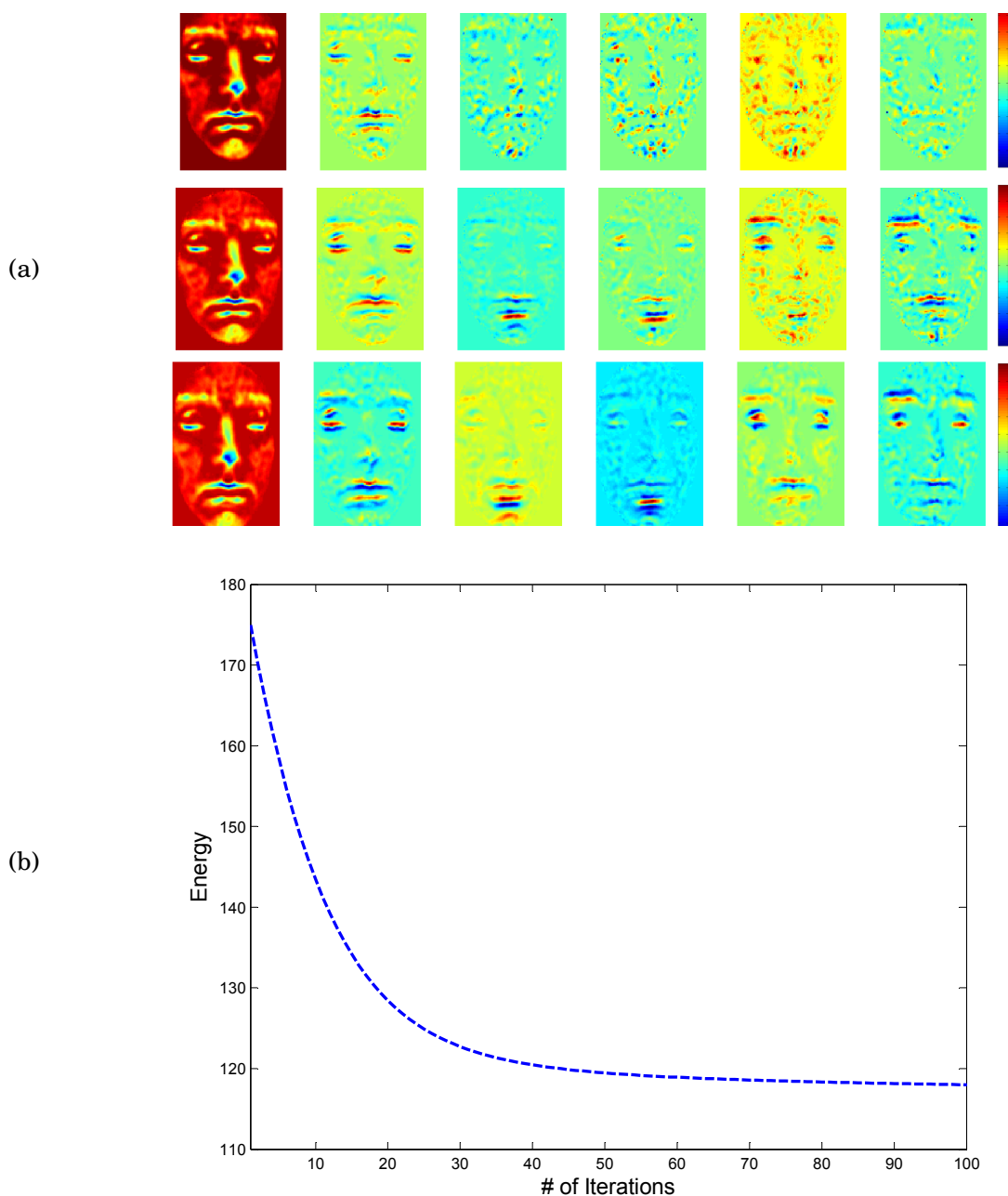


Figure 4.6: (a) Each row represents a sample mean subspace dimension computed on the subsequences of the same person with different expressions. The first 6 dominant singular-vectors are used to represent the sequences in each case. Three different window size are instead considered passing from the top to the bottom row ($\omega = 6, 25, 50$, respectively) where ω refers to number of 3D frames in the original 3D sequence; (b) The energy (i.e., $\|\bar{v}\|$) minimized in Algorithm 1 for estimating the mean subspace.

1492 **Illustration of Karcher mean computation**

1493 In Fig. 4.6(a) three *mean subspaces* obtained with the Karcher mean Algorithm pre-
 1494 sented in Algorithm 1 are shown, each of them computes the mean facial dynamics
 1495 for subsequences of the same person under different expressions. In each row, the first
 1496 six dominant singular vectors are reported, while the window size changes from $\omega = 6$,
 1497 to 25 and 50, from top to bottom, respectively. Considering the top row, we can notice
 1498 the first singular vector (first column) captures the main shape information of the face
 1499 across the sequence and expressions, which is the mean of the global 3D dynamic data,
 1500 and the second singular-vector captures the main deformation. Less relevant data are
 1501 included in the remaining singular vectors. This illustration shows clearly the main
 1502 motivation to choose the subspace representation. This observation (i.e., $k = 2$ is sufficient
 1503 for $\omega = 6$) is in agreement with the results reported in Fig. 4.4, where the information
 1504 Y_k captured by considering the first k singular-values reaches 90% considering just the
 1505 first two singular-values (in the case of window size $\omega = 6$). In contrast, in the second
 1506 and the third example of Fig. 4.6(a), the first column captures the mean shape, while
 1507 the remaining singular vectors are required to model the principal deformations of the
 1508 face. In Fig. 4.6(b), an example of the values of the energy (i.e., $\|\tilde{v}\|$) minimized over the
 1509 iterations of Algorithm 1 is also plotted.

1510 Figure 4.6 points out the relevance of using the subspace representation for modeling
 1511 the spatio-temporal behavior of the dynamic face. Besides, discarding less dominant
 1512 singular vectors allows us to remove the noise and redundancy in the original data.
 1513 The 3D shape representation obtained here by computing the mean curvature-maps
 1514 of the 3D face, which is relevant to such analysis. The mean subspace reflects the
 1515 shape information as well as the dominant deformations of the face in the subsequence
 1516 (window).

1517 These observations are confirmed in Fig. 4.7, where the visual illustration of the
 1518 mean computed on sets of subspaces corresponding to the same expressions of different
 1519 subjects are reported. In this Figure, each row corresponds to the mean of one of the
 1520 six universal facial expressions – *Angry, Disgust, Fear, Happy, Sad* and *Surprise* – as
 1521 conveyed by 3D dynamic sequences belong to 10 different people.

1522 The window size is set to $\omega = 50$ in each row (the first six dominant singular vec-
 1523 tors are shown). It is evident that each expression produces quite different dominant
 1524 deformations.

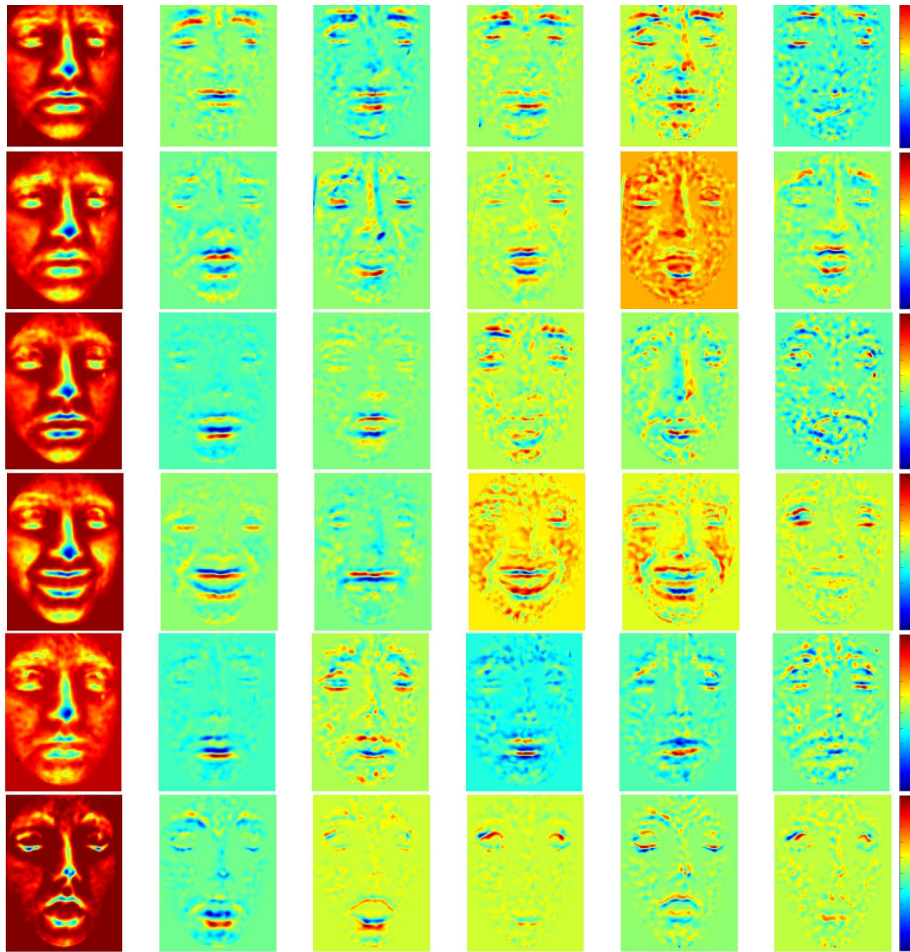


Figure 4.7: Visual illustration of mean subspaces. In every row of the six, we have one subspace computed from subspaces belonging to 10 different person but they were acting the same expression. Each row represents one of the six universal facial expressions, namely, from top to bottom: *Angry*, *Disgust*, *Fear*, *Happy*, *Sad* and *Surprise*.

1525 4.4.2 Grassmann Sparse Representation Classifier (GSRC)

1526 In this case, the classification is performed on the sparse representation computed
1527 according to sparse coding Algorithm 3 presented in Sect. 3.4.3.

1528 In fact, given a test sample, its sparse representation is first computed using the
1529 dictionary on the training samples. Consequently, conventional classification methods,
1530 like SVM or Nearest-Neighbor can be applied. An alternative solution is to use the
1531 Sparse Representation Classifier (SRC) proposed in [140].

1532 Algorithm 5 summarizes the main steps of the classification procedure. The main

1533 concept behind this classifier is to reproduce the testing query subspace from non-zero
 1534 sparse codes that belong to every class in the dictionary separately. Repeating this
 1535 class-specific estimation and computing the residual error between them and the original
 1536 query subspace gives a similarity measure. The estimation from the correct class should
 1537 give the minimum residual error for correct recognition.

1538 The Dirac function has been used in Algorithm 5 allows the selection of the coefficients
 1539 associated to the i^{th} class. That is, all the elements of this vector are set to be 0 except
 1540 those which correspond to the i^{th} class.

Algorithm 5 – Grassmann Sparse Representation Classifier

Require: Grassmann Dictionary $\mathbb{D} = \{\mathcal{D}_i\}_{i=1}^N \in \mathcal{G}_k(\mathbb{R}^n)$ where $\mathcal{D}_i = Span(D_i)$ with C classes, the
 test query $\mathcal{X} \in \mathcal{G}_k(\mathbb{R}^n)$ where $\mathcal{X} = Span(X)$ and $XX^T = \hat{X}$

Sparse code estimation of the query as in Algorithm 3

$$y^* \leftarrow \arg \min_y \|x^* - Ay\|^2 + \lambda \|y\|_1$$

for $i \leftarrow$ to C **do**

$$\varepsilon_i(\mathcal{X}) = \|\hat{X} - \sum_{i=1}^N y_i \hat{D}_i \text{dirac}_i(l_j - i)\|_F^2,$$

where l_j is the atom label

end for

Ensure: Identity(\mathcal{X}) $\leftarrow \arg \min_i (\varepsilon_i(\mathcal{X}))$

1541 In summary, face recognition is performed according to the following steps: (1) *Dictio-*
 1542 *nary learning* on the Grassmann manifold - given a training subset of observations, a
 1543 set of atoms (dictionary) is determined to describe the observations sparsely; (2) *Sparse*
 1544 *representation* - given a dictionary and a probe on the underlying manifold, the probe
 1545 is approximated using a sparse linear combination of atoms that belong to every class
 1546 from the dictionary separately; (3) *GSR-based classification* - once the training and
 1547 testing observations are expressed linearly using a sparse representation, it is possible
 1548 to perform the Grassmann Sparse Representation Classification.

1549 4.5 Experiments and results

1550 To investigate the contribution of facial dynamics in identity recognition using 4D data,
 1551 we conducted extensive experiments involving the BU-4DFE dataset. This dataset has
 1552 been collected at the Binghamton University [148] and used in several studies on 4D
 1553 facial expression recognition. To our knowledge, only two works, Sun et al. [128] and
 1554 Hayat et al. [61] have reported identification performance on this dataset. To allow a fair

1555 comparison with their study, we will consider in the following the same experimental
1556 setting.

1557 Before to present experiments and results, a summary of the main characteristics of
1558 the BU-4DFE dataset and its pre-processing is presented.

1559 **4.5.1 BU-4DFE dataset description and pre-processing**

1560 The BU-4DFE database consists of 101 subjects (58 female and 43 male, with an age
1561 range of 18 – 45 years old). It includes 606 3D model sequences with 6 universal expres-
1562 sions and a variety of ethnic/racial ancestries. Each participant (subject) was requested
1563 to perform the six prototypical expressions – *angry, disgust, fear, happiness, sadness,*
1564 *and surprise* – separately. The acquisition protocol requires each expression sequence
1565 to start and end with neutral facial states. Each expression was performed gradually
1566 passing from neutral, low intensity, high intensity, and back to low intensity and neutral
1567 (i.e., following the subsequent states *neutral-onset-apex-offset-neutral*).

1568 Actually, as a matter of fact, at a visual inspection some sequences evidence a wrong
1569 acquisition, starting with a non-neutral expression. In any case, each 3D sequence
1570 captures one expression at a rate of 25 frames per second, lasting approximately 4
1571 seconds, with about 35k vertices per 3D frame (or 3D mesh). As acquisition technology,
1572 the Di4D capturing system was used [148], which produces sequences of stereo images
1573 and computes 3D meshes of the face based on a passive stereo-photogrammetry approach.
1574 The resulting 3D frames of a sequence show a near-frontal pose, with some slight changes
1575 occurring mainly in the azimuthal plane. The scans are affected by large outliers, mainly
1576 located in the hair, neck and shoulders regions.

1577 In order to remove these imperfections from each 3D frame, an efficient pre-processing
1578 pipeline similar to [15] has been performed. The main steps of this pipeline are summa-
1579 rized as follows: (1) For each 3D frame, the holes are filled in; (2) The tip of the nose is
1580 detected, then the facial area is cropped using a sphere with radius of 90mm centered at
1581 the detected nose tip; (3) The pose of each 3D frame is normalized by registering it to the
1582 previous one using the Iterative Closest Point (ICP) algorithm. Once the pre-processing
1583 is performed, the mean curvature is computed from each 3D frame (Fig. 4.2). Then, the
1584 curvature-maps (images) are produced by projection, as described in Sect. 4.3. All these
1585 steps are implemented using the Visualization Toolkit (VTK) library¹.

¹<http://www.vtk.org>

1586 In the following, we report experimental evaluation and comparative analysis of the
 1587 proposed approaches using Grassmann Nearest-Neighbor (GNNC) classification on the
 1588 mean subspaces of each subject class, and Grassmann Sparse-Representation (GSR)
 1589 based classification computed on the sparse codes, with respect to the current literature.

1590 **4.5.2 Experimental setting**

1591 Following the protocol proposed in [128], 60 subjects have been considered out of the BU-
 1592 4DFE, and their sequences are partitioned into subsequences using a window size $\omega = 6$
 1593 (with a shifting step of 3 frames). This results into 30 sub-sequences extracted out of
 1594 every facial expression sequence of the 60 subjects (i.e., each sequence has approximately
 1595 90 frames). On these subsequences, experiments have been conducted following two
 1596 different settings:

- 1597 • *Expression Independent (EI)* – One expression per subject is used for training,
 1598 and this expression does not appear in the testing. All the other five expression
 1599 sequences are used for testing. Since 30 sub-sequences represent each expression
 1600 sequence, for the 60 subjects a total of $30 \times 60 = 1800$ subsequences is used for
 1601 training. Five expressions per subject are used for testing, i.e., for each subject
 1602 we have $5 \times 30 = 150$ test subsequences, with a total for all the 60 subjects of
 1603 $150 \times 60 = 9000$ subsequences;
- 1604 • *Expression Dependent (ED)* – For each sequence, the first half (from neutral to
 1605 nearby the apex of the expression) is used for training, while the remaining half
 1606 (from the apex of the expression to neutral) is used for testing. As a consequence,
 1607 the gallery and the probe samples convey similar dynamic behavior, though with
 1608 inverse temporal evolution. The number of training subsequences for every subject
 1609 is $15 \times 6 = 90$, with a total for the 60 subjects of $90 \times 60 = 5400$ subsequences. The
 1610 same number of subsequences is used for testing.

1611 **4.5.3 4D face recognition using GNNC**

1612 In this experiment, a window of six frames $\omega = 6$ and shifting step equals to 3 is used (the
 1613 same as in [128]), with only the first two dominant components kept for representing
 1614 the subspace ($k = 2$). The GNN-classification method is based on a gallery of subspaces,
 1615 one per subject, each computed as the mean of the training subsequences for the subject.
 1616 With the setting above, in the EI scenario, one complete expression is used to compute the

1617 mean for each subject, i.e. 30 subsequences; In the ED scenario, the mean is computed
 1618 on $15 \times 6 = 90$ subsequences with different expressions.

1619 Using the GNN-classifier, a comparison is performed between the ED and EI ex-
 1620 periments. Different distances are also considered, which involve the principal angles
 1621 between subspaces (see Sect. 3.3.5). The average recognition rates are reported in Ta-
 1622 ble 4.1.

Table 4.1: Recognition rates (RR%) for GNN-classification using different distances

Subspace Distance	ED – RR (%)	EI – RR (%)
Min Correlation	44.75	28.72
Binet-Cauchy	52.83	51.99
Geodesic	73.00	65.00
Procrustes	78.11	66.55
Max Correlation	92.61	67.12
Projection	93.69	68.88

1623 The observations can be derived from this Table are: (i) ED results outperform EI
 1624 results for each distance measure. This is expected, since in the ED setting there are
 1625 sequences of the same subject conveying the same expression both in the gallery and
 1626 probe sets (though with inverse temporal evolution); (ii) The different recognition rates
 1627 scored by the distances provide experimental evidence of the discriminative information
 1628 distribution across the principle angles. In particular, the highest recognition rate
 1629 obtained by the *Projection* distance shows that all the singular vectors, and consequently
 1630 the dynamic information of subsequences, helps in the recognition task by improving
 1631 the result obtained using just one principle angles (i.e., *Max Correlation* distance). The
 1632 lowest recognition rate is scored by the *Min Correlation* distance, suggesting us that the
 1633 subspaces on the manifold are sufficiently separated from each other, thus making them
 1634 well suited for the identity recognition task.

1635 Results reported in Table 4.1 have been obtained by comparing single instances
 1636 (subspaces) in the video. Since subsequences are part of a continuous video, it is possible
 1637 to fuse the decisions of successive subsequence instances to perform recognition. This al-
 1638 lows us to design an incremental recognition system over time, where multiple instances
 1639 are used to decide instead of only one. This idea has been implemented using a majority
 1640 voting fusion rule, at each time, using all available instances. The experimental results
 1641 are reported in Fig. 4.8 to show the performance at increasing size of the data have been
 1642 seen and analyzed along a sequence. From these plots, it is clear that the performance

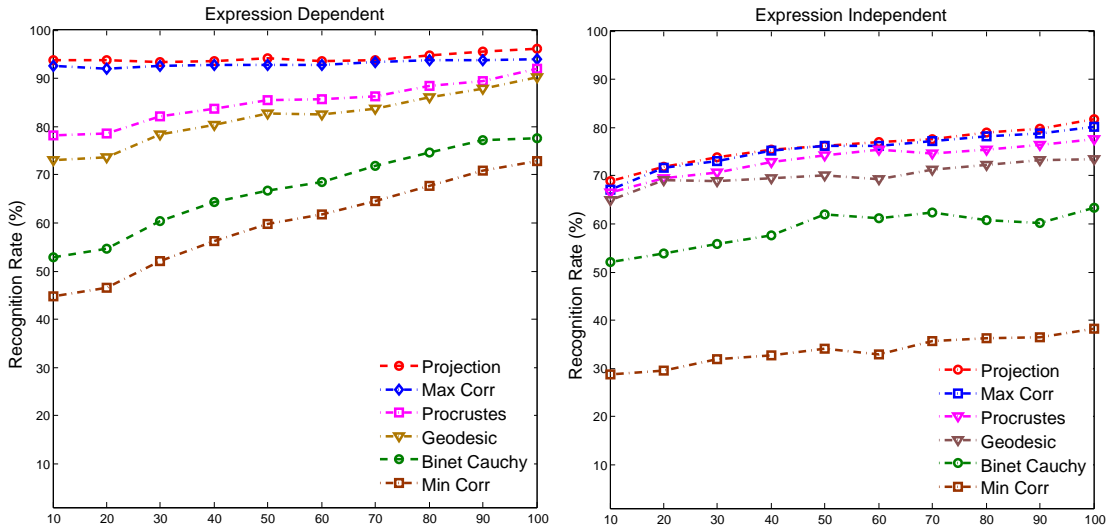


Figure 4.8: Trade-off between accuracy and latency (fraction of the video seen) for different Grassmann metrics/distances in the ED and EI settings.

1643 increase by having longer fraction of the 3D video. This observation is the same, under
 1644 ED and EI settings.

1645 4.5.4 4D face recognition using GSRC

1646 In these experiments, we use the proposed solution based on Grassmann Sparse Repre-
 1647 sentation algorithm presented before (GSR). A variant of the GDA Grassmann Discrimi-
 1648 nant Analysis algorithm [56], called GGDA (Graph-embedding GDA) [60] is also used
 1649 as a baseline to evaluate the effectiveness of the GSR algorithm. In practice, the flow
 1650 of curvature-maps, for the window of size ω is first mapped to the Grassmann manifold
 1651 using SVD. Then, the steps described in Sect. 4.4.2 are performed for training and testing.
 1652 Results under the ED and EI settings are reported. A comprehensive discussion of the
 1653 experimental results, when varying the window size ω , and the subspace order k is also
 1654 reported.

1655 Expression Independent (EI) experiment

1656 As a preliminary experiment, we investigated the effect of the subspace order k on the
 1657 performance. To this end, we apply the GSR algorithm with a varying $k \in \{1, 2, 3, 5, 6\}$,
 1658 while keeping a fixed window size $\omega = 6$ and shifting step equals to 3. So, in this case we

1659 have 30 training subspaces for subject, for a total of 1800 subspaces in the training set
1660 (dictionary).

1661 The subspace order k is also related to the information carried by the respective
1662 eigenvalues through the measure Y_k (see Eq. (4.1)). As shown in Table 4.2, the highest
1663 average recognition rate is 84.13%, obtained for $k = 2$. This rate is 3% higher than the
1664 average recognition rate obtained for $k = 1$ (using only the first dominant left-singular
1665 vector, which corresponds to the common data over the window).

Table 4.2: EI experiment: Effect of the subspace order k on the recognition rate for the GSR algorithm. Subsequences with window size $\omega = 6$ have been used in all the cases

Subspace order k	1	2	3	4	5	6
Y_k (%)	81	90	94	96	98	100
RR (%)	81.03	84.13	81.76	81.22	80.94	80.02

1666 This allows us to make two main conclusions: (i) The importance of the facial dynamics
1667 in improving the recognition performance. In fact, the optimal parameter $k = 2$ implies
1668 that the mean and the first dominant deformations are important in the recognition
1669 process. They are given by the first and the second singular-vectors of the orthogonal
1670 matrix, respectively; (ii) The remaining left-singular vectors are less relevant in the
1671 recognition process, including the noise which is present in the 4D acquisition. We
1672 note that $k = 2$ allows capturing in average about 90% of the data available in the 4D
1673 sub-sequence. Based on these empirical observations, in our next experiments, we will
1674 consider 90% of the information for different window size (ω).

1675 We are interested now in studying the effect of varying the size of the window on
1676 the performance. In the following experiment, we have varied this parameter in the
1677 set $\omega \in \{6, 10, 15, 20, 25\}$. The subspace order k is defined as the number of left singular
1678 vectors, which retains 90% of the original data. The corresponding recognition accuracy
1679 are reported in Table 4.3. It can be seen that the optimal window size is $\omega = 6$ for both
1680 the GSR and the GGDA algorithms.

1681 The reason behind the decreasing accuracy at increasing size of the window is the
1682 lack of temporal registration of the curvature-maps. In fact, a large difference between
1683 the frames across the window affects negatively the orthogonalization procedure, which
1684 assumes dense correspondence between the frames. Interestingly, the accuracy obtained
1685 using the GSR (84.13%) substantially improves the accuracy achieved using the GGDA
1686 (64.24%), and the GNN-classification (68.88%). This result also evidences the efficiency

1687 of sparse coding of subspaces in comparison to the discriminant analysis, which can be
 1688 affected by the points distribution over the Grassmannian manifold.

Table 4.3: EI experiment: Effect of the window size ω on the recognition accuracy for the GGDA and GSR algorithms. The subspace order k is set to keep 90% of the information

ω, k	Algorithm	
	GGDA – RR(%)	GSR – RR(%)
6, 2	64.24	84.13
10, 4	61.15	79.89
15, 6	56.61	76.55
20, 9	50.50	76.59
25, 11	50.60	75.80

1689 Table 4.4 provides additional details by reporting the recognition rates obtained
 1690 separately for each test expression, by the GGDA and GSR algorithms, and the approach
 1691 proposed in [128]. The average recognition rate achieved by GSR is 84%, which is about
 1692 10% lower than the accuracy reported in [128]. However, differently from the approach
 1693 proposed by Sun et al., the proposed solution does not require any manual or automatic
 1694 landmarking of the face, and it is computationally more efficient. In addition, the dense
 1695 (vertex-level) registration of the 3D frames, which is computationally complex and time-
 1696 consuming and is not performed in our method. On an opposite side, this operation
 1697 permits the approach presented in [128] to achieve comparable results throughout all
 1698 the expressions. In our case instead, we observe the RR decreases by 4% in the case of
 1699 posed surprise expression, which includes topological variations of the face (i.e., mouth
 1700 open). Another methodological difference between the two approaches is that Sun et al.
 1701 designed and trained two separate HMMs called spatial and temporal. In our approach,
 1702 only 2 singular vectors are used to encode the spatio-temporal information of a 3D facial
 1703 sequence and can be used to perform GSR classification.

1704 The recognition performance of our solution can be improved by using an increasing
 1705 fraction of the video. This implies that more than one instance (subsequence) is used to
 1706 recognize a subject. With this approach, the overall performance of GSRC increases from
 1707 84.13% (using only one instance, which represents about 5% of the video) to 95.11% using
 1708 the whole video (about 4s). This is illustrated in Fig. 4.9, separately for each expression.
 1709 This Figure also confirms the difficulty in recognizing subjects which convey the *Surprise*
 1710 expression.

Table 4.4: EI experiment: Recognition rate obtained using different training expressions compared to the approach in [128]

Training Expression	Method		
	Sun et al. [128]	GGDA	GSR
Angry	94.12%	61.26%	85.20%
Disgust	94.09%	68.54%	87.70%
Fear	94.45%	69.02%	83.49%
Happy	94.52%	68.56%	83.36%
Sad	93.87%	63.05%	84.86%
Surprise	95.02%	56.07%	80.49%
Overall	94.37%	64.42%	84.13%

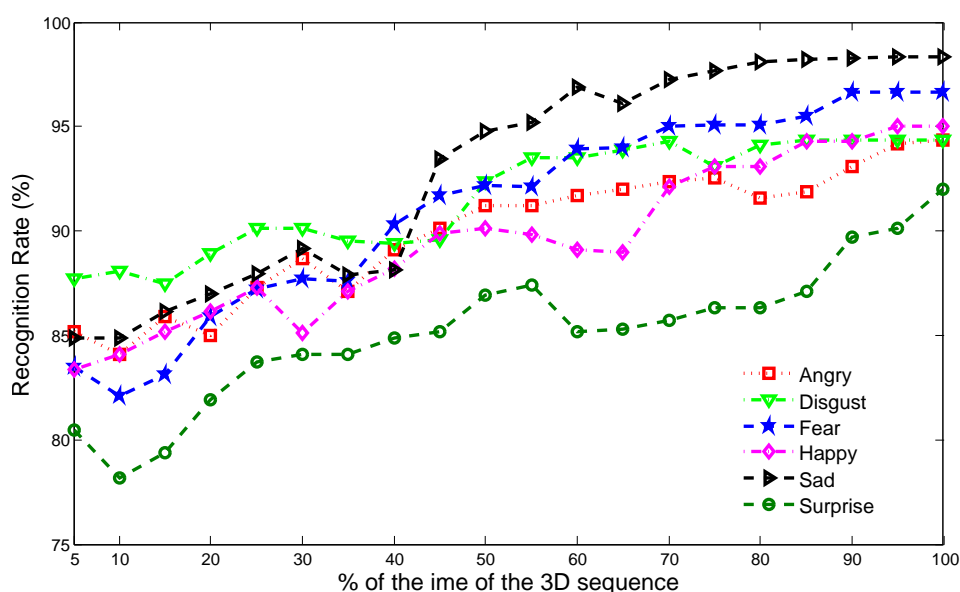


Figure 4.9: EI Experiment: Trade-off between accuracy (RR%) and latency.

1711 In the experiments presented above, only one expression is considered for (identity)
1712 training. We have also analyzed the results in the case the training is performed with
1713 five expressions, i.e., 9000 for training (150 for each subject), and 1800 for testing (30
1714 per subject), while the test is performed on subsequences from the remaining expression.
1715 Results are reported in Table 4.5, which provides a comparison when training with one
1716 expression versus training with five. Comparison of these results (using GSRC) shows
1717 that increasing the number of samples and their dynamics (even though they come

1718 from different expressions) can significantly increase the recognition rate from 84.13% to
 1719 93.37%.

1720 We can also observe that recognizing the subject identity under *Surprise* expression
 1721 is the most difficult case among the six expressions, due to the large shape changes,
 1722 where identity recognition under *Sad* expression is the easiest across the time.

Table 4.5: Impact of the training set on the performance: training based on only one expression vs. training based on five expressions

Testing Expression	Training by one	Training by five
Angry	83.27%	94.50%
Disgust	78.42%	96.30%
Fear	92.21%	98.13%
Happy	86.23%	93.20%
Sad	94.32%	97.73%
Surprise	69.75%	80.40%
Overall	84.13%	93.37%

1723 Expression Dependent (ED) experiments

1724 In this experiment, the window size is $\omega = 6$, with shifting step, equals to 3, and 30
 1725 sub-sequences are obtained from each facial expression sequence, half of which is used
 1726 for training and a half for testing. Thus, we have 90 training subspaces per subject, and
 1727 a dictionary of 5400 subspaces.

1728 The GSR-based classifier is used in this experiment. Table 4.6 reports the results
 1729 obtained using the GSR and the GGDA algorithms on 3D dynamic sequences (4D).
 1730 In addition, for comparison purposes, we also reported in the Table several results
 1731 from [128], including Gabor wavelets on 2D videos, LLE, PCA and LDA on 3D static
 1732 data, and the ST-HMM on 4D data.

1733 It can be seen that both GGDA and GSR outperform state of the art approach. In
 1734 particular, their accuracy is close or equal to 100% under the ED-setting. Our explanation
 1735 of the higher accuracy achieved by the GGDA and GSR compared to existing methods
 1736 is that the optimized SVD-based orthogonalization produces a matrix independent of
 1737 the time-order of the 3D video clips. That is, comparing two video clips taken from
 1738 the Onset-Apex and the Apex-Offset gives small distance as the temporal order of the
 1739 curvature-maps is ignored. This demonstrates the efficiency of using the Grassmann

Table 4.6: ED-experiment: Comparison between the recognition accuracy obtained for the methods proposed in this works, and for the 2D video, 3D static, and 3D dynamic (4D) approaches reported in [128]

Method	RR (%)
Gabor-wavelet on 2D videos (from [128])	85.09
LLE on static 3D (from [128])	82.34
PCA on static 3D (from [128])	80.78
LDA on static 3D (from [128])	91.37
ST-HMM on 4D [128]	97.47
GNN on 4D	93.69
GGDA on 4D	98.08
GSR on 4D	100

1740 representation and learning methods defined on in for solving 4D face recognition
1741 problem.

1742 4.5.5 Comparative study and discussions

1743 From the experimental results reported above, it emerges the proposed approach, which
1744 combines Grassmann representation with an extrinsic learning method achieved promis-
1745 ing results in 4D face recognition. We have demonstrated, through extensive experiments,
1746 the contribution of the facial dynamics in the recognition process. In Table 4.7, we sum-
1747 marize the obtained results under the ED and EI settings. We also studied the advantage
1748 of using the dynamic of shape (3D videos) compared to the dynamic of appearance (2D
1749 videos), as reported in the Table with comparison with Sun et al. [128].

Table 4.7: ED and EI results for 2D and 3D videos

Method	EI - RR (%)	ED - RR (%)
2D video A-HMM [83] (from [128])	67.05	93.97
4D ST-HMM [128]	94.37	97.47
4D GSR	84.13	100

1750 It is clear from these results that the 3D video modality outperforms the 2D video
1751 modality. That is, the dynamics in 3D facial shapes has more discriminating power
1752 compared to the dynamics of 2D facial images. When the proposed approach is compared
1753 with [128], it is evident that the latter performs better in the ED case, where sequences

1754 with different expressions are compared. This indicates the effect of using registration
 1755 and tracking technique for the robustness against expression differences.

1756 This is mainly due to the dense temporal vertex-tracking approach required before
 1757 training the HMMs. However, this comes at the cost of an increased computational com-
 1758 plexity of the tracking, in addition to the required accurate manual/automatic landmarks
 1759 detection in the first 3D frame of a sequence.

Table 4.8: Processing time of the proposed pipeline compared to [128]. A 3.2GHz CPU was used in [128], compared to the 2.6GHz CPU used in our work

Processing Step	Processing time (s)	
	Sun et al. [128]	This work
One 3D frame processing	15	1
One probe recognition	5	0.73
Full video processing - 100 frames	1500	90

1760 The computational aspect is evaluated in Table 4.8, which reports the processing
 1761 time of the proposed pipeline compared to [128]. From the Table, it emerges the proposed
 1762 approach is less demanding in processing time. While the method presented in [128]
 1763 includes time-consuming mesh processing steps, such as conformal mapping, generic
 1764 model adaptation and vertex-level tracking across the video, our approach benefits from
 1765 the subspace modeling methodology and sparse coding techniques over the underlying
 1766 manifold to keep the approach computationally cheap. In addition, it does not use manual
 1767 or automatic landmark detection and tracking of the face.

1768 **4.6 Towards 4D face recognition in adverse** 1769 **conditions**

1770 Since most of current 3D dynamic datasets and 4D face recognition works are limited
 1771 to one face recognition problem that is the facial expressions, several other important
 1772 problems still not explored like pose variation, occlusion talking, walking, etc. In this
 1773 section, we present a new 3D/4D dynamic facial database collected basically to address
 1774 4D face recognition challenges in real world scenarios. Also, the subspace metric-based
 1775 approach is implemented to evaluate the performance of this approach under such
 1776 difficult scenarios in 3D unconstrained videos.

1777 **4.6.1 The full 3D/4D face recognition database**

1778 All the available 3D dynamic databases are created to address the problem of facial
1779 expressions and action units recognition as it can be seen from the literature review in
1780 Section 2.8.2. This new 3D dynamic face recognition database implies several common
1781 challenges which have not been considered in 3D dynamic before. It is collected using
1782 single-view 3D *Artec* scanners with temporal resolution around 15 frames per second.
1783 This database can make a contribution in 4D FR research, especially for non-constraint
1784 scenarios.

1785 There are 58 subjects in this database, 23 females and 35 males. The age average is 23
1786 years old from different ethnics groups. For each subject, we collected first a full 3D static
1787 high-resolution model using the *Artec MHT* 3D scanner with the texture information. the
1788 average vertices in every 3D model about 50 *k* vertices. Figure 4.10 shows an example of
1789 a 3D static model from this database with and without texture information.

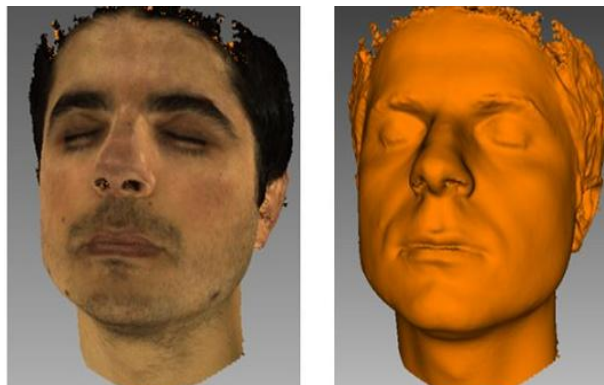


Figure 4.10: Full 3D static model from the database with and without texture information

1790 Second, for every subject, eight 3D videos of 20 seconds using the *Artec L* 3D scanner
1791 are recorded. These eight videos are: one segment for the following challenges: facial
1792 expression, talking, walking, internal occlusion by hand or hair, external occlusion by
1793 scarf or sunglasses, and multiple persons (two or three) and two neutral videos. We
1794 refer by neutral that there is no facial expressions or occlusion. All of these videos were
1795 recorded under free pose variation in front of the scanner. Since the scanner has been
1796 used is a single view scanner, we have only a part of the face in many phases of the video
1797 as it is depicted in Fig. 4.11. This database is available for public research use.

1798 More details about the acquisition protocol, settings and database properties, are
1799 published in [5].



Figure 4.11: The 3D dynamic sequences acquired under different conditions: a) neutral; b) expressive; c) talking; d) internal occlusion by hand; e) external occlusion by sunglasses; f) walking and g) multiple persons.

1800 4.6.2 Preliminary experiments and results

1801 To validate this new database, we applied a metric-based subspace learning approach to
 1802 recognize the identity similarly to the framework proposed in Sect. 4.3. Here, different
 1803 techniques are used to address the new challenges of this new dataset. The problem of
 1804 pose variation is solved by dividing the long video into short videos of size 15 frames (i.e.
 1805 about 1 second) where they have one nearby pose. The normal vector is estimated at

1806 each vertex for two reasons: First, to make a dense correspondence between successive
 1807 frames using normal shooting technique presented in [30]. This normal shooting was
 1808 used to track roughly the vertices through one subsequence to have registration. Second,
 1809 the map of z component values of the estimated normals are used as a spatial feature
 1810 vector for every frame. Before that, a down-sampling step is applied to each frame, to
 1811 produce a constant number of n vertices per frame. These feature vectors are vectorized
 1812 as columns of one matrix and k – SVD orthogonalization is applied to find the subspace
 1813 representation of the original data. These steps are illustrated in Fig. 4.12.

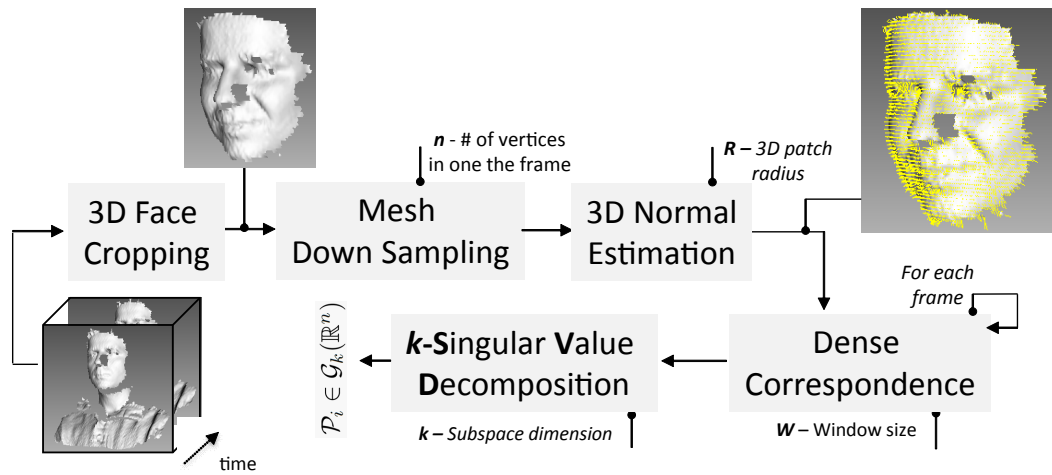


Figure 4.12: Overview of 4D to 4D FR approach under adverse conditions.

As a result of this pipeline, each 4D fragment is viewed as an element of the Grassmannian, and the original problem of 4D-to-4D matching is turned into a distance measurement on Grassmann which can be formulated as follows:

$$(4.2) \quad g^* = \operatorname{argmin}_i d_{Geo}(\mathcal{X}_{probe}, \mathbb{X}_{g_i}),$$

1814 where $d_{Geo}(\cdot, \cdot)$ denotes the geodesic distance between two linear subspaces, and g^* is the
 1815 closer fragment in the gallery set \mathbb{X}_{g_i} to the probe fragment \mathcal{X}_{probe} according to the used
 1816 distance. Furthermore, using the Riemannian geometry on Grassmann manifold makes
 1817 it possible to use other mathematical computations, such as mean computation and
 1818 k-means clustering explained in Sect. 3.4. As it is explained above, to solve the problem
 1819 of pose variations the sequence of each subject in the gallery is divided into multiple
 1820 instances over time. The same procedure is applied to probe sequences. Thus, each 3D
 1821 temporal fragment of a probe will be compared with all 3D temporal fragments in the
 1822 gallery. This exhaustive search can be avoided by applying k-means clustering algorithm

1823 on the gallery instances to cluster them according to the main pose of the 3D frames.
 1824 After applying this unsupervised clustering, each cluster uses the *Karcher* mean [73]
 1825 algorithm on all elements included in the cluster to have a representative mean subspace.
 1826 In this way, each probe sequence is compared just with the clusters' representative in
 1827 order to recognize the probe pose first, and then it will be compared only with gallery
 1828 fragments that have the same pose only. Figure 4.13 illustrates instances from the same
 1829 subject or from different subjects that have similar poses grouped in the same class.

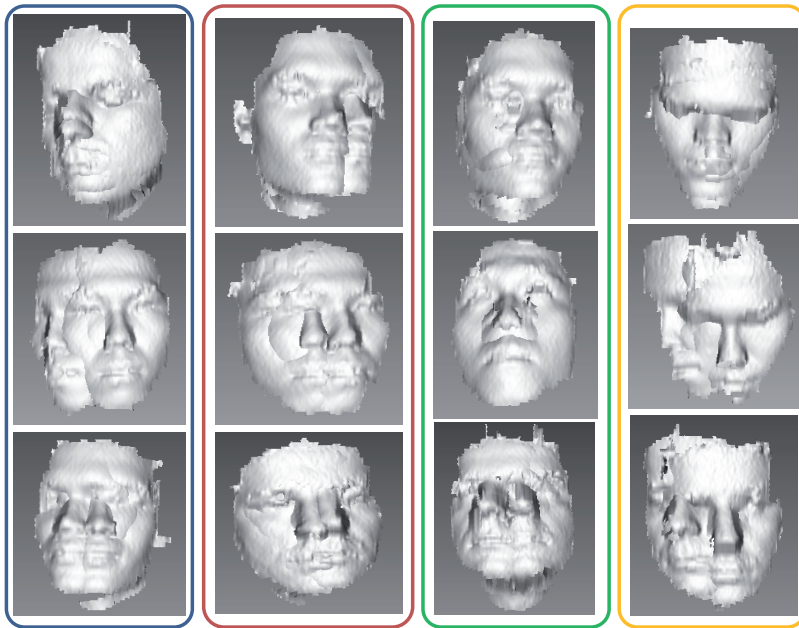


Figure 4.13: Each column shows instances belong to different subjects clustered together due to their nearby poses.

1830 For evaluation, we considered the 58 subject of the database. One of the neutral
 1831 3D dynamic sessions is taken as a gallery. After dividing the 20 seconds videos into
 1832 short subsequences, there are 20 subsequences resulted for every subject, and they are
 1833 clustered into 5 classes according to their poses. The mean of each class is computed
 1834 offline as well. For testing, 4 scenarios are considered: Neutral (Ne), Facial expression
 1835 (Fe), talking (Tk), and external occlusion (EO) for every subject. The subject 3D video
 1836 that contains these scenarios are tested separately after dividing every video into 20
 1837 subsequences as has been done for the gallery. Recognition process includes comparing
 1838 the probe subsequence with the mean of gallery clusters to estimate its pose first, then
 1839 comparing it with the instances that belong to this pose to find the identity. Applying

1840 majority voting concept to have more robust decision using more than one instances is
1841 implemented. The obtained recognition rates for these four scenarios (Ne, Fe, Tk, and
1842 Eo) are equal to 72%, 62%, 65%, and 36%, respectively.

1843 Although the results obtained from this dataset is lower than those have been ob-
1844 tained on BU-4DFE database, the considered challenges in each scenario are more
1845 difficult, and these primary experience results can be improved by adopting more ad-
1846 vanced techniques for faces registration, feature extraction, and learning. More details
1847 about this experimental study can be found in [6].

1848 4.7 Conclusion

1849 In this chapter, we have proposed a comprehensive 4D face recognition framework, which
1850 adopts a subspace-learning methodology and exploiting the efficiency of low dimensional
1851 subspace compact representation of the high dimensional data. While this direction
1852 has been widely used in the 2D domain, to our knowledge, this is the first study which
1853 brings it to the 3D domain for face recognition problem. As a contribution to our study,
1854 we have demonstrated that the shape dynamics (behavior) improves the recognition
1855 accuracy. This conclusion is valid even if the training samples (in the gallery) and the
1856 probes (to be recognized) present a different facial behavior. Leveraging the geometry of
1857 Grassmann manifolds, relevant geometric tools, and advanced Machine Learning tools,
1858 i.e., dictionary learning and sparse coding on the underlying manifold and comparing
1859 its performance with intrinsic learning methods like the Karcher mean computation.
1860 This approach is capable of managing face recognition from dynamic sequences of
1861 3D scans in an effective and efficient way. The main advantages of this framework
1862 are: It is completely automatic and computationally less demanding compared to the
1863 current literature. Evaluation on BU-4DFE database is conducted, and obtained results
1864 outperform previous approaches under the expression-dependent setting and better
1865 performance than 2D video and 3D static based approaches. An empirical analysis
1866 for proposed approach parameters is reported as well. The importance of exploiting
1867 more than one instance to make recognition decision (majority voting through the time)
1868 advantage validated on expression independent scenario. A performance comparison
1869 of the different defined distances in Grassmann Nearest Neighbor classifier shows the
1870 superiority of projection distance over all others.

1871 To bring face recognition from 3D dynamic sequences to more realistic scenarios,
1872 new 3D/4D facial database has been collected containing several challenges like pose

1873 variation, facial expressions, talking, walking, internal and external occlusion and mul-
1874 tiple persons in the scene. Experimental analysis for a primary metric-based subspace
1875 learning approach for 4D to 4D face recognition on this new challenging database is
1876 reported.

1877 In the following Chapter 5, we will address another main application for 3D dynamic
1878 sequences analysis which is spontaneous emotional states and pain affect early detection
1879 from depth and 3D high-resolution dynamic data by analyzing trajectories of subspaces
1880 on Grassmann manifolds.

SPONTANEOUS EMOTION DETECTION IN 4D DATA

5.1 Introduction

1881 One of major field of interest in facial sequences analysis is emotions and affects recog-
1882 nition and detection. Most of the current facial expression recognition works in the
1883 community consider the six prototypical (basic) expressions derived from psychological
1884 study proposed by Ekman [44] and they include *anger*, *disgust*, *fear*, *happiness*, *sad-*
1885 *ness* and *surprise* which are collected in acted manner. These posed expressions are
1886 different from spontaneous and genuine expressions that are more complex. A more
1887 recent alternative to the hard categorical description of human affect is the *dimensional*
1888 *description* [111] in which an affective state is characterized in terms of a small number
1889 of latent dimensions, rather than a small number of discrete emotion categories. The
1890 dimensional description of emotions is shown in Fig. 5.1 using the *Arousal-Valence*
1891 chart. On the horizontal axis, the evaluation dimension is accounted, from displeasure to
1892 pleasure; on the vertical axis, the activation dimension is accounted through the arousal
1893 state, varying from low-to-high.

1894 In this chapter, we exploit 3D dynamic data representation on Grassmann manifolds
1895 as **trajectories**, for the purpose of online spontaneous emotion detection, such as happi-
1896 ness or physical pain from depth or 3D videos. Our approach consists of mapping the
1897 video streams onto a Grassmann manifold (i.e., space of k -dimensional linear subspaces)
1898 to form time-parameterized trajectories. To this end, depth videos are decomposed into
1899 short-time clips, each approximated by a k -dimensional linear subspace, which is in

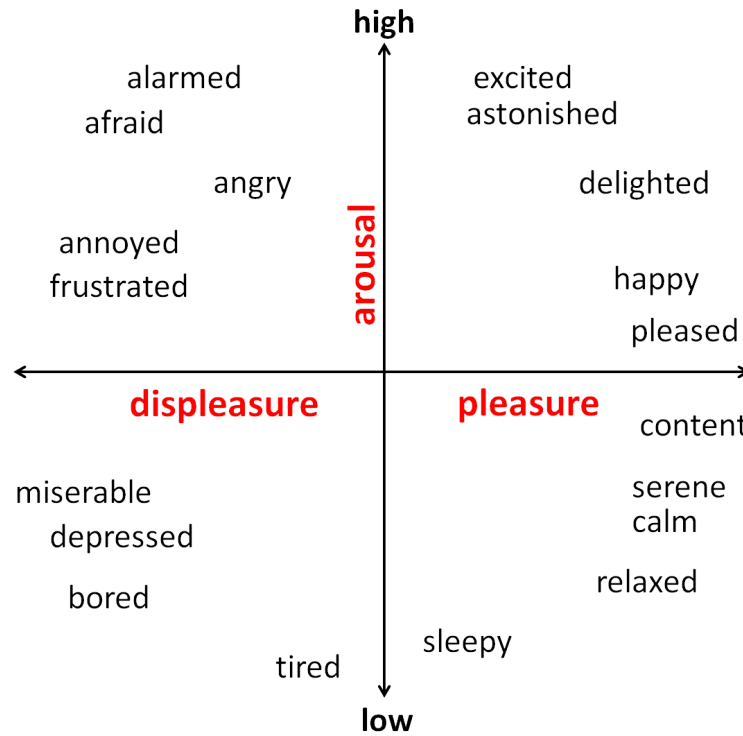


Figure 5.1: Dimensional Arousal-Valence chart of human emotions.

1900 turn a point on the Grassmann manifold that captures the embodied information in
 1901 the video at that portion. Then, the temporal evolution of subspaces gives rise to a
 1902 precise mathematical representation of trajectories on the underlying manifold. In the
 1903 final step, extracted spatio-temporal features based on computing the velocity vectors
 1904 along the trajectories, termed Geometric Motion History (GMH), are led to an early
 1905 event detector based on Structured Output SVM. The SO-SVM enables online emotion
 1906 detection in the 3D video from partial and complete data. Experimental results obtained
 1907 on the publicly available Cam3D Kinect [90] and BP4D-Spontaneous databases[155]
 1908 validate the proposed solution. The first database has served to exemplify the proposed
 1909 framework using depth sequences of the upper part of the body (4D-bodies) collected
 1910 using depth-consumer cameras, while the second database allowed the application of
 1911 the same framework to physical pain detection from high-resolution and long 4D-face
 1912 sequences.

1913 The rest of the chapter is organized as follows: In Sect. 5.2, we outline the main ideas
 1914 and contributions of the proposed approach; A discussion of the 3D video representation
 1915 adaptation to an early event-detector framework, which permits emotion detection from

1916 a 3D dynamic sequence is presented in Sect. 5.3; The pain detection from 4D data is
 1917 presented in Sect. 5.4; We showcase the potential of the proposed solution in Sect. 5.5, by
 1918 reporting results on the Cam3D Kinect database and BP4D-Spontaneous high-resolution
 1919 database; Finally, our conclusion is in Sect. 5.6.

1920 5.2 Methodology and contributions

1921 In this chapter, we propose an online approach that detects the emotional state from
 1922 3D dynamic data as early as possible. The proposed framework is evaluated on two
 1923 challenging problems: (a) Early detection of spontaneous emotional states from depth
 1924 sequences of the upper part of the body (*depth-bodies*) acquired with a low-resolution
 1925 sensor. Here, the spontaneous emotions derived from the dynamics of facial expressions
 1926 and upper body gestures together; (b) Early detection of spontaneous physical pain affect
 1927 from 4D high-resolution facial sequences (*4D-faces*).

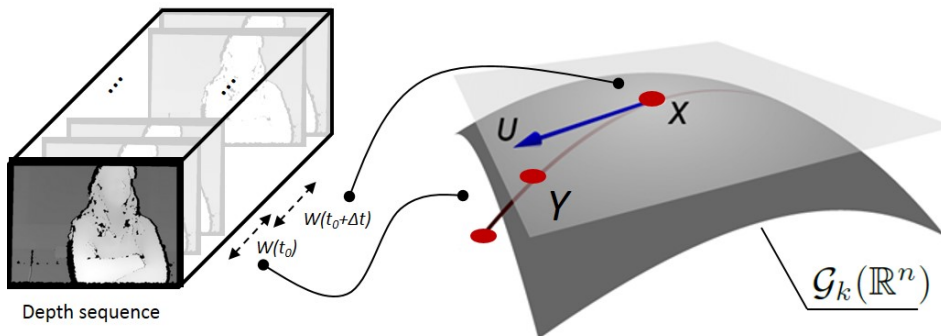


Figure 5.2: Dynamic depth data representation as trajectories on the Grassmann manifold $\mathcal{G}_k(\mathbb{R}^n)$. The streams of depth data at the left, are mapped to associated trajectories on the Grassmannian (right).

1928 The main contribution has been introduced here is a new representation of human
 1929 space-time 3D/depth data and relevant processing tools. In fact, several inherent chal-
 1930 lenges arise when analyzing depth videos. The most relevant one derives from the
 1931 non-linearity of the space-time data. The non-linearity is caused by face deformations or
 1932 the body gestures. In addition, the rigid transformations, mainly rotations and transla-
 1933 tions, which span other challenging problems, like missing data. In fact, human body
 1934 acquisition using depth sensors or single-view 4D scanners includes auto-occlusions
 1935 (the occlusion of the body by itself). In the literature, solving these issues requires pose

1936 normalization as well as temporal registration along the depth-video, which are time-
1937 consuming when processing dense data [128]. In our proposed approach, we account for
1938 the non-linearity of the data and related transformations as follow: First, we assume
1939 linearity in a local (short) time interval, by grouping the depth frames into subsequences
1940 of predefined length and regarding each group as a linear subspace (i.e., span of an
1941 orthonormal basis, represented by a matrix). This matrix gives rise to an element on a
1942 specific well-known Riemannian manifold (Grassmannian manifold); Then, we generalize
1943 it to longer videos using curves (i.e., non-linear) on the underlying curved manifold. This
1944 manifold-mapping allows faithfully representing the original depth and 3D video data in
1945 a cheaper and effective way, and it also shows robustness to noisy and missing data. This
1946 latter aspect makes the proposed representation suitable for processing and analyzing
1947 videos acquired with depth-consumer cameras, which suffer from low-accuracy and noisy
1948 depth measurements as well as incomplete data. Finally, using a Structured Output
1949 SVM (SO-SVM) based on sequential analysis of Euclidean spatio-temporal features, our
1950 framework is also endowed with online affect state detection capability, thus permitting
1951 early event detection.

1952 Figure 5.2 summarizes the idea of mapping short-time depth video clips to a Grass-
1953 mann manifold $\mathcal{G}_k(\mathbb{R}^n)$, where k is the dimension of subspaces, and n the ambient space
1954 dimension. The positions of points corresponding to successive clips capture the temporal
1955 evolution (i.e., dynamics) of the face or the body in 3D videos, shown as a trajectory on the
1956 manifold. In particular, the temporal evolution of neighboring points across the trajectory
1957 is regarded as a one-dimensional feature vector, called *Geometric Motion History (GMH)*
1958 descriptor, which constitutes the input to the SO-SVM early event detector. In summary,
1959 the main contributions of this part are:

- 1960 – A novel representation based on trajectories on Grassmann manifold suitable
1961 for modeling 3D/depth sequences and inherent human motions (deformations,
1962 gestures, etc.) of non-linear nature;
- 1963 – A new space-time features vector termed *GMH*, which captures the spatio-temporal
1964 information to analyze the dynamic facial or body data 3D data;
- 1965 – An adaptation of the early event detector developed by Hoai and De la Torre [63]
1966 for sequential analysis of Grassmann trajectories. In so doing, we report a clear
1967 benefit in early spontaneous emotion detection using the upper part of the body,
1968 rather than the face alone, and the efficiency in pain affect detection from 3D
1969 high-resolution facial expression sequences.

1970 The proposed framework is also the first one, to our knowledge, capable of addressing
 1971 early detection of spontaneous emotions in a complex scenario that includes:

- 1972 – Depth sequences of the upper part of the body acquired with a cost-effective Kinect
 1973 camera;
- 1974 – Spontaneous emotions acquired without a rigid protocol (i.e., no assumption on the
 1975 time when the emotion occurs in the sequence);
- 1976 – Emotional state detection does not depend only on the temporal dynamics of the
 1977 3D face deformations but also on the upper part of the body, including shoulders
 1978 and arms;
- 1979 – Early detection of spontaneous physical pain from 4D high-resolution sequences.

1980 **5.3 Emotion detection from Kinect depth-bodies**

1981 In this scenario, videos of the upper part of the body (face, neck, shoulders and arms/hands)
 1982 are acquired using a depth-consumer (Kinect) camera.

1983 The first processing step consists in segmenting the upper part of the body from the
 1984 background in each depth frame of the observed videos. Then, the sequence of the cropped
 1985 upper body is divided into successive short-time clips, based on a temporal window size
 1986 ω . For each clip, the cropped depth data (of each frame) of the body are reshaped to a
 1987 vector of size n , which is then arranged to a matrix $X \in \mathbb{R}^{n \times \omega}$. Applying k -SVD to X , i.e.,
 1988 $X = U\Sigma V^T$, the subspace spanned by the columns of the matrix $U \in \mathbb{R}^{n \times k}$ is retained to
 1989 represent the original clip. As a result, a video comprising m subsequences of size ω , and
 1990 each of them is mapped to represent k -dimensional linear subspaces which lies on the
 1991 Grassmann manifold $\mathcal{G}_k(\mathbb{R}^n)$. These points define a corresponding time parameterized
 1992 trajectory on the manifold $\mathcal{T}(t)$ as discussed in Section 3.5.1, where every subspace here
 1993 is a time instance.

1994 This representation by trajectories on Grassmann manifold allows us to reduce
 1995 the effect of the noise of the acquired depth data, and constitutes an efficient way to
 1996 sequentially analyze the video streams (when observed) and extract relevant space-time
 1997 features for online emotion detection. Our idea here is to compute first-order derivatives
 1998 of the trajectory, and build a history of the motion including both deformations and pose
 1999 changes. In so doing, the rhythm and the amplitude of the motion can be captured using
 2000 the norm of the derivation.

2001 **5.3.1 Geometric Motion History (GMH)**

2002 In this work, we introduce a mono-dimensional feature vector to capture a spatio-
2003 temporal description for the 3D dynamic video from its representation as trajectory
2004 of subsapces on the Grassmann manifold. From this 4D-depth bodies, this GMH will
2005 be built from the instantaneous speed along trajectories as presented in Section 3.5.2.
2006 More in details, trajectories on Grassmann manifold can be analyzed by considering
2007 the evolution of their instantaneous speed. Given an observed portion of the trajectory
2008 $\mathcal{T}(t)$ in the time interval $[0, t]$, the instantaneous speed can be computed as the distance
2009 between neighboring points $\mathcal{X}(t)$ and $\mathcal{X}(t + \delta)$ along the trajectory, where δ is an integer
2010 constant added to control the evolution step between considered subsapces of the tra-
2011 jectory. The length of the shortest path is computed (Geodesic distance) on Grassmann
2012 manifold between the elements of the trajectory with step δ to build the *Geometric*
2013 *Motion History (GMH)* that characterizes the temporal motion of this 3D dynamic video.
2014 For an experimental validation of using Grassmann manifold, the same GMH is also
2015 built on Stiefel manifold using the Frobenius norm distance, given in Eq. 3.9, as it will be
2016 seen in the experimental Section 5.5. Figure 5.3 plots the *GMH* feature vectors obtained
2017 for three different depth videos, where the green segment corresponds to the emotion of
2018 interest while the black *GMH* segments are obtained for other different emotions. The
2019 similar shape exhibited by the *GMH* descriptors in the three cases for the emotion of
2020 interest in the middle can be appreciated.

2021 **5.3.2 Structured output learning from sequential data**

2022 The principle idea behind early detection from sequential data is to find the correct
2023 classifier capable of providing a recognition decision from both partial and complete
2024 events. This should permit recognition of the emotion of interest while receiving the
2025 sequential data and also provide its initial and ending boundary. To this end, in this work,
2026 we adopted the Structured-Output SVM (SO-SVM) [63], motivated by some interesting
2027 aspects of this classifier: 1) it can be trained on all partial segments and the complete one
2028 at the same time; 2) it allows us to model the correlation between the extracted features
2029 and duration of the emotion; 3) no previous knowledge is required about the structure of
2030 the emotion; 4) it can give better performance than other algorithms in sequence-based
2031 applications [99].

2032 Assume a set of *Geometric Motion History (GMH)* feature vectors are computed. Each
2033 resulted *GMH* feature vector includes an emotion of interest, which is annotated by a

5.3. EMOTION DETECTION FROM KINECT DEPTH-BODIES

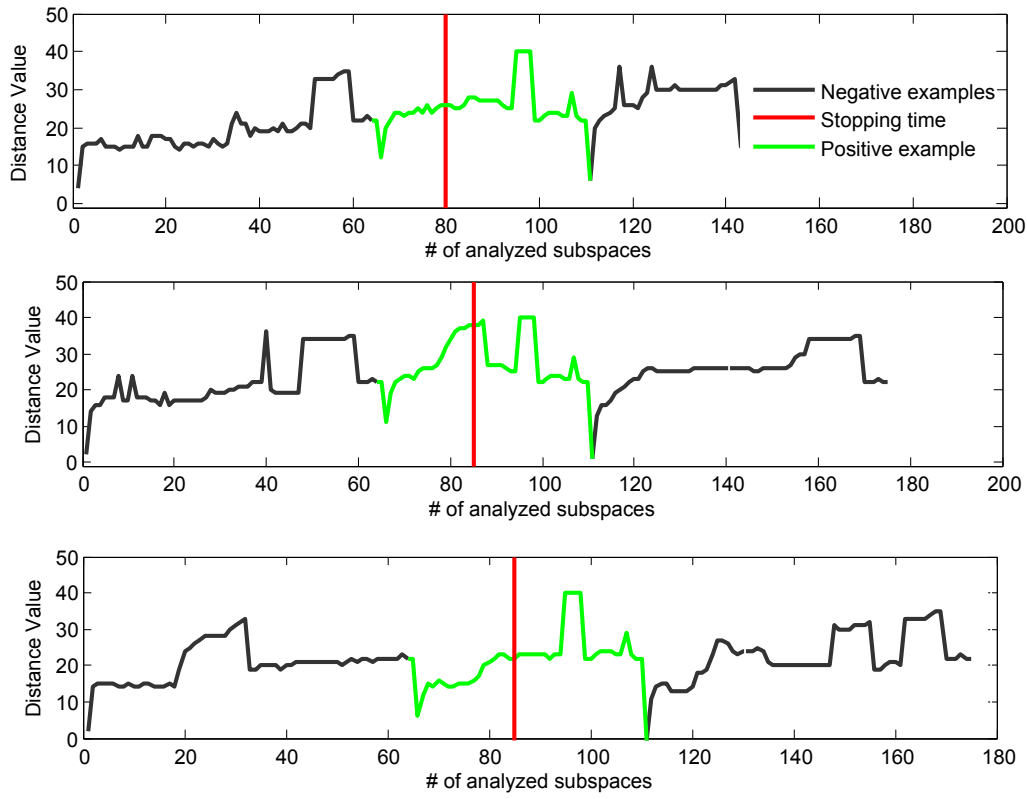


Figure 5.3: Three examples of the *Geometric Motion History* feature vectors extracted using the proposed framework.

2034 pair of values $\langle s^i, e^i \rangle$, representing the start and end time of the emotion, respectively.
 2035 At any time t^i comprised within the start and end of the emotion $s^i \leq t^i \leq e^i$, all partial
 2036 emotions sub-segments obtained between $[s^i, t^i]$ will be used to train the structured
 2037 output early event detector, since these different size sub-segments represent positive
 2038 samples. All the other parts of the *GMH* are considered, instead, as negative samples.
 2039 Another important aspect in SO-SVM early detection that always the more complete
 2040 emotion portion of the video has a higher functional score than the less complete one as
 2041 depicted in Fig. 5.4

2042 The expected performance from SO-SVM in the testing stage is to fire the detection
 2043 of the emotion of interest as soon as possible (after it starts and before it ends). As an
 2044 example, Fig. 5.3 shows (in red) the detection times at which the early detection of the
 2045 emotion from depth video is performed online. The problem of size variation between
 2046 the partial segments of the emotion and the complete one is solved by computing the

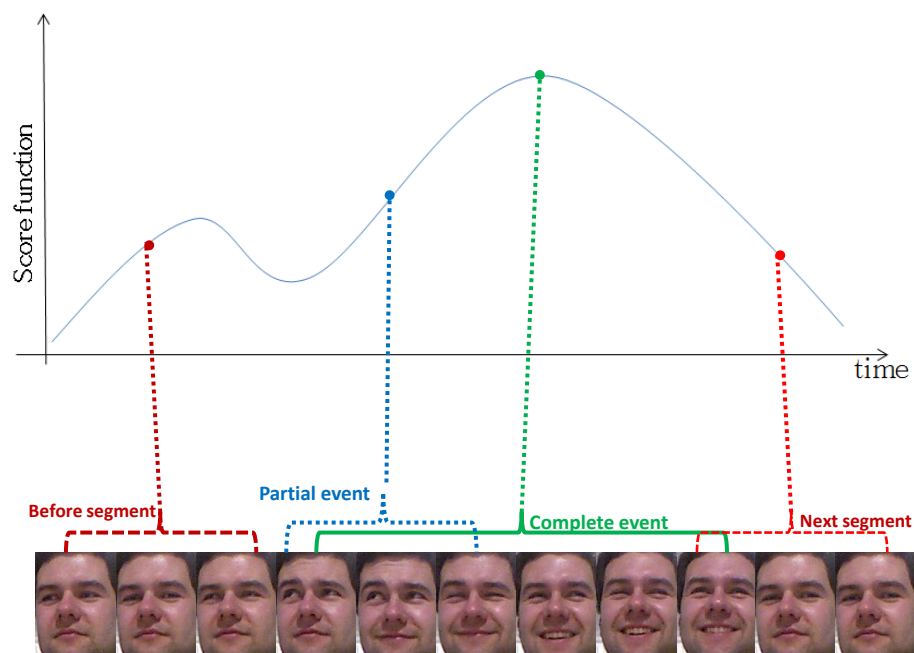


Figure 5.4: Online early detection score for happiness emotion from dynamic data

2047 L_2 -normalized histogram for each *GMH* segment to pass it to the SO-SVM. More details
 2048 about this SO-learning framework can be found in [63]. The task of emotion detection is
 2049 formulated as an early detection problem, which aims to detect the emotion of interest as
 2050 quick as possible. This is achieved using SO-SVM, which results in a convex optimization
 2051 problem [130].

2052 Algorithm 6 summarizes the steps of our proposed method for early emotion detection
 2053 from depth bodies.

2054 5.4 Physical pain detection from 4D-faces

2055 In this Section, we present a different adaptation of our trajectory based framework to
 2056 the scenario of spontaneous physical pain detection from high-resolution 4D scans. Two
 2057 different representations of the facial data are used here. First, the 3D landmarks-based
 2058 method that uses the 3D facial keypoints available in the video (as a baseline), and
 2059 the depth frames obtained from the 3D high-resolution scan. Since the detection of
 2060 physical pain from the face is related to slight and local facial expressions, we proposed
 2061 to create the Geometric Motion History (GMH) of the 3D video not only by geodesic
 2062 distance but by using the complete information available in the velocity vector between

Algorithm 6 – Online emotion detection from 4D depth-bodies

Require: Depth bodies videos set $\mathbb{S} = \{S_{m_i}^i\}_{i=1}^M$, of size M ; every S^i has m_i frames; ω is the window size

Initialization:

for $i \leftarrow 1$ to M **do**

$\hat{S}^i \leftarrow S^i$ //Depth preprocessing and taking the region of interest

$X^i = \{X_1^i, X_2^i, \dots, X_N^i\} \leftarrow \hat{S}^i$ //Dividing video into N successive subsequences of size ω

$\mathcal{T}^i(t) \leftarrow kSVD\{X_t^i\}_{t=1}^N$ //Subspace representation of the subsequences as trajectory

$GMH^i(t) \leftarrow d_{Geo}(\mathcal{T}^i(t), \mathcal{T}^i(t + \delta))$ //GMH building by computing geodeisc distances between successive subsapces

end for

Processing:

$D\{i\} = [GMH_L \mid GMH_M \mid GMH_R]$ //GMH Concatenation with emotion of interest in the middle

$Label\{i\} = [s, e]$ //GMH_M start and end points indexes

Model = SO-SVM($D_{tr}, Label_{tr}$) //SO-SVM Training

$y^* = SO-SVM(D_{tst}, Model)$ //SO-SVM Testing

Ensure: $y^* = [s^*, e^*]$ //Emotion of interest detected boundaries

2063 two subspaces in the trajectory. To this end, we implemented the transported velocity
 2064 vector fields formulation presented in Sect. 3.5.3. By this implementation, we intend to
 2065 illustrate the utility of considering the information carried in velocity vectors to capture
 2066 densely the deformations. Figure 5.5 shows the landmarks and the depth image with
 2067 their corresponding 2D texture image that belong to one 3D pain face, taken from the
 2068 BP4D-Spontaneous expression dataset.

2069 **5.4.1 3D landmarks-based Grassmann trajectories**

2070 In this solution, we start from a sequence of high-resolution 3D face scans, each of which
 2071 is labeled with l facial landmarks. The 3D coordinates (x, y, z) of the facial landmarks are
 2072 considered as a simple baseline descriptor of the face so that each frame is represented
 2073 by a vector in $\mathbb{R}^{3 \times l}$. Starting from this representation, and following the same steps of
 2074 Sect. 5.3 as dividing the video into subsequences of size ω , applying k-SVD to obtain
 2075 a trajectory of subspaces for every 3D dynamic pain sequence $\mathcal{T}(t)$ on a Grassmann
 2076 manifold $\mathcal{G}_k(\mathbb{R}^{3 \times l})$. The 3D spatio-temporal information is then captured by computing

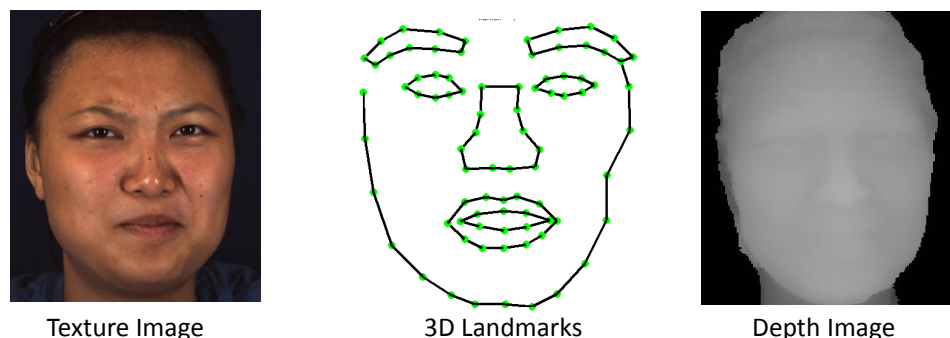


Figure 5.5: From left to right: color image; 3D landmarks; and depth image.

2077 the geodesic distance between successive subspaces by step δ to build the *Geometric*
 2078 *Motion History* from dynamic 3D landmarks.

2079 In addition, the change in the instantaneous speed along a trajectory due to both
 2080 facial deformations between two subspaces of the trajectory with interval δ and the
 2081 pose variations can be observed. This latter effect is the dominant one in Fig. 5.6, due
 2082 to a strong pose variation. This represents a problem for emotion recognition from the
 2083 facial deformation that is addressed by pose normalization as it will be detailed in the
 2084 experimental part.

2085 From this one-dimensional vector derived from 4D high-resolution facial data using
 2086 $\delta = 1, 3, 6$ can be observed. The importance of selecting an appropriate value of δ emerges
 2087 clearly from the Figure. It is evident that the signal resulting for $\delta = 1$ is noisy while the
 2088 informative change in the subsequence is clearer for $\delta = 3$. Further increasing δ to 6 can
 2089 cancel information about the emotional evolution through the video.

2090 This solution uses local and sparse information of the 3D shape of the face, and will
 2091 serve as a baseline to compare with the dense 3D shape representation using depth
 2092 images.

2093 5.4.2 Depth-based Grassmann trajectories

2094 In this case, we produce a depth image from each 3D model after preprocessing and
 2095 cropping the facial area. As mentioned earlier, a depth map gives a complete shape
 2096 description of the face, rather than only the 3D landmarks. Following the same procedure
 2097 as previously, every subsequence of ω depth frames is modeled as a k -dimensional
 2098 subspace of \mathbb{R}^n , being n the image size after vectorization. This permits us to build
 2099 a time-parametrized trajectory $\mathcal{T}(t)$ of subspaces on the Grassmann manifold $\mathcal{G}_k(\mathbb{R}^n)$,

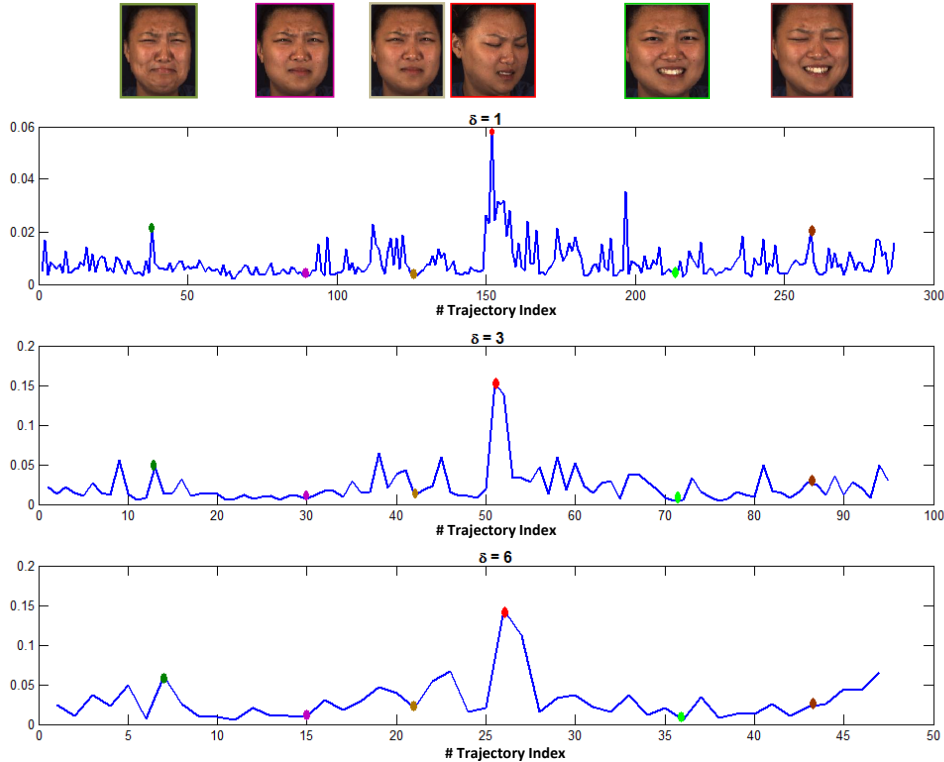


Figure 5.6: The instantaneous speed along a trajectory on Grassmannian manifold computed for a pain depth flow for different values of $\delta = 1, 3, 6$.

2100 similarly to the case studied in Sect. 5.3. In this scenario, in addition to build the *GMH*
 2101 by computing the geodesic distances between successive subspaces, like in the landmarks
 2102 representation method, we introduce a more efficient spatio-temporal representation of
 2103 the facial dynamic data by proposing the *Local Deformation Histogram (LDH)* descriptor
 2104 that follows the transported vector field formulation.

2105 More in detail, the *LDH* is computed through the following steps. First, the velocity
 2106 vector V between successive subspaces of a trajectory \mathcal{T} on the Grassmann manifold
 2107 $\mathcal{G}_k(\mathbb{R}^n)$ is computed and transported to a fixed tangent space $T_I(\mathcal{G}_k(\mathbb{R}^n))$ at the identity
 2108 element of Grassmann manifold. One possible representation of the parallel transported
 2109 velocity vector $(V_i) \in T_I(\mathcal{G}_k(\mathbb{R}^n))$ is a matrix of size $n \times k$. Taking the k first columns of this
 2110 matrix V_i as vectors of size n and reshaping them to the original dimension of the face
 2111 depth image $\hat{m} \times \hat{n}$ gives rise to a k -first components. Visualizing these components as
 2112 2D images shows clearly the temporal deformation with respect to its spatial location in
 2113 the depth image. The first component of the velocity vector contains informative motion
 2114 data, where the rest contains noise and redundant data.

2115 Then, rather than using the Grassmann distance that quantifies the speed along the
 2116 trajectory, we propose to exploit the first component of the velocity vector between two
 2117 subspaces. This new representation for the temporal evolution of the trajectory carries
 2118 information not only about the speed of the deformation, but also about where and in
 2119 which direction the deformation occurs as anticipated in Fig. 5.7.

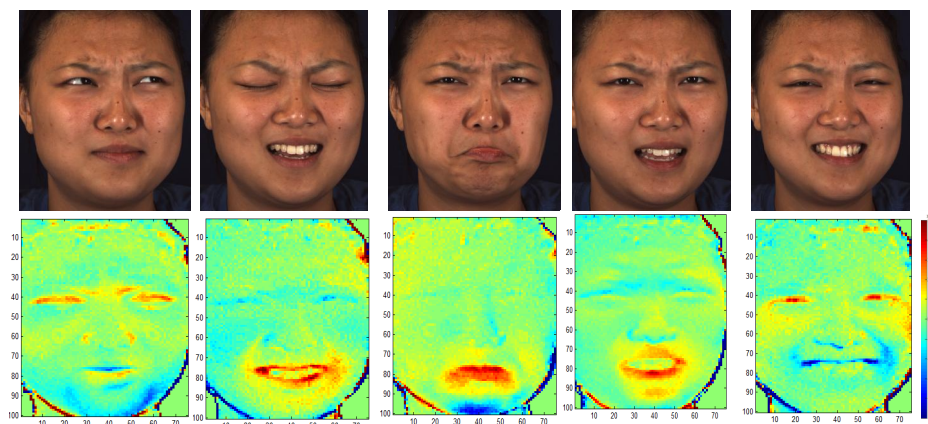


Figure 5.7: The visualization of velocity vectors first components between subspaces of one trajectory with their corresponding 2D texture images. The color maps show where the deformation happens in the face and its direction. Colors around green mean no deformation; from green to red: deformation in the positive z axis direction and from green to blue deformation in the negative z direction. The degree of the color indicates the deformation intensity.

2120 This is illustrated in Fig. 5.7, where positive values indicate a deformation in the
 2121 forward (positive z axis) direction, while negative values indicate deformation in the
 2122 backward (negative z axis) direction. The scalar value also indicates the degree of
 2123 deformation.

2124 In a final step, the matrix is divided into blocks, thus permitting us to localize
 2125 where the deformation happens in the face, and compute a dual value (positive/negative)
 2126 histogram for each block. This dual-value histogram gives us an idea about the intensity
 2127 and the direction of the deformation of the facial area associated with the block. Then,
 2128 the concatenation of all blocks provides what we call the *Local Deformation Histogram*
 2129 (LDH) for the velocity vector. The LDH vectors between each two successive subspaces
 2130 will be concatenated sequentially to build the Geometric Motion History *GMH* out of the
 2131 trajectory \mathcal{T} on Grassmann manifold. Fig. 5.8 illustrates these steps.

2132 The beginning and the end of the pain are decided according to certain annotated

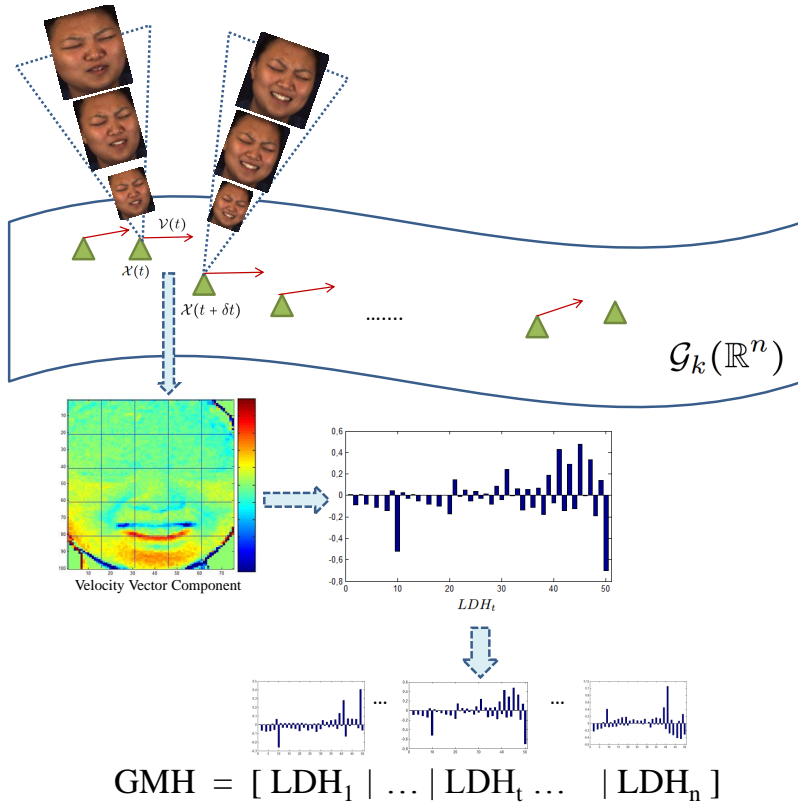


Figure 5.8: Illustration of LDH computation from the velocity vectors (red arrows) between subspaces (green triangles) of the same trajectory. Taking the first component of the velocity vector, and dividing the first component into 5×5 blocks, computing the dual value histogram for every batch and concatenate them together to have the LDH_t . Concatenating LDH for a ω frames gives rise the GMH feature vector, input of the SO-SVM algorithm.

2133 facial action units combination (this aspect will be discussed in more detail in Sect. 5.5).
 2134 The SO-SVM approach presented above will be used to detect the pain feeling as early as
 2135 possible from the GMH features extracted from the landmarks and depth representation.
 2136 Algorithm 7 summarizes the main steps of the pain detection approach from 4D high-
 2137 resolution data using the local deformation histogram (LDH).

2138 5.5 Experiments and evaluation

2139 To validate the proposed framework, we have conducted several experiments of emotion
 2140 detection on two different datasets. The first dataset captures depth-videos of the upper

Algorithm 7 – Physical pain detection from 4D-faces

Require: 4D facial scans set $\mathbb{S} = \{S_{m_i}^i\}_{i=1}^M$, of size M ; every S^i has m_i frames; ω is the window size. $Labels\{L^i\}_{i=1}^M$, where $L^i[s, e]$ indicates the start and the end of pain affect in S^i

Initialization:

for $i \leftarrow 1$ to M **do**

$\hat{S}^i \leftarrow S^i$ // 3D preprocessing and depth generation

$X_i\{\mathcal{X}_1^i, \mathcal{X}_2^i, \dots, \mathcal{X}_N^i\} \leftarrow \hat{S}^i$ // Dividing video into subsequences

$\mathcal{T}_i\{1, \dots, N\} \leftarrow kSVD(X_i\{1, \dots, N\})$ // Trajectory building

$\mathcal{V}_i \leftarrow Velocity(\mathcal{T}_i)$ // Velocity Vectors between subspaces

$\mathcal{V}_i^T \leftarrow Transport(\mathcal{V}_i)$ // Transportation to one tangent space

$LDH_i\{1, \dots, N\} = LDH(\mathcal{V}_i^T)$ // LDH from velocity vectors

$GMH_i \leftarrow [LDH_i(1), LDH_i(2), \dots, LDH_i(N)]$ // GMH building by concatenation of LDHs

end for

Processing:

Model = SOSVM(GMH_{tr} , $Labels_{tr}$) // SO-SVM Training

$y^* = SO-SVM(GMH_{tst}, Model)$ // SO-SVM Testing

Ensure: $y^* = [s^*, e^*]$ // Pain affect detected boundaries

2141 part of the body when spontaneous emotions or complex mental states, such as happiness
 2142 and thinking are exhibited [90]. We will apply our framework on this dataset to obtain
 2143 early detection of a spontaneous emotional state of interest. The second dataset consists
 2144 of high-resolution 3D videos of faces also showing spontaneous emotions, like happiness,
 2145 sadness, physical pain, etc. [152]. On this database, our experiments focus on early
 2146 detection of spontaneous physical pain using different representations.

2147 Two evaluation criteria are used to test the performance from the viewpoint of
 2148 accuracy and timeliness.

2149 • **Area under the ROC curve:** A ROC curve is created by plotting the *True Positive*
 2150 *Rate* (TPR) vs. the *False Positive Rate* (FPR) at varying threshold; and the Area
 2151 Under ROC Curve (AUC) gives the overall performance of the binary classifier to
 2152 discriminate between positive and negative samples;

• **AMOC curve:** The *Activity Monitoring Operating Characteristic* curve is generally used to evaluate the timeliness of any event surveillance system. It gives an indicator of how fast the detection of the event is, by reporting the *Normalized*

Time to Detection (NTtoD) as a function of False Positive Rate (FPR). In particular, NTtoD is defined as the fraction of the event occurred at one-time instance. For an event starting at s and ending at e in a time series, if the detector fires the event at time t where $s < t < e$, the NTtoD is given by:

$$(5.1) \quad NTtoD = \frac{t - s + 1}{e - s + 1}.$$

2153 5.5.1 Cam3D Kinect database

2154 In the Cam3D Kinect database [90], Mahmoud et al. collected a set of 108 audio/video
 2155 segments of natural complex mental states of 7 subjects. Each video is acquired with
 2156 the Kinect camera, including both the appearance (RGB) and depth (D) information.
 2157 The data capture natural facial expressions and the accompanying hand gestures. The
 2158 emotional states are: *Agreeing, Bored, Disagreeing, Disgusted, Excite, Happy, Interested,*
 2159 *Sad, Surprised, Thinking* and *Unsure*. These emotional states are more realistic and
 2160 more complex than the basic well known six facial expressions that are commonly used
 2161 in the literature. Figure 5.9 shows example frames for four different emotional states. It
 2162 can be observed the subjects sit at a table in front of the camera showing the upper part
 2163 of the body, including arms and hands, shoulders and face.

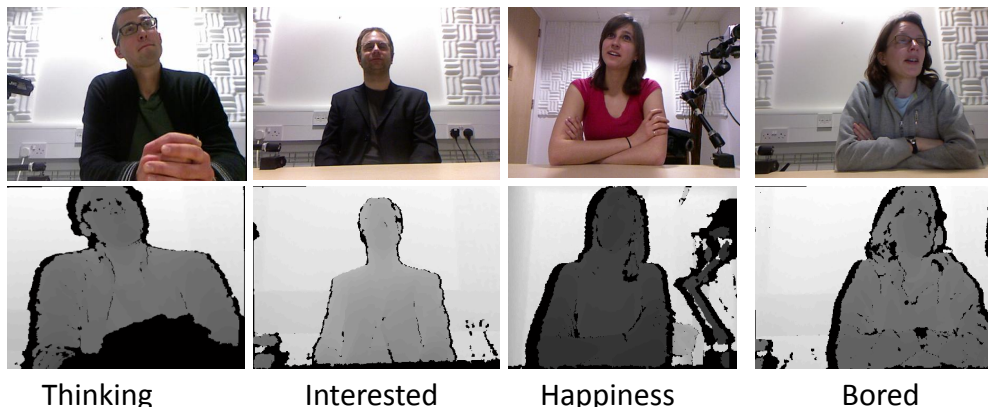


Figure 5.9: Cam3D Kinect database: Example depth frames with their corresponding 2D texture image of different emotional states.

2164 Table 5.1 shows the number of available segments for each emotional state. It can be
 2165 observed that videos in this dataset provide a sampling of the dimensional description
 2166 chart of emotions as reported in Fig. 5.1. However, the possibility to use each emotion
 2167 category in a detection experiment is hindered by the low number of videos comprised
 2168 by several categories (i.e., less than 8 videos are present in 9 out of the 12 emotion

2169 categories, with 5 categories having just 1 or 2 videos). This motivated us to consider
 2170 the following two experimental scenarios: *Happiness* vs. *others*; and *Thinking/Unsure*
 2171 vs. *others*. Compared to the chart of Fig. 5.1, the first scenario tests the detection of an
 2172 emotion of interest located in the *high-arousal / pleasure* quadrant (positive emotion);
 2173 the second one refers to an emotion in the *low-arousal / displeasure* sector (negative
 2174 emotion).

Table 5.1: Number of available depth videos for each emotional state

Emotional/Mental State	# of depth videos
Agreeing	4
Bored	3
Disagreeing	2
Disgusted	1
Excited	1
Happy	26
Interested	7
Neutral	2
Sad	1
Surprised	5
Thinking	22
Unsure	32

2175 5.5.2 Emotional state detection

2176 We applied the method using speed along trajectories on the manifold (see Algorithm 6)
 2177 to detect emotional states from two different regions of the dimensional *Arousal-Valence*
 2178 emotion chart of Fig. 5.1: (1) *Happiness* out of all non-happiness, i.e., *Happiness* vs. *others*
 2179 (high-arousal/pleasure quadrant); (2) *Thinking/Unsure* vs. *others* (*low-arousal / displea-*
 2180 *sure* quadrant). In both the experiments, the videos of the emotion of interest and the
 2181 videos of the other emotions are divided equally into two halves, one used for training
 2182 and one for testing. Then, the *Geometric Motion History* feature (GMH) of each video is
 2183 computed by dividing the video into subsequences of size $\omega = 20$ and subspace dimension
 2184 $k = 5$. These setting have been chosen empirically. Then, the GMH of the emotion of
 2185 interest is concatenated with the GMH computed for two videos of different emotional
 2186 states. Selecting these videos randomly for each concatenation, permitted us to obtain

2187 more training and testing data. Some examples of this process are illustrated in Fig. 5.3.
 2188 Using this setting, we derive a total of 100 GMH for training and the same number
 2189 for testing. For each generated sequence, the start and the end point of the emotion
 2190 of interest are known. Experiments in the following explore different aspects of the
 2191 proposed approach.

2192 In a first experiment, we compare the performance of our trajectory sequential
 2193 analysis framework using the *Geometric Motion History* feature computed for Grassmann
 2194 and Stiefel manifold. For the *Happiness vs. others* case, Fig. 5.10 shows the ROC and
 2195 the AMOC curves obtained. From the ROC curves related to the Grassmann, it can
 2196 be observed that when the FPR is around 20% the TPR reaches 90% for *Happiness*
 2197 detection. This accuracy decreases significantly (around 50%) at FAR=10%. Comparing
 2198 the analysis of the trajectories along the Stiefel (dashed curves) and the Grassmann
 2199 manifold (continuous curves), it clearly emerges the sequential analysis performed on
 2200 Grassmann manifold outperforms the analysis on Stiefel manifold. The areas under ROC
 2201 curves are 0.73 and 0.84 on Stiefel and Grassmann, respectively. The same findings can
 2202 be concluded from comparing Stiefel and Grassmann manifolds for *Thinking/Unsure*
 2203 emotional state in Fig. 5.10.

2204 This demonstrates the consistency of the subspace based representation $\mathcal{Y} = \text{Span}(Y)$
 2205 and the associated metric $d_{\mathcal{G}}$ over the matrix representation. This is mainly due to the
 2206 invariance of the subspace representation to the rotations $O(k)$ as \mathcal{G} is a quotient space
 2207 of \mathcal{V} under the group action of $O(k)$. The plots on the right of Fig. 5.10 show the evolution
 2208 of the system latency (the fraction of video needed to make the binary decision) against
 2209 FPR. For example, the detector achieves 20% of FPR by analyzing 20% of the video
 2210 segment. Also, in this case, results reported for the Grassmann representation are better
 2211 than results obtained from the Stiefel representation.

2212 From Fig. 5.10, it is also possible to compare detection accuracy results for *Hap-*
 2213 *piness* and *Thinking/Unsure*. In particular, the *Thinking/Unsure* detection shows a
 2214 performance decrease with respect to the *Happiness* detection results. The area under
 2215 the ROC curve is 0.66 and 0.79 on Stiefel and Grassmann manifold, respectively, for
 2216 *Thinking/Unsure*, while they are 0.73 and 0.84 for *Happiness*. These results confirm the
 2217 advantage in using the Grassmann rather than the Stiefel representation. From the plot
 2218 on the right of this Figure, it can be noted that about 20% of the negative samples are
 2219 recognized to be an element of this class, even if the videos are observed completely. This
 2220 can be motivated by the "common" neutral behavior exhibited by human when conveying
 2221 other complex mental states (e.g., agreeing, bored, etc.). This induces a confusion to the

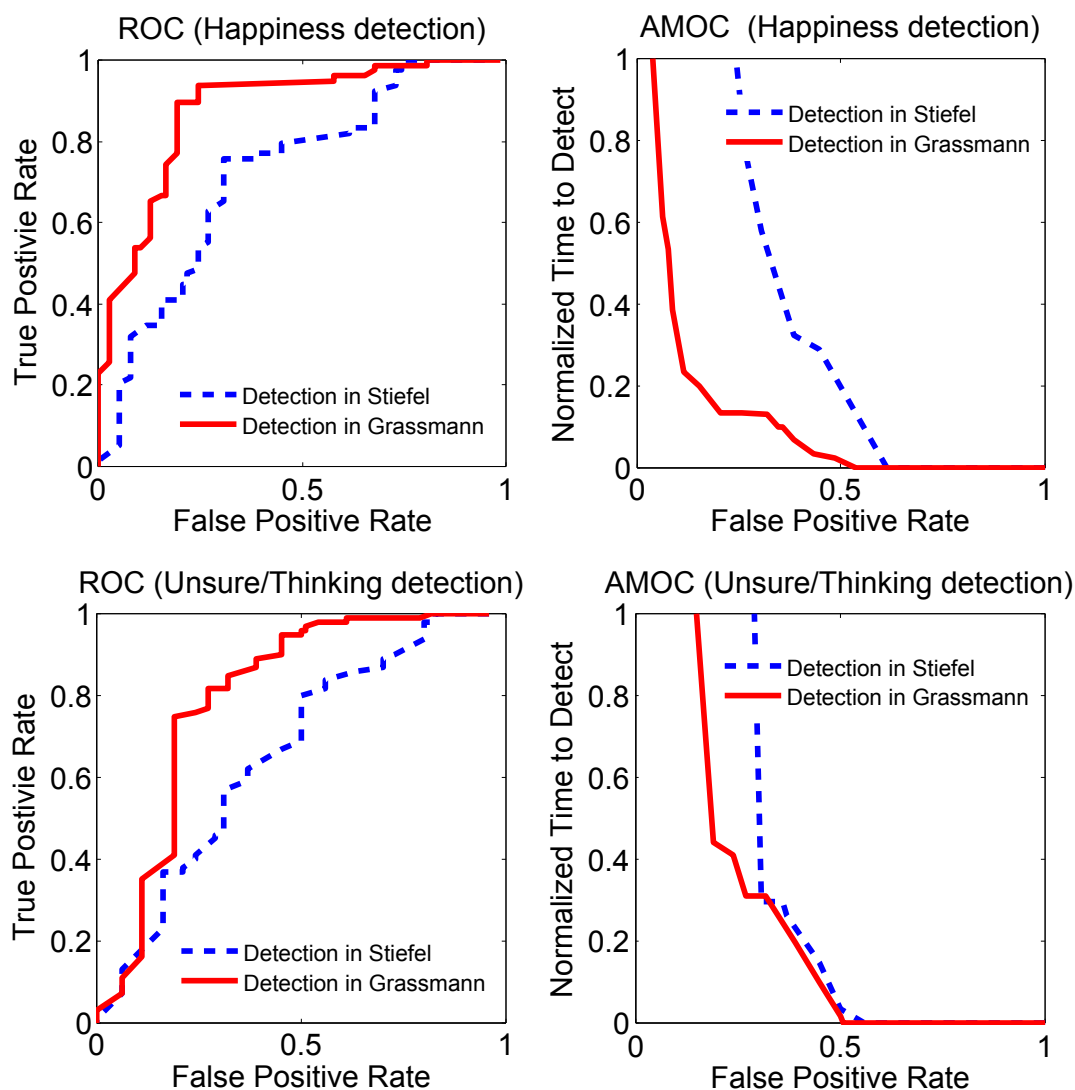


Figure 5.10: ROC and AMOC curves for *Happiness* (top) detection and *Thinking/Unsure* detection over Stiefel and Grassmann manifolds.

2222 detector, which was not the case for the *Happiness* detector, as the happiness is often
 2223 accompanied by body and facial expressions.

2224 To investigate the importance of using the upper part of the body versus using only
 2225 the face depth spatio-temporal information, we performed experiments with the previous
 2226 protocol, but considering the upper body in the depth videos to construct the *GMH* on
 2227 Grassmann manifold, instead of the cropped region of the face. From Fig. 5.11, it is clear
 2228 that the emotional state exhibited by the upper part of the body is easier to detect than
 2229 considering the facial region alone when acquired using cost-effective cameras. In the

2230 *Happiness* experiment, the area under the ROC curve for the upper part of the body and
 2231 the face only are 0.84 and 0.68, respectively. Performing the same experiment for the
 2232 *Thinking/Unsure* case, the area under the ROC curve is 0.79 and 0.63 for the upper
 2233 part of the body and the face only, respectively. This result is in agreement with studies
 2234 like [94, 135], which encourage the use of the upper body with the face to have better
 2235 performance in automatic emotional state understanding.

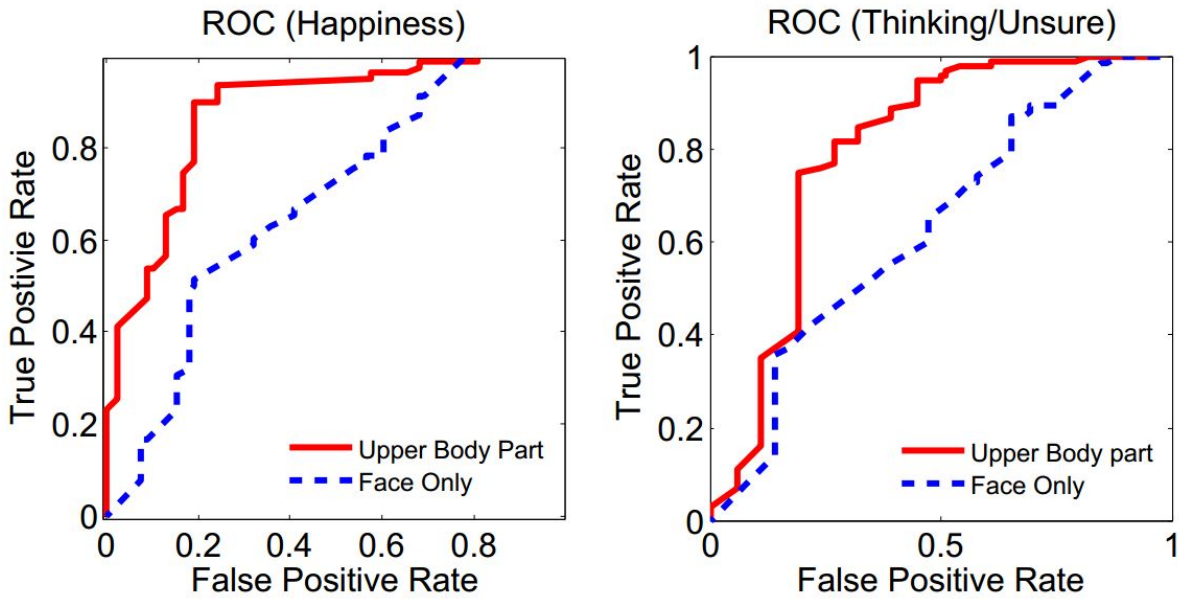


Figure 5.11: ROC curves comparison for *Happiness* and *Thinking/Unsure* detection over the Grassmann manifold using the upper body and the face only.

2236 Finally, we also investigated the relevance of the window size (# of frames used
 2237 to embody the motion in the subspace) and of the subspace dimension. In Fig. 5.12,
 2238 we consider the Grassmann manifold for *Happiness* detection and compare results for
 2239 windows of size $\omega = 20$ and $\omega = 5$ (red and blue curves, respectively). The dimension of
 2240 the subspace is $k = 5$ in both the cases (we remember here, k is the number of singular-
 2241 values used for the subspace representation). In the first case, with the window size of
 2242 $\omega = 20$, using five singular values permits us to keep 90% of the original information of
 2243 the temporal window (we selected this value by empirical experiment); in the second
 2244 case ($\omega = 5$), we keep 100% of the information as $k = \omega = 5$. So, in this comparison the
 2245 window size ω is the only changing parameter. The area under the ROC curve for $\omega = 5$
 2246 is 0.74, and 0.84 when $\omega = 20$. The observed performance gap between the two cases (a

2247 quite marked improvement is noted for $\omega = 20$), clearly evidences the importance of an
 2248 appropriate setting of these parameters.

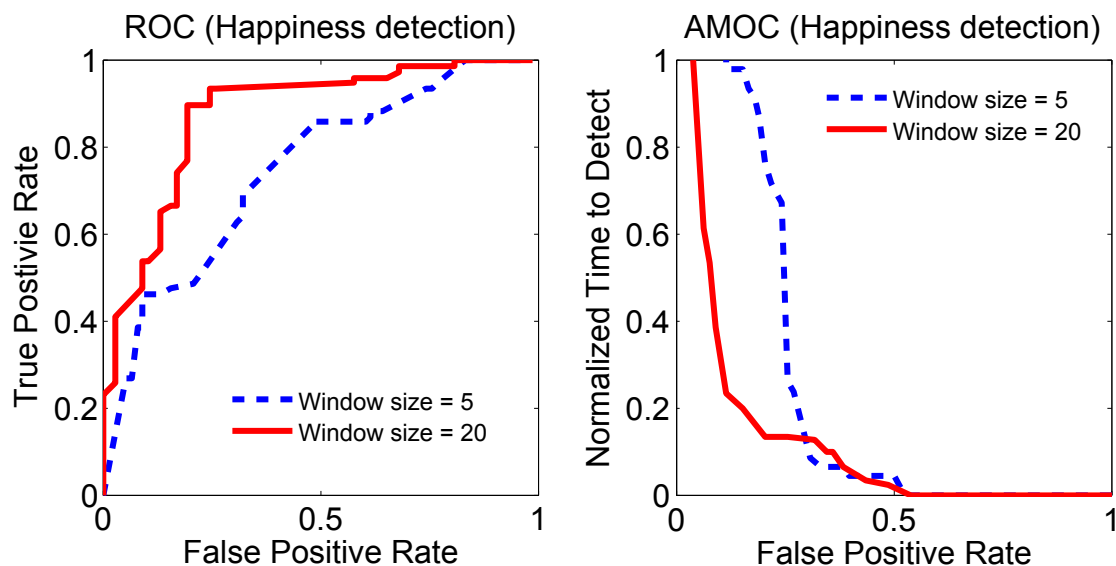


Figure 5.12: ROC and AMOC curves for *Happiness* detection over the Grassmann manifold for two different window size (i.e., $\omega = 5$ and $\omega = 20$).

2249 5.5.3 BP4D-Spontaneous facial expression database

2250 In [152], Zhang et al. proposed Binghamton-Pittsburgh 3D dynamic (4D) spontaneous
 2251 facial expression database. This database includes 41 subjects acquired using Di3D
 2252 dynamic face capturing system at 25 fps resolution for 3D videos. There are 8 different
 2253 tasks for every subject corresponding to the following spontaneous expressions: *Happi-*
 2254 *ness* or *Amusement*, *Sadness*, *Surprise*, *Embarrassment*, *Fear* or *Nervous*, *Physical pain*,
 2255 *Anger* or *upset* and *Disgust*. This database provides the 3D model and the 2D still images
 2256 for every video with metadata. The metadata includes for 2D texture images, the 46
 2257 landmarks annotation with the pose information, and for 3D models, 83 feature points
 2258 (landmarks) annotation with the pose information given by the *pitch*, *yaw* and *roll* angles.
 2259 Facial action units (FAUs) are provided for 20 seconds (about 500 frames) of every task.
 2260 This AU annotation provides information about the fact a specific AU is activated or not
 2261 in the frame and its intensity in the case of activation. Figure 5.13 depicts one 3D model
 2262 with its corresponding 2D texture image for every task.

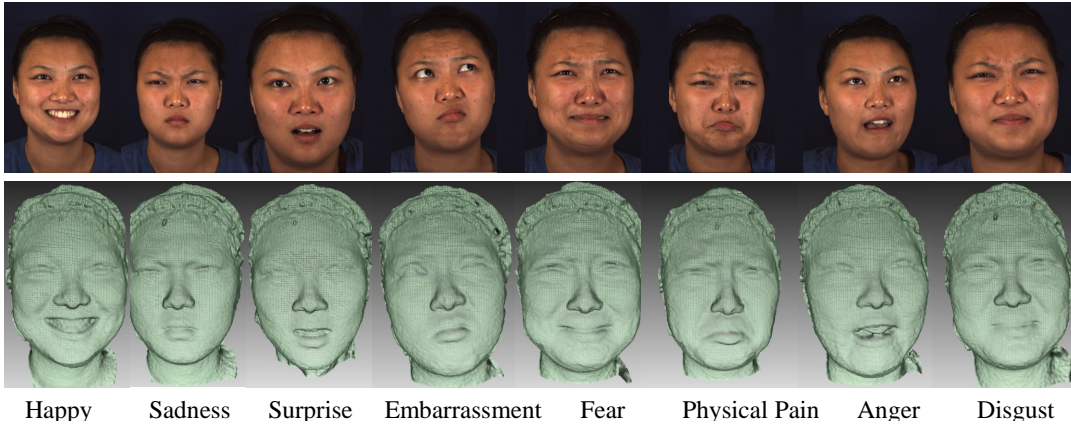


Figure 5.13: BP4D Database: Examples of the eight different spontaneous expressions (tasks) included in the database

2263 5.5.4 Analyzing 4D-faces for physical pain detection

We applied the proposed geometric framework with transported velocity vector fields method as explained in Sect. 5.4 to detect spontaneous physical pain from 3D dynamic facial videos. The spontaneous physical pain is elicited by putting the participant's hand in ice water for each of the 41 subjects. The acquired 3D videos are quite long (their duration is about 20s), and it is known there is a pain emotion through the video, which constitutes our initial ground truth. To have accurate pain affect start and end points during the video as an emotion of interest, we use the FAUs provided annotation. Several studies have been conducted in psychology field to reveal the optimal AUs combination that can define the physical pain emotional state, like [70] where they found the AUs that can be activated in pain affect are those listed in Table 5.2. Parkachin and Solomonin [70] also proposed a pain intensity scale equation (PSPI) considering certain AUs:

$$(5.2) \quad Pain = AU4 + (AU6||AU7) + (AU9||AU10) + AU43.$$

Zhang et al. [155] made extensive study to show the mapping between the AUs and the targeted emotion on BP4D database, and they found that AUs {4, 6, 7, 9, 10} are the most common in pain videos. From these results, and the available AUs annotation, we decided the begging and the end of the pain in the videos using the following equation:

$$(5.3) \quad Pain = AU4 + (AU6||AU7) + (AU9||AU10).$$

2264 which states that a *physical pain* is considered as existing if AU4 and (AU6 or AU7) and

Table 5.2: Possible AUs related to pain according to [70].

Action unit	Name	Action unit	Name
4	Brow Lowerer	20	Lip Stretcher
6	Cheek Raising	25	Lip parter
7	Eyelid Tightener	26	Jaw Dropper
9	Nose wrinkler	27	Mouth Stretcher
10	Upper Lip Raiser	43	Eye Closer
12	Lip Corner Puller		

2265 (AU9 or AU10) are activated. Figure 5.14 illustrates the use of AUs combination for pain
 2266 annotation according to Eq. (5.3).

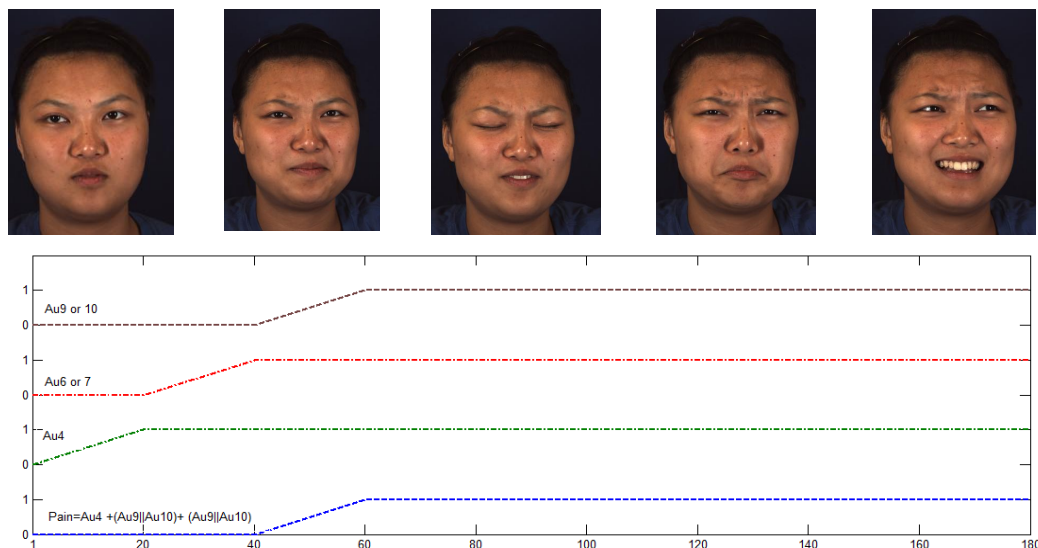


Figure 5.14: Illustration of AU activation during a physical pain video. The horizontal axis gives the frame index in the video, and the vertical axis provides the activation (i.e. of value 1) or non-activation of the AU (i.e. of value 0).

2267 Based on the available AUs annotation in BP4D database, 28 subjects have been
 2268 selected for the task of physical pain detection (task 6 videos). Half of these subjects
 2269 (14) are used for training and the second half (14) for testing in the SO-SVM learning

2270 framework with the beginning and the end of pain emotion labels. There is no need for
 2271 concatenation of *GMH* in these experiments since we have long 3D videos and the pain
 2272 does not start immediately according to the eliciting protocol. Two methods have been
 2273 investigated in this work to model the 3D video subsequences. Results, for both the cases,
 2274 are reported in the following, using a window size $\omega = 6$ for deriving the linear subspaces.

2275 **3D landmarks-based (baseline) method**

2276 In this representation, we use the 3D coordinates (x, y, z) of the 83 landmarks available
 2277 in BP4D metadata as a representative feature for every 3 frame after vectorizing these
 2278 values to have a feature vector in \mathbb{R}^n where $n = 83 * 3 = 249$. This approach is regarded
 2279 as a baseline solution for our work. We model every subsequence of size $\omega = 6$ as one
 2280 subspace after applying k -SVD, with $k = 2$. These settings are selected empirically. Two
 2281 experiments are conducted using this representation to study the pose effects and the
 2282 step δ on the trajectory.

2283 To evaluate the pose normalization effect on the performance, we used the landmarks
 2284 representation for pain detection from 3D videos with and without the pose normalization
 2285 in order to investigate how the pose variation affects the pain detection accuracy. The pose
 2286 is normalized by applying the inverse rotation of the 3D frame pose information given
 2287 in the metadata. From Fig. 5.15, it is quite clear that the AUC with pose normalization
 2288 (0.68,0.78,0.76) are higher than without pose normalization (0.63,0.75,0.70) for $\delta = 1, 3, 6$,
 2289 respectively. These results confirm the negative effect of pose variation in our framework,
 2290 because the facial deformation resulting from pain affect in correspondence to the
 2291 landmarks is combined with the changes resulting from the pose variation.

2292 *GMH* curves on Grassmann manifold can be affected by noisy changes that might
 2293 occur due to raw data or errors in the registration step. To investigate this aspect, we
 2294 considered the effect of different smoothing levels applied to the Grassmann trajectory,
 2295 which corresponds to using different values of δ . This empirical analysis is conducted
 2296 using the landmarks representation and normalized pose with $\omega = 6$ and $k = 2$. Table 5.3
 2297 shows the AUC values for pain detection with this setting for δ from 1 to 5. The best
 2298 AUC value of 0.78 is obtained for $\delta = 3$. These results show that smoothed trajectories,
 2299 corresponding to $\delta > 1$, provide better performance up to a certain extent, thanks to the
 2300 noise removal, but large values of δ (e.g., $\delta = \{4, 5\}$) affect negatively the results, since
 2301 informative changes along the time can be canceled.

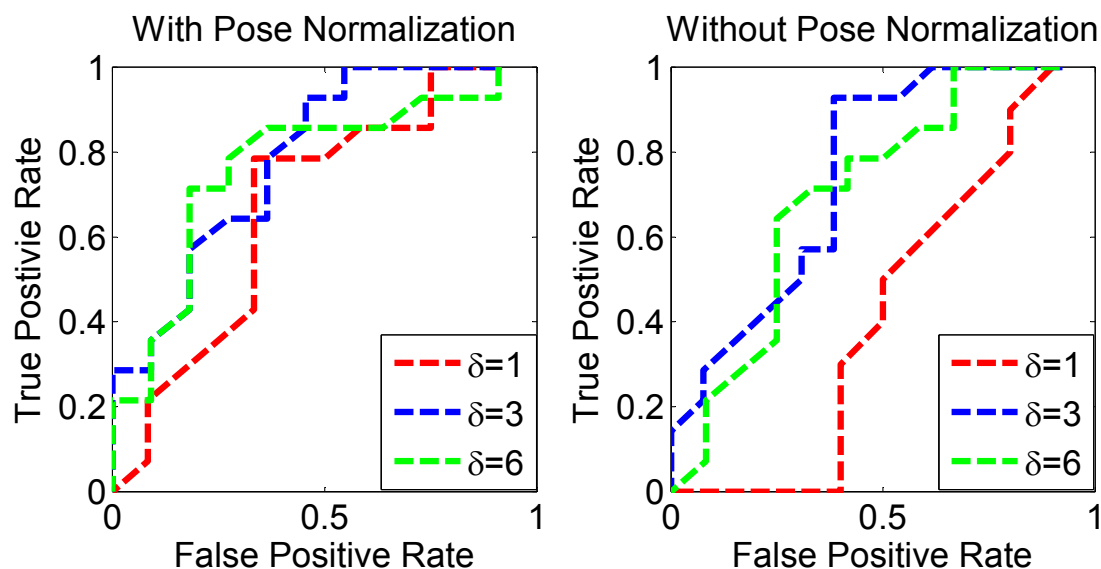


Figure 5.15: ROC curve for the landmarks method. The left plots show the ROC curves after pose normalization for $\delta = \{1, 3, 6\}$, while the right plots show the performance obtained without pose normalization.

Table 5.3: AUC values for the landmarks method, with and without pose normalization, for $\delta = 1, 2, 3, 4, 5$

value of δ	1	2	3	4	5
AUC – not normalized pose	0.63	0.69	0.75	0.71	0.70
AUC – normalized pose	0.68	0.72	0.78	0.75	0.74

2302 Depth representation method

2303 In this approach, the depth images of the face region are used instead of the landmarks.
 2304 The depth image is obtained by rendering the 3D model after pose normalization, and
 2305 then the face region is cropped and saved as a depth image of size 100×75 . The pain
 2306 depth video is divided into subsequences of size $\omega = 6$, and every subsequence is modeled
 2307 as one subspace by applying k -SVD, with $k = 2$ and $\delta = 3$.

2308 Firstly, we compare the performance of the proposed pain detection framework
 2309 by using two different facial representations: the landmarks, and the depth data of
 2310 the face region. In both the cases, the geodesic distance is used to create the *GMH*
 2311 trajectories, with $\omega = 6$ and $k = 2$ under normalized pose. Figure 5.16 shows the ROC

2312 and AMOC curves for the two methods. From the ROC curve, we observe the depth
 2313 representation, whose captures carry more spatio-temporal information, also achieves
 2314 better performance on pain affect detection. The AUC value obtained using depth flow
 2315 reached 0.80, compared to the value of 0.78 obtained using the landmarks only. In term
 2316 of timeliness represented by AMOC curve, we can see that the depth flow scores less
 2317 false positive rate once the system receives more than 50% of the pain emotion frames.

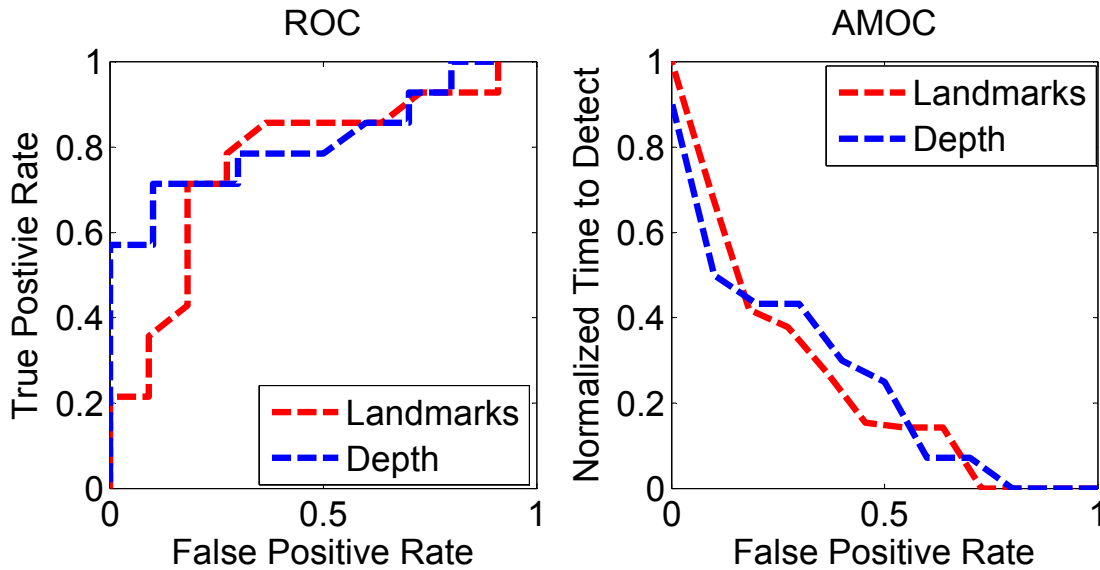


Figure 5.16: ROC and AMOC curves for comparison between pain detection using landmarks and depth representation.

2318 The performance of the GMH computed from the geodesic distances is then evalu-
 2319 ated in comparison with our proposed Local Deformation Histogram (LDH) descriptor
 2320 extracted from the whole velocity vector between two successive subspaces along the
 2321 trajectory (see Sect. 5.4). In both the cases, we used pose normalization with $\omega = 6$,
 2322 $k = 2$, and $\delta = 3$. Results for this experiment are reported in Fig. 5.17, showing the ROC
 2323 and AMOC curves for the two methods. The ROC curve on the left shows the superior
 2324 performance of the LDH representation over the geodesic distance, where the AUC for
 2325 LDH and geodesic distance is 0.84 and 0.80, respectively. The AMOC curve on the right
 2326 shows that the two methods are comparable, while the system receives less than 40%
 2327 of the pain emotion, and the LDH method achieves less false positive rate when more
 2328 frames are received.

2329 These results confirm the efficiency of using local coding of the temporal facial
 2330 deformation through the time for pain affect detection from facial expressions. This

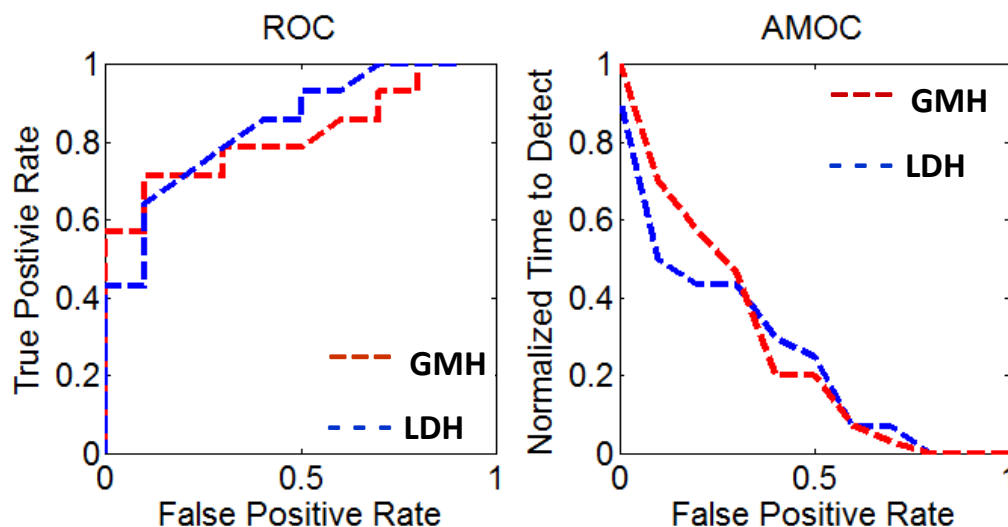


Figure 5.17: ROC and AMOC curves for comparison between pain detection using *Local Deformation Histogram (LDH)* and Grassmann distances-based *GMH*.

2331 representation outperforms the geodesic distance method, which accounts only for the
 2332 speed of the deformation through the time, thus incurring in potential hiding of important
 2333 local cues for detection.

2334 5.6 Conclusion

2335 In this chapter, we have introduced a novel geometric framework for early detection
 2336 of spontaneous emotional states, and experimented its applicability in two different
 2337 scenarios: (i) happiness/thinking-unsure detection in depth videos of the upper part of the
 2338 body acquired using Kinect-like cameras (depth-bodies); and (ii) physical pain detection
 2339 from 3D high-resolution facial sequences (4D-faces). The key idea of our approach is to
 2340 represent the stream of depth-images as time-parametrized trajectories of subspaces on
 2341 a well defined Grassmann manifold. Analyzing the obtained trajectories gives rise to
 2342 space-time features called *GMH (Geometric Motion History)* computed in two different
 2343 ways to allow global and local analyze of the deformations and their temporal rhythm
 2344 along the underlying trajectories. From a perspective of binary classification, we use an
 2345 adaptation of the SVM algorithm to accommodate sequential (partial) analysis of the
 2346 features, proposed earlier in [63]. We have experimentally illustrated the effectiveness of
 2347 the proposed framework using two datasets: the Cam3D contains spontaneous emotions
 2348 and complex mental states, such as happiness and thinking/unsure, while the BP4D

2349 consists of high-resolution 3D facial sequences of a set of eight emotional states, including
2350 the physical pain affect. We have performed several experiments including (i) global vs.
2351 local GMH (using LDH) representations, (ii) sparse (3D landmarks) vs. dense (depth)
2352 data, (iii) Stiefel vs. Grassmann (quotient space of the Stiefel), and (iv) the impact of
2353 the pose variation on the obtained results. To our knowledge, this is the first work
2354 proposing early automated detection of spontaneous emotions and pain acquired from
2355 high-resolution and low-resolution depth videos.

2356 We have limited our experiments to an existing early event detector [63] from se-
2357 quential Euclidean features in order to exemplify the proposed representation. It will be
2358 interesting to investigate advanced statistical inference techniques of partial (or full)
2359 observations using intrinsic (on the manifold) or extrinsic (e.g., fixed tangent space). In
2360 addition, we will apply the same framework to other databases and emotions to make
2361 more detailed comparison with other detection approaches.

CONCLUSION AND PERSPECTIVES

2362 **Summary and contributions**

2363 We have demonstrated, through the study investigated in this thesis, the contribu-
2364 tion of 3D facial dynamic behavior in identity recognition and spontaneous emotion
2365 early detection. We have proposed a unified framework based on (optimized) subspace
2366 representations, which leads to the Grassmann manifolds. When the subspace-based
2367 representation is widely used in 2D domain and several computer vision research areas
2368 such as face recognition [134], action recognition [138], facial expression recognition
2369 [1] and age estimation [48]. To our knowledge, our study is the first one bringing these
2370 ideas, with extensions, to 3D dynamic domain. For each targeted application, we have
2371 derived a specific representation and efficient classification/detection algorithms. That
2372 is, in the context of face recognition, we have used the sparse coding and dictionary
2373 learning techniques on Grassmannian to design an efficient solution. We have demon-
2374 strated experimentally that considering the temporal evolution (up to certain interval)
2375 of the face helps to recognize people both in expression-dependent (same expression)
2376 and expression-independent (different expression) scenarios. A comparative study of
2377 the proposed solution to the existing method of Sun et al. [128] and two baseline algo-
2378 rithms, GNNC for Grassmann Nearest-Neighbor Classifier and an improved variant
2379 of the Grassmann Discriminant Analysis (GGDA) has shown the effectiveness of the
2380 proposed solution. In fact, our approach does not need neither landmarks detection nor
2381 tracking densely the vertex-flow over the 3D video. Extensive experiments (on the pub-

2382 licly available dataset BU-4DFE) are conducted but remains limited due to the limited
2383 number of subjects. Initially, this database is designed to test solutions on 4D (posed)
2384 facial expression analysis, where the participants are asked to sit in front of the camera
2385 and pose specific expression. Hence, all the 3D frames are near-frontal and of spatial
2386 and temporal high-resolutions.

2387 To allow more realistic face recognition tests from 3D video, we have collected a new
2388 dataset, which includes several sequences of 58 participants, using a single-view 3D
2389 scanner with a large field-of-view to allow people (more than one in some scenarios)
2390 moving freely (but up to certain distance) in front of the 3D camera. Preliminary results
2391 on this new challenging dataset are reported as well.

2392 As far as the second targeted application of early detection of spontaneous emotion
2393 is concerned, a novel (non-linear) representation of long 4D sequences is proposed. It
2394 consists to map the original 3D video data to Grassmann manifolds and build time-
2395 parametrized curves (or trajectories). Then, a simple dynamic model have been proposed
2396 based on the first-order derivation along the curves to capture the facial dynamic spatio-
2397 temporal behavior. Finally, we have employed and adapted recently-developed learning
2398 techniques for partial Euclidean data analysis. Using this pipeline, we have designed
2399 solutions for complex emotional state early detection. The validation has been made
2400 in two different scenarios. When the first uses depth-streams acquired via consumer
2401 cameras (like the Kinect) and focus on the behavior of the upper-part of the body, the
2402 second analyzes high-resolution 4D faces for the purpose of physical pain detection.
2403 These test scenarios are context-dependent, i.e., the emotional states and the physical
2404 pain are stimulated using the same procedure for all the participants of the databases,
2405 Cam3D [90] and BP4D-Spontaneous [152], respectively. Again, we consider these experi-
2406 ments limited due to the limited number of available acquisitions and participants. In
2407 contrast, the emotions exhibited in both datasets are spontaneous, which represents a
2408 first opportunities to researchers to conduct preliminary studies. Here also, an important
2409 set of experiments are conducted to compare the trajectory representation on Grassmann
2410 vs. Stiefel manifolds, the depth-based shape representation vs. the landmarks-based
2411 representations and to allow studying our approach's behavior when changing some
2412 relevant parameters.

2413 As mentioned above, my thesis presents preliminary methodological and practical
2414 contributions to the field of face analysis from 4D facial sequences with experimental
2415 illustrations in face recognition and emotion detection. However, it opens the door to
2416 several perspectives and future work that we summarize in the next section.

2417 **Perspectives and future directions**

2418 This work is one of the first studies in the field of 4D data analysis for human facial
2419 behavior understanding. It is now a shared conviction that the 3D data capture faithfully
2420 the facial deformations and allow better understanding of facial behavior, compared to
2421 2D data. Using dynamic 3D data (4D) is suitable as the face is a deformable surface
2422 by nature. This work confirms these observations in the context of identity recognition
2423 and emotion analysis. However, several issues of two types remain open – practical and
2424 methodological/theoretical.

2425 First, the availability of 3D sensors embarked on computers and tablets have pushed,
2426 recently, the community to explore the use of depth and color streams together or sepa-
2427 rately in human behavior analysis. In addition to their attractive cost, RGB-D cameras
2428 (and their associated SDKs) present several benefits. That is, the foreground (human
2429 body, face, hands, etc.) could be isolated easily from the background in the filmed scene.
2430 Second, in spite of its low-resolution and the presence of noise, the depth channel is an
2431 additional source of information which reflects a dense (dynamic) shape representation of
2432 the face or the body. However, analyzing the dynamic depth channel requires to address
2433 several issues such as the noise, incomplete data, occlusions, etc. In this work, we have
2434 presented possible solutions to these problems, mainly using the subspace represen-
2435 tation of short-time 3D clips. This representation could be improved by introducing
2436 some methodological approaches as we will describe next (i.e., smoothing and filtering
2437 Grassmann trajectories) and consider recent technical progress which makes available
2438 solutions for real-time pose estimation in depth videos. Considering these solutions, one
2439 can implement real-time processing algorithms, improve current performances and go
2440 to real-world like evaluation of the approaches. In this context and with the help of a
2441 master student (Damien Druel), I have started this work with the implementation of
2442 first blocks including – depth data acquisition using the Intel RealSense F200 camera.
2443 I use available algorithms in the SDK (face detection, landmarks detection and pose
2444 estimation), and include our implementation of the subspace-based representation. This
2445 gave rise to a preliminary interface to study the proposed methodology, in a realistic way
2446 and using depth-consumer cameras.

2447 From a methodological point-of-view, it is now a sharing statement that dense corre-
2448 spondence between 3D frames is required to accurately quantify the facial deformations
2449 and the temporal dynamics. Some research groups have tried to tackle this problem by
2450 developing vertex flow tracking algorithms and/or model adaptation techniques, under

2451 facial deformations. For example, in [15], Ben Amor et al. have proposed a Riemannian
2452 approach, which resolves the issues of pose variations and dense correspondence, in the
2453 same framework, using elastic radial curves. However, the registration is obtained along
2454 the curves, which presents a serious limitation of their approach. In a different way,
2455 Sun et al. [128] proposed to use a vertex tracking algorithm, driven by the location of
2456 3D landmarks along the 3D video. This method is time-consuming and unsuitable for
2457 real-time processing. Other solutions consist of using or adapting existing algorithms,
2458 previously used in static, like the Non-rigid Iterative Closest Point (ICP) [31], the Free
2459 Form Deformation (FFD) algorithm [49], or the Thin-plate Splines (TPS) technique
2460 [45] to achieve non-rigid registration or template fitting. Their goal is to achieve an
2461 accurate frame-to-frame correspondence. In our methodology, we consider short-time
2462 clips and assume pixel-to-pixel correspondence, in the same temporal interval (window).
2463 Long-term videos are presented by curves (of subspaces) on Grassmann manifolds. Al-
2464 though its capability to face both pose variation and dense correspondence issues, its
2465 major limitation is the limited size of the 3D clips. One possible future investigation is
2466 associating efficient 3D registration/tracking algorithms to subspace representations to
2467 allow increasing the time-interval of the clips (i.e. increase the window size) and study
2468 the behavior our the trajectory-based representation.

2469 Another interesting methodological perspective to propose a suite of tools and al-
2470 gorithms for processing trajectories on Grassmann manifolds. The simplicity of their
2471 geometry and the availability of geometric formulations and efficient implementations
2472 (of geodesics, Karcher mean computation, etc.) make possible to develop the following
2473 processing blocks,

- 2474 - **Smoothing and (median) filtering** of trajectories to allow reducing the effect of
2475 the noise, suitable when exploiting depth data. This is possible using algorithms to
2476 compute sample (Karcher) means and median samples on a fixed-time window of
2477 the trajectories.
- 2478 - **Resampling (down-sampling or up-sampling)** original trajectories based on
2479 the geodesic formulation on Grassmann manifolds. In some cases, processing/analyzing
2480 requires increasing their temporal resolution. This is possible by creating new
2481 samples between original samples (up-sampling processing). In contrast, the down-
2482 sampling step reduces the number of original samples on the trajectory.
- 2483 - **Novel dynamic models**, which consist in computing n -order derivations of the
2484 trajectories (the simplest ones are velocity and acceleration) to characterize their

2485 temporal evolution. In the proposed methodology, we have investigated only a
2486 first-order dynamic model, which leads to the velocity vector field. This model could
2487 be easily extended to a second-order model involving the covariant derivative of
2488 velocity vector fields, and so on.

2489 - **Extend existing inference models to analyze curves on Grassmann mani-**
2490 **folds** and their use in dynamic 3D data analysis. For example, it will be interesting
2491 to adopt techniques designed to analyze time-series to the Grassmann domains (or
2492 any other matrix manifold). Some recent works have studied the problem, in the
2493 context of object tracking, using particle filtering [55, 120].

2494 All these tools and others could be developed in the continuous domain, which
2495 is more suitable for theoreticians. That is, one can start considering continuous and
2496 smooth parametrized curves on Grassmann manifolds (i.e., $\mathcal{G}_k(\mathbb{R}^n)$) and to develop proper
2497 metrics, statistical summaries and associated algorithms for the space of trajectories (i.e.,
2498 $\mathcal{G}_k(\mathbb{R}^n)^{[0,t]}$). One difficult problem would be to propose rate-invariant metrics (or dynamic
2499 time-warping techniques) for registration and comparison of curves, which basically
2500 represent 4D sequences of the same emotion conveyed by different subjects, for example.
2501 Based on this methodology, one can push the discretization of the problem to the end
2502 step, i.e., when implementing the algorithms. All the ideas presented above, of both
2503 methodological and practical order, present the direction of our future investigations.

BIBLIOGRAPHY

- [1] Improving subspace learning for facial expression recognition using person dependent and geometrically enriched training sets.
Neural Networks, 24(8):814 – 823, 2011.
Artificial Neural Networks: Selected Papers from {ICANN} 2010.
- [2] A. F. Abate, M. Nappi, D. Riccio, and G. Sabatino.
2D and 3D face recognition: A survey.
Pattern Recognition Letters, 28(14):1885–1906, 2007.
- [3] M. Abd El Meguid and M. Levine.
Fully automated recognition of spontaneous facial expressions in videos using random forest classifiers.
Affective Computing, IEEE Transactions on, 5(2):141–154, April 2014.
- [4] P.-A. Absil, R. Mahony, and R. Sepulchre.
Optimization algorithms on matrix manifolds.
In *Princeton University Press, Princeton, NJ*, 2008.
- [5] T. Alashkar, B. Ben Amor, M. Daoudi, and S. Berretti.
A 3D dynamic database for unconstrained face recognition.
In *5th Int. Conf. of 3D body scanning technology*, Oct 2014.
- [6] T. Alashkar, B. Ben Amor, M. Daoudi, and S. Berretti.
A grassmannian framework for face recognition of 3D dynamic sequences with challenging conditions.
In *European Conf. on Computer Vision (ECCV) Workshops*, pages 326–340.
Springer International Publishing, 2014.
- [7] S. Aly, A. Trubanova, L. Abbott, S. White, and A. Youssef.
Vt-kfer: A kinect-based RGBD+time dataset for spontaneous and non-spontaneous facial expression recognition.

- In *Biometrics (ICB), 2015 International Conference on*, pages 90–97, May 2015.
- [8] B. Amberg, S. Romdhani, and T. Vetter.
Optimal step nonrigid ICP algorithms for surface registration.
In *Computer Vision and Pattern Recognition, 2007. CVPR '07. IEEE Conference on*, pages 1–8, June 2007.
- [9] R. Anirudh, P. Turaga, J. Su, and A. Srivastava.
Elastic functional coding of human actions: From vector-fields to latent variables.
June 2015.
- [10] M. Aung, S. Kaltwang, B. Romera-Paredes, B. Martinez, A. Singh, M. Cella, M. Valstar, H. Meng, A. Kemp, A. Elkins, N. Tyler, P. Watson, A. Williams, M. Pantic, and N. Berthouze.
The automatic detection of chronic pain-related expression: requirements, challenges and a multimodal dataset.
Affective Computing, IEEE Transactions on, 2015.
- [11] J. Barr, K. Bowyer, P. Flynn, and S. Biswas.
Face recognition from video: a review.
Int. Journal of Pattern Recognition and Artificial Intelligence, 26(5), 2012.
- [12] A. Battocchi, F. Pianesi, and D. Goren-Bar.
The properties of dafex, a database of kinetic facial expressions.
In J. Tao, T. Tan, and R. Picard, editors, *Affective Computing and Intelligent Interaction*, volume 3784 of *Lecture Notes in Computer Science*, pages 558–565. Springer Berlin Heidelberg, 2005.
- [13] M. Bauml, K. Bernardin, M. Fischer, H. Ekenel, and R. Stiefelhagen.
Multi-pose face recognition for person retrieval in camera networks.
In *Advanced Video and Signal Based Surveillance (AVSS), 2010 Seventh IEEE International Conference on*, pages 441–447, Aug 2010.
- [14] Y. Baveye, E. Dellandrea, C. Chamaret, and L. Chen.
Liris-accede: A video database for affective content analysis.
Affective Computing, IEEE Transactions on, 6(1):43–55, Jan 2015.
- [15] B. Ben Amor, H. Drira, S. Berretti, M. Daoudi, and A. Srivastava.
4-d facial expression recognition by learning geometric deformations.
IEEE T. Cybernetics, 44(12):2443–2457, 2014.

- [16] B. Ben Amor, J. Su, and A. Srivastava.
Action recognition using rate-invariant analysis of skeletal shape trajectories.
Pattern Analysis and Machine Intelligence, IEEE Transactions on, PP(99):1–1,
2015.
- [17] L. Benedikt, D. Cosker, P. Rosin, and D. Marshall.
Assessing the uniqueness and permanence of facial actions for use in biometric
applications.
*Systems, Man and Cybernetics, Part A: Systems and Humans, IEEE Transactions
on*, 40(3):449–460, May 2010.
- [18] S. Berretti, A. Del Bimbo, and P. Pala.
3D face recognition using iso-geodesic stripes.
IEEE Trans. on Pattern Analysis and Machine Intelligence, 32(12):2162–2177, Dec.
2010.
- [19] S. Berretti, A. Del Bimbo, and P. Pala.
Real-time expression recognition from dynamic sequences of 3D facial scans.
In *Proceedings of the 5th Eurographics Conference on 3D Object Retrieval*, EG
3DOR'12, pages 85–92. Eurographics Association, 2012.
- [20] S. Berretti, P. Pala, and A. Del Bimbo.
Face recognition by super-resolved 3D models from consumer depth cameras.
Information Forensics and Security, IEEE Transactions on, 9(9):1436–1449, Sept
2014.
- [21] J. R. Beveridge, H. Zhang, B. A. Draper, P. J. Flynn, Z. Feng, P. Huber, J. Kittler,
Z. Huang, S. Li, Y. Li, M. Kan, R. Wang, S. Shan, X. Chen, H. Li, G. Hua,
V. Struc, J. Krizaj, C. Ding, D. Tao, and P. J. Phillips.
Report on the FG 2015 video person recognition evaluation.
In *11th IEEE International Conference and Workshops on Automatic Face and
Gesture Recognition, FG 2015, Ljubljana, Slovenia, May 4-8, 2015*, pages 1–8,
2015.
- [22] K. Bowyer, K. Chang, and P. Flynn.
A survey of approaches and challenges in 3D and multi-modal 3D + 2D face
recognition.
Computer Vision and Image Understanding, 101(1):1–15, 2006.

- [23] V. Bruce, Z. Henderson, K. Greenwood, P. Hancock, A. Burton, and P. Miller. Verification of face identities from images captured on video. *Journal of Experimental Psychology*, 5:339–360, 1999.
- [24] P. Bull. *Communication under the microscope: The theory and practice of microanalysis*. Routledge, 2002.
- [25] R. Calvo and S. D’Mello. Affect detection: An interdisciplinary review of models, methods, and their applications. *Affective Computing, IEEE Transactions on*, 1(1):18–37, Jan 2010.
- [26] H. Cetingul and R. Vidal. Intrinsic mean shift for clustering on stiefel and grassmann manifolds. In *IEEE Conf. on Computer Vision and Pattern Recognition (CVPR)*, pages 1896–1902, Miami Beach, FL, USA, June 2009.
- [27] H. Cetingul and R. Vidal. Sparse riemannian manifold clustering for hardi segmentation. In *IEEE Int. Symp. on Biomedical Imaging: From Nano to Macro*, pages 1750–1753, March 2011.
- [28] C. H. Chan, B. Goswami, J. Kittler, and W. Christmas. Local ordinal contrast pattern histograms for spatiotemporal, lip-based speaker authentication. *Information Forensics and Security, IEEE Transactions on*, 7(2):602–612, April 2012.
- [29] K. Chang, W. Bowyer, and P. Flynn. Multiple nose region matching for 3d face recognition under varying facial expression. *Pattern Analysis and Machine Intelligence, IEEE Transactions on*, 28(10):1695–1700, Oct 2006.
- [30] Y. Chen and G. Medioni. Object modeling by registration of multiple range images. In *Robotics and Automation*, volume 3, pages 2724–2729, 1991.

- [31] S. Cheng, I. Marras, S. Zafeiriou, and M. Pantic.
Active nonrigid ICP algorithm.
In *Proceedings of IEEE International Conference on Automatic Face and Gesture Recognition (FG'15)*, Ljubljana, Slovenia, May 2015.
- [32] J. Choi, A. Sharma, and G. Medioni.
Comparing strategies for 3D face recognition from a 3D sensor.
In *RO-MAN, 2013 IEEE*, pages 19–24, Aug 2013.
- [33] F. Christie and V. Bruce.
The role of dynamic information in the recognition of unfamiliar faces.
Memory and Cognition, 26:780–790, 1998.
- [34] J. Cohn, K. Schmidt, R. Gross, and P. Ekman.
Individual differences in facial expression: stability over time, relation to self-reported emotion, and ability to inform person identification.
In *Multimodal Interfaces, 2002. Proceedings. Fourth IEEE International Conference on*, pages 491–496, 2002.
- [35] D. Cosker, E. Krumhuber, and A. Hilton.
A faces valid 3D dynamic action unit database with applications to 3D dynamic morphable facial modeling.
In *Int. Conf. on Computer Vision (ICCV)*, pages 2296–2303, 2011.
- [36] A. Cruz, B. Bhanu, and N. Thakoor.
Vision and attention theory based sampling for continuous facial emotion recognition.
Affective Computing, IEEE Transactions on, 5(4):418–431, Oct 2014.
- [37] A. Danelakis, T. Theoharis, and I. Pratikakis.
A survey on facial expression recognition in 3D video sequences.
Multimedia Tools and Applications, 74(15):5577–5615, 2015.
- [38] A. Danelakis, T. Theoharis, and I. Pratikakis.
A survey on facial expression recognition in 3D video sequences.
Multimedia Tools and Applications, 74(15):5577–5615, 2015.
- [39] H. Drira, B. Ben Amor, M. Daoudi, A. Srivastava, and S. Berretti.

- 3D dynamic expression recognition based on a novel deformation vector field and random forest.
In *Pattern Recognition (ICPR), 2012 21st International Conference on*, pages 1104–1107, 2012.
- [40] H. Drira, B. Ben Amor, A. Srivastava, M. Daoudi, and R. Slama.
3D face recognition under expressions, occlusions, and pose variations.
IEEE Trans. on Pattern Analysis and Machine Intelligence, 35(9):2270–2283, Sept. 2013.
- [41] M. Du, A. C. Sankaranarayanan, and R. Chellappa.
Robust face recognition from multi-view videos.
IEEE Transactions on Image Processing, 23(3):1105–1117, 2014.
- [42] A. Edelman, T. Arias, and S. Smith.
The geometry of algorithms with orthogonality constraints.
Siam J. Matrix Anal. Appl., 20(2):303–353, 1998.
- [43] G. Edwards, C. Taylor, and T. Cootes.
Improving identification performance by integrating evidence from sequences.
In *Computer Vision and Pattern Recognition, 1999. IEEE Computer Society Conference on.*, volume 1, page 491 Vol. 1, 1999.
- [44] P. Ekman.
Universals and cultural differences in facial expressions of emotion.
In *Nebraska Symposium on Motivation*, volume 19, pages 207–283, Lincoln, NE, 1972.
- [45] T. Fang, X. Zhao, O. Ocegueda, S. K. Shah, and I. A. Kakadiaris.
3D/4D facial expression analysis: An advanced annotated face model approach.
Image and Vision Computing, 30(10):738 – 749, 2012.
- [46] T. Fang, X. Zhao, S. Shah, and I. Kakadiaris.
4d facial expression recognition.
In *Computer Vision Workshops (ICCV Workshops), 2011 IEEE International Conference on*, pages 1594–1601, 2011.
- [47] M.-I. Faraj and J. Bigun.
Audio,Ävisual person authentication using lip-motion from orientation maps.

-
- Pattern Recognition Letters*, 28(11):1368 – 1382, 2007.
Advances on Pattern recognition for speech and audio processing.
- [48] Y. Fu and T. Huang.
Human age estimation with regression on discriminative aging manifold.
Multimedia, IEEE Transactions on, 10(4):578–584, June 2008.
- [49] M. P. G. Sandbach, S. Zafeiriou and L. Yin.
Static and dynamic 3D facial expression recognition: A comprehensive survey.
Image and Vision Computing, 30(10):683 – 697, 2012.
- [50] K. Gallivan, A. Srivastava, X. Liu, and P. Van Dooren.
Efficient algorithms for inferences on grassmann manifolds.
In *Statistical Signal Processing, 2003 IEEE Workshop on*, pages 315–318, 2003.
- [51] S. Gao, I.-H. Tsang, and L.-T. Chia.
Laplacian sparse coding, hypergraph laplacian sparse coding, and applications.
Pattern Analysis and Machine Intelligence, IEEE Transactions on, 35(1):92–104,
Jan 2013.
- [52] G. Golub and C. Van Loan.
Matrix computations (3rd edition).
Johns Hopkins University Press, Baltimore, MD, USA, 1996.
- [53] R. Gopalan, R. Li, and R. Chellappa.
Domain adaptation for object recognition: An unsupervised approach.
In *IEEE Int. Conf. on Computer Vision (ICCV)*, pages 999–1006, Barcelona, Spain,
Nov. 2011.
- [54] B. Goswami, C. H. Chan, J. Kittler, and B. Christmas.
Local ordinal contrast pattern histograms for spatiotemporal, lip-based speaker
authentication.
In *Biometrics: Theory Applications and Systems (BTAS), 2010 Fourth IEEE Inter-
national Conference on*, pages 1–6, Sept 2010.
- [55] I. Gu and Z. Khan.
Grassmann manifold online learning and partial occlusion handling for visual
object tracking under bayesian formulation.
In *Pattern Recognition (ICPR), 2012 21st International Conference on*, pages 1463–
1466, 2012.

- [56] J. Hamm and D. D. Lee.
Grassmann discriminant analysis: A unifying view on subspace-based learning.
In *Int. Conf. on Machine Learning, ICML '08*, pages 376–383, 2008.
- [57] H. Han, C. Otto, X. Liu, and A. K. Jain.
Demographic estimation from face images: Human vs. machine performance.
IEEE Trans. Pattern Anal. Mach. Intell., 37(6):1148–1161, 2015.
- [58] S. Happy, A. Dasgupta, P. Patnaik, and A. Routray.
Automated alertness and emotion detection for empathic feedback during e-learning.
In *Technology for Education (T4E), 2013 IEEE Fifth International Conference on*, pages 47–50, Dec 2013.
- [59] M. Harandi, R. Hartley, C. Shen, B. Lovell, and C. Sanderson.
Extrinsic methods for coding and dictionary learning on grassmann manifolds.
Int. Journal of Computer Vision, 2015, under press.
- [60] M. T. Harandi, C. Sanderson, S. A. Shirazi, and B. C. Lovell.
Graph embedding discriminant analysis on grassmannian manifolds for improved image set matching.
In *IEEE Conf. on Computer Vision and Pattern Recognition (CVPR)*, pages 2705–2712, Colorado Springs, CO, USA, June 2011.
- [61] M. Hayat, M. Bennamoun, and A. El-Sallam.
Fully automatic face recognition from 3D videos.
In *Pattern Recognition (ICPR), 2012 21st International Conference on*, pages 1415–1418, Nov 2012.
- [62] J. Helmke and K. Huper.
Newton’s method on grassmann manifold.
In *Preprint, arXiv:0709.2205*, 2007.
- [63] M. Hoai and F. De la Torre.
Max-margin early event detectors.
Int. Journal of Computer Vision, 107(2):191–202, Feb. 2014.
- [64] G.-S. Hsu, Y.-L. Liu, H.-C. Peng, and P.-X. Wu.
RGB-D-based face reconstruction and recognition.
IEEE Trans. on Information Forensics and Security, 9(12):2110–2118, Dec. 2014.

- [65] G. Hua, M. Yang, E. Learned-Miller, Y. Ma, M. Turk, D. Kriegman, and T. Huang. Introduction to the special section on real-world face recognition. *IEEE Trans. on Pattern Analysis and Machine Intelligence*, 33(10):1921–1924, Oct. 2011.
- [66] Z. Huang, R. Wang, S. Shan, and X. Chen. Projection metric learning on grassmann manifold with application to video based face recognition. In *Computer Vision and Pattern Recognition (CVPR), 2015 IEEE Conference on*, pages 140–149, 2015.
- [67] L. A. Jeni, A. Lorincz, T. Nagy, Z. Palotai, J. Sebok, Z. Szabo, and D. Takacs. 3D shape estimation in video sequences provides high precision evaluation of facial expressions. *Image and Vision Computing*, 30(10):785 – 795, 2012.
3D Facial Behaviour Analysis and Understanding.
- [68] I. Jolliffe.
Principal Component Analysis.
John Wiley and Sons, Ltd, 2005.
- [69] E. J.Su, S.Kurtek and A.Srivastava.
Statistical analysis of trajectories on riemannian manifolds: Bird migration, hurricane tracking and video surveillance.
The Annals of Applied Statistics, 8(1), April 2014.
- [70] P. S. K. Prkachin.
The structure, reliability and validity of pain expression: evidence from patients with shoulder pain.
Pain, 139(2):267 – 274, 2008.
- [71] S. Kaltwang, O. Rudovic, and M. Pantic.
Continuous pain intensity estimation from facial expressions.
In *Advances in visual computing*, volume 7432 of *Lecture notes in computer science*, pages 368–377, Berlin, Germany, 2012. Springer.
- [72] S. K. A. Kamarol, N. S. Meli, M. H. Jaward, and N. Kamrani.
Spatio-temporal texture-based feature extraction for spontaneous facial expression recognition.

- In *Machine Vision Applications (MVA), 2015 14th IAPR International Conference on*, pages 467–470, May 2015.
- [73] H. Karcher.
Riemannian center of mass and mollifier smoothing.
Communications on Pure and Applied Mathematics, 30:509–541, 1977.
- [74] R. Khan, A. Meyer, H. Konik, and S. Bouakaz.
Pain detection through shape and appearance features.
In *Multimedia and Expo (ICME), 2013 IEEE International Conference on*, pages 1–6, July 2013.
- [75] B. Knight and A. Johnston.
The role of movement in face recognition.
Visual Cognition, 2:265–273, 1997.
- [76] S. Koelstra, M. Pantic, and I. Patras.
A dynamic texture-based approach to recognition of facial actions and their temporal models.
IEEE Trans. Pattern Anal. Mach. Intell., 32(11):1940–1954, 2010.
- [77] K. Lander, F. Chrisite, and V. Bruce.
The role of movement in the recognition of famous faces.
Visual Cognition, 6:974–985, 1999.
- [78] V. Le, H. Tang, and T. Huang.
Expression recognition from 3D dynamic faces using robust spatio-temporal shape features.
In *Automatic Face Gesture Recognition and Workshops (FG 2011), 2011 IEEE International Conference on*, pages 414–421, March 2011.
- [79] B. Li, A. Mian, W. Liu, and A. Krishna.
Using kinect for face recognition under varying poses, expressions, illumination and disguise.
In *IEEE Work. on Applications of Computer Vision (WACV)*, pages 186–192, Tampa, FL, USA, Jan. 2013.
- [80] X. Li, T. Pfister, X. Huang, G. Zhao, and M. Pietikainen.
A spontaneous micro-expression database: Inducement, collection and baseline.

- In *Automatic Face and Gesture Recognition (FG), 2013 10th IEEE International Conference and Workshops on*, pages 1–6, April 2013.
- [81] Y. M. Lim, A. Ayesh, and M. Stacey.
Detecting emotional stress during typing task with time pressure.
In *Science and Information Conference (SAI), 2014*, pages 329–338, Aug 2014.
- [82] P. Liu and L. Yin.
Spontaneous facial expression analysis based on temperature changes and head motions.
In *Automatic Face and Gesture Recognition (FG), 2015 11th IEEE International Conference and Workshops on*, pages 1–6, May 2015.
- [83] X. Liu and T. Chen.
Video-based face recognition using adaptive hidden markov models.
In *IEEE Conf. on Computer Vision and Pattern Recognition (CVPR)*, pages 340–345, Madison, WS, USA, June 2003.
- [84] S. Liwicki, G. Tzimiropoulos, S. Zafeiriou, and M. Pantic.
Efficient online subspace learning with an indefinite kernel for visual tracking and recognition.
IEEE Transactions on Neural Networks and Learning Systems, 23:1624–1636, October 2012.
- [85] P. Lucey, J. Cohn, K. Prkachin, P. Solomon, and I. Matthews.
Painful data: The unbc-mcmaster shoulder pain expression archive database.
In *Automatic Face Gesture Recognition and Workshops (FG 2011), 2011 IEEE International Conference on*, pages 57–64, March 2011.
- [86] P. Lucey, J. F. Cohn, K. M. Prkachin, P. E. Solomon, S. Chew, and I. Matthews.
Painful monitoring: Automatic pain monitoring using the unbc-mcmaster shoulder pain expression archive database.
Image and Vision Computing, 30(3):197 – 205, 2012.
Best of Automatic Face and Gesture Recognition 2011.
- [87] J. Luettin, N. Thacker, and S. Beet.
Speaker identification by lipreading.
In *Spoken Language, 1996. ICSLP 96. Proceedings., Fourth International Conference on*, volume 1, pages 62–65 vol.1, Oct 1996.

- [88] Y. M. Lui.
Advances in matrix manifolds for computer vision.
Image Vision Computing, 30(6-7):380–388, June 2012.
- [89] Y. M. Lui and J. R. Beveridge.
Grassmann registration manifolds for face recognition.
In *European Conf. on Computer Vision, ECCV'08*, pages 44–57, 2008.
- [90] M. Mahmoud, T. Baltrušaitis, P. Robinson, and L. Riek.
3D corpus of spontaneous complex mental states.
In *Conf. on Affective Computing and Intelligent Interaction*, pages 205–214, Memphis, TN, USA, Oct. 2011.
- [91] B. Matuszewski, W. Quan, L.-k. Shark, A. McLoughlin, C. Lightbody, H. Emsley, and C. Watkins.
Hi4d-adsip 3D dynamic facial articulation database.
Image and Vision Computing, 30(10), 2012.
- [92] S. Mavadati, M. Mahoor, K. Bartlett, P. Trinh, and J. Cohn.
Disfa: A spontaneous facial action intensity database.
Affective Computing, IEEE Transactions on, 4(2):151–160, April 2013.
- [93] G. McKeown, M. Valstar, R. Cowie, and M. Pantic.
The semaine corpus of emotionally coloured character interactions.
In *Multimedia and Expo (ICME), 2010 IEEE International Conference on*, pages 1079–1084, July 2010.
- [94] H. Meeren, C. van Heijnsbergen, and B. de Gelder.
Rapid perceptual integration of facial expression and emotional body language.
National Academy of Sciences USA, 102(45):16518–16523, 2005.
- [95] A. Mehrabian and M. WIENER.
Decoding of inconsistent communications.
Journal of Personality and Social Psychology, 6(1):109–114, May 1967.
- [96] R. Min, J. Choi, G. Medioni, and J.-L. Dugelay.
Real-time 3D face identification from a depth camera.
In *Int. Conf. on Pattern Recognition (ICPR)*, pages 1739–1742, Tsukuba, Japan, Nov. 2012.

- [97] B. Mishra, S. Fernandes, K. Abhishek, A. Alva, C. Shetty, C. Ajila, D. Shetty, H. Rao, and P. Shetty.
Facial expression recognition using feature based techniques and model based techniques: A survey.
In *Electronics and Communication Systems (ICECS), 2015 2nd International Conference on*, pages 589–594, 2015.
- [98] M. S. Mohamad-Hoseyn Sigari, Muhammad-Reza Pourshahabi and M. Fathy.
A review on driver face monitoring systems for fatigue and distraction detection.
International Journal of Advanced Science and Technology, 46(0):73 – 100, 2014.
- [99] N. Nguyen and Y. Guo.
Comparisons of sequence labeling algorithms and extensions.
In *Int. Conf. on Machine Learning, ICML '07*, pages 681–688, 2007.
- [100] M. Pantic.
Facial Expression Recognition, pages 1–8.
2014.
- [101] P. Phillips, P. Flynn, W. Scruggs, K. Bowyer, J. Chang, K. Hoffman, J. Marques, J. Min, and W. Worek.
Overview of the face recognition grand challenge.
In *IEEE Int. Conf. on Computer Vision and Pattern Recognition (CVPR)*, pages 947–954, San Diego, CA, USA, June 2005.
- [102] P. J. Phillips and A. J. O’Toole.
Comparison of human and computer performance across face recognition experiments.
Image Vision Comput., 32(1):74–85, 2014.
- [103] E. Piatkowska and J. Martyna.
Spontaneous facial expression recognition: Automatic aggression detection.
In E. Corchado, V. Snasel, A. Abraham, M. Wozniak, M. Grana, and S.-B. Cho, editors, *Hybrid Artificial Intelligent Systems*, volume 7208 of *Lecture Notes in Computer Science*, pages 147–158. Springer Berlin Heidelberg, 2012.
- [104] G. Pike, R. . Kemp, A. Towell, and C. Keith.
Recognizing moving faces: The relative contribution of motion and perspective view information.

- Visual Cognition*, 4:409–438, 1997.
- [105] M. Reale, X. Zhang, and L. Yin.
Nebula feature: A space-time feature for posed and spontaneous 4d facial behavior analysis.
In *Automatic Face and Gesture Recognition (FG), 2013 10th IEEE International Conference and Workshops on*, pages 1–8, 2013.
- [106] Q. Rentmeesters, P.-A. Absil, P. Van Dooren, K. Gallivan, and A. Srivastava.
An efficient particle filtering technique on the grassmann manifold.
In *Acoustics Speech and Signal Processing (ICASSP), 2010 IEEE International Conference on*, pages 3838–3841, March 2010.
- [107] M. Roach, J. Brand, and J. Mason.
Acoustic and facial features for speaker recognition.
In *Pattern Recognition, 2000. Proceedings. 15th International Conference on*, volume 3, pages 258–261 vol.3, 2000.
- [108] D. Roark, S. Barrett, M. Spence, A. Abdi, and A. O’Toole.
Psychological and neural perspectives on the role of motion in face recognition.
Behavioral and Cognitive Neuroscience Reviews, 2:15–46, 2003.
- [109] G. I. Roisman and J. L. Tsai.
The emotional integration of childhood experience: Physiological, facial expressive, and self-reported emotional response during the adult attachment interview.
Developmental Psychology, pages 776–789, 2004.
- [110] D. Rueckert, A. Frangi, and J. Schnabel.
Automatic construction of 3D statistical deformation models using non-rigid registration.
In W. Niessen and M. Viergever, editors, *Medical Image Computing and Computer-Assisted Intervention, À MICCAI 2001*, volume 2208 of *Lecture Notes in Computer Science*, pages 77–84. Springer Berlin Heidelberg, 2001.
- [111] J. Russell and A. Mehrabian.
Evidence for a three-factor theory of emotions.
Journal of Research in Personality, 11(3):273–294, Sept. 1977.
- [112] G. Sandbach, S. Zafeiriou, M. Pantic, and D. Rueckert.

- A dynamic approach to the recognition of 3D facial expressions and their temporal models.
In *IEEE Conf. on Automatic Face and Gesture Recognition*, pages 406–413, Santa Barbara, CA, Mar. 2011.
- [113] G. Sandbach, S. Zafeiriou, M. Pantic, and D. Rueckert.
Recognition of 3D facial expression dynamics.
Image and Vision Computing, 30(10):762–773, 2012.
3D Facial Behaviour Analysis and Understanding.
- [114] E. Sariyanidi, H. Gunes, and A. Cavallaro.
Automatic analysis of facial affect: A survey of registration, representation, and recognition.
Pattern Analysis and Machine Intelligence, IEEE Transactions on, 37(6):1113–1133, June 2015.
- [115] K. Schindler and L. Van Gool.
Action snippets: How many frames does human action recognition require?
In *IEEE Conf. on Computer Vision and Pattern Recognition*, pages 1–8, June 2008.
- [116] R. Séguier.
A very fast adaptive face detection system.
International conference on visualization, imaging, and image processing, 2004.
- [117] T. Senechal, J. Turcot, and R. El Kaliouby.
Smile or smirk? automatic detection of spontaneous asymmetric smiles to understand viewer experience.
In *Automatic Face and Gesture Recognition (FG), 2013 10th IEEE International Conference and Workshops on*, pages 1–8, April 2013.
- [118] J. Shao, I. Gori, S. Wan, and J. Aggarwal.
3D dynamic facial expression recognition using low-resolution videos.
Pattern Recognition Letters, 2015.
- [119] R. Shigenaka, B. Raytchev, T. Tamaki, and K. Kaneda.
Face sequence recognition using grassmann distances and grassmann kernels.
In *IEEE Int. Joint Conf. on Neural Networks (IJCNN)*, pages 1–7, Brisbane, QLD, Australia, June 2012.

- [120] S. A. Shirazi, M. T. Harandi, B. C. Lovell, and C. Sanderson.
Object tracking via non-euclidean geometry: A grassmann approach.
CoRR, abs/1403.0309, 2014.
- [121] S. A. Shirazi, M. T. Harandi, C. Sanderson, A. Alavi, and B. C. Lovell.
Clustering on grassmann manifolds via kernel embedding with application to
action analysis.
In *IEEE Int. Conf. on Image Processing (ICIP)*, pages 781–784, Orlando, FL, USA,
Sept. 2012.
- [122] K. Sikka, A. Dhall, and M. Bartlett.
Weakly supervised pain localization using multiple instance learning.
In *Automatic Face and Gesture Recognition (FG), 2013 10th IEEE International
Conference and Workshops on*, pages 1–8, April 2013.
- [123] M. Soleymani, J. Lichtenauer, T. Pun, and M. Pantic.
A multimodal database for affect recognition and implicit tagging.
Affective Computing, IEEE Transactions on, 3(1):42–55, Jan 2012.
- [124] A. Srivastava.
A bayesian approach to geometric subspace estimation.
IEEE Trans. on Signal Processing, 48(5):1390–1400, May 2000.
- [125] L. Steede, J. Tree, and H. G.J.
I can't recognize your face but i can recognize its movement.
Cognitive Neuropsychology, 24:451–466, 2007.
- [126] L. Su, S. Kumano, K. Otsuka, D. Mikami, J. Yamato, and Y. Sato.
Early facial expression recognition with high-frame rate 3D sensing.
In *IEEE Int. Conf. on Systems, Man, and Cybernetics*, pages 3304–3310, Oct 2011.
- [127] L. Su and Y. Sato.
Early facial expression recognition using early rankboost.
In *IEEE Int. Conf. on Automatic Face and Gesture Recognition*, pages 1–7, April
2013.
- [128] Y. Sun, X. Chen, M. Rosato, and L. Yin.
Tracking vertex flow and model adaptation for three-dimensional spatiotemporal
face analysis.

-
- Systems, Man and Cybernetics, Part A: Systems and Humans, IEEE Transactions on*, 40(3):461–474, May 2010.
- [129] M. Tistarelli and M. S. Nixon, editors.
Advances in Biometrics, Third International Conference, ICB 2009, Alghero, Italy, June 2-5, 2009. Proceedings, volume 5558 of *Lecture Notes in Computer Science*. Springer, 2009.
- [130] I. Tsochantaridis, T. Joachims, T. Hofmann, and Y. Altun.
Large margin methods for structured and interdependent output variables.
Journal of Machine Learning Research, 6:1453–1484, Sept. 2005.
- [131] S. Tulyakov, T. Slowe, Z. Zhang, and V. Govindaraju.
Facial expression biometrics using tracker displacement features.
In *Computer Vision and Pattern Recognition, 2007. CVPR '07. IEEE Conference on*, pages 1–5, June 2007.
- [132] P. Turaga, A. Veeraraghavan, A. Srivastava, and R. Chellappa.
Statistical computations on grassmann and stiefel manifolds for image and video-based recognition.
IEEE Trans. on Pattern Analysis and Machine Intelligence, 33(11):2273–2286, Nov. 2011.
- [133] M. Turk and A. Pentland.
Face recognition using eigenfaces.
In *Computer Vision and Pattern Recognition, 1991. Proceedings CVPR '91., IEEE Computer Society Conference on*, pages 586–591, Jun 1991.
- [134] G. Tzimiropoulos, S. Zafeiriou, and M. Pantic.
Subspace learning from image gradient orientations.
Pattern Analysis and Machine Intelligence, IEEE Transactions on, 34(12):2454–2466, Dec 2012.
- [135] J. Van den Stock, R. Righart, and B. de Gelder.
Body expressions influence recognition of emotions in the face and voice.
Emotion, 7:487–494, August 2007.
- [136] R. Vemulapalli, J. Pillai, and R. Chellappa.
Kernel learning for extrinsic classification of manifold features.

- In *IEEE Conf. on Computer Vision and Pattern Recognition (CVPR)*, pages 1782–1789, Portland, OR, USA, June 2013.
- [137] F. Wallhoff, B. Schuller, M. Hawellek, and G. Rigoll.
Efficient recognition of authentic dynamic facial expressions on the feedtum database.
In *Multimedia and Expo, 2006 IEEE International Conference on*, pages 493–496, July 2006.
- [138] L. Wang and D. Suter.
Learning and matching of dynamic shape manifolds for human action recognition.
Image Processing, IEEE Transactions on, 16(6):1646–1661, June 2007.
- [139] S. Wang, Z. Liu, S. Lv, Y. Lv, G. Wu, P. Peng, F. Chen, and X. Wang.
A natural visible and infrared facial expression database for expression recognition and emotion inference.
Multimedia, IEEE Transactions on, 12(7):682–691, Nov 2010.
- [140] J. Wright, A. Y. Yang, A. Ganesh, S. S. Sastry, and Y. Ma.
Robust face recognition via sparse representation.
IEEE Trans. on Pattern Analysis and Machine Intelligence, 31(2):210–227, Feb. 2009.
- [141] Y. Xie, J. Ho, and B. Vemuri.
On a nonlinear generalization of sparse coding and dictionary learning.
In *Int. Conf. of Machine Learning (ICML)*, pages 1480–1488, Atlanta, GE, USA, June 2013.
- [142] Y. Xu, Z. Xiao, and X. Tian.
A simulation study on neural ensemble sparse coding.
In *Int. Conf. on Information Engineering and Computer Science (ICIECS)*, pages 1–4, Wuhan, China, Dec. 2009.
- [143] M. Xue, A. Mian, W. Liu, and L. Li.
Automatic 4d facial expression recognition using DCT features.
In *Applications of Computer Vision (WACV), 2015 IEEE Winter Conference on*, pages 199–206, Jan 2015.
- [144] B. Yang, J. Yan, Z. Lei, and S. Li.

- Fine-grained evaluation on face detection in the wild.
In *Automatic Face and Gesture Recognition (FG), 2015 11th IEEE International Conference and Workshops on*, pages 1–7, May 2015.
- [145] M. Yang, D. Zhang, J. Yang, and D. Zhang.
Robust sparse coding for face recognition.
In *IEEE Conf. on Computer Vision and Pattern Recognition (CVPR)*, pages 625–632, Colorado Springs, CO, USA, June 2011.
- [146] C. Yasuko.
Statistics on special manifolds, lecture notes in statistics.
In *vol. 174. New York: Springer*, 2003.
- [147] N. Ye and T. Sim.
Towards general motion-based face recognition.
In *Computer Vision and Pattern Recognition (CVPR), 2010 IEEE Conference on*, pages 2598–2605, June 2010.
- [148] L. Yin, X. Chen, Y. Sun, T. Worm, and M. Reale.
A high-resolution 3D dynamic facial expression database.
In *IEEE Conf. on Face and Gesture Recognition (FG)*, pages 1–6, Amsterdam, The Netherlands,, Sept. 2008.
- [149] S. Zafeiriou and M. Pantic.
Facial behaviometrics: The case of facial deformation in spontaneous smile/laughter.
In *Computer Vision and Pattern Recognition Workshops (CVPRW), 2011 IEEE Computer Society Conference on*, pages 13–19, June 2011.
- [150] Z. Zeng, Y. Fu, G. Roisman, Z. Wen, Y. Hu, and T. Huang.
One-class classification for spontaneous facial expression analysis.
In *Int. Conf. on Automatic Face and Gesture Recognition (FGR)*, pages 281–286, April 2006.
- [151] Z. Zeng, M. Pantic, G. Roisman, and T. Huang.
A survey of affect recognition methods: Audio, visual, and spontaneous expressions.
IEEE Trans. on Pattern Analysis and Machine Intelligence, 31(1):39–58, Jan. 2009.
- [152] L. Zhang, H. Nejati, L. Foo, K. T. Ma, D. Guo, and T. Sim.

- A talking profile to distinguish identical twins.
In Automatic Face and Gesture Recognition (FG), 2013 10th IEEE International Conference and Workshops on, pages 1–6, April 2013.
- [153] X. Zhang and Y. Gao.
Face recognition across pose: A review.
Pattern Recognition, 42(11):2876–2896, 2009.
- [154] X. Zhang, L. Yin, and J. F. Cohn.
Three dimensional binary edge feature representation for pain expression analysis.
In Automatic Face and Gesture Recognition (FG), 2015 11th IEEE International Conference and Workshops on, pages 1–7, May 2015.
- [155] X. Zhang, L. Yin, J. F. Cohn, S. Canavan, M. Reale, A. Horowitz, P. Liu, and J. M. Girard.
Bp4d-spontaneous: a high-resolution spontaneous 3D dynamic facial expression database.
Image and Vision Computing, 32(10):692 – 706, 2014.
- [156] Y. Zhang, S. J. Kundu, D. B. Goldgof, S. Sarkar, and L. V. Tsap.
Elastic face, an anatomy-based biometrics beyond visible cue.
In In Proceedings of International Conference on Pattern Recognition, 2004.
- [157] G. Zhao and M. Pietikainen.
Dynamic texture recognition using local binary patterns with an application to facial expressions.
Pattern Analysis and Machine Intelligence, IEEE Transactions on, 29(6):915–928, 2007.
- [158] W. Zhao, R. Chellappa, P. J. Phillips, and A. Rosenfeld.
Face recognition: A literature survey.
ACM Comput. Surv., 35(4):399–458, Dec. 2003.
- [159] X. Zhu, Z. Lei, J. Yan, D. Yi, and S. Z. Li.
High-fidelity pose and expression normalization for face recognition in the wild.
June 2015.
- [160] W. Zuo, D. Meng, L. Zhang, X. Feng, and D. Zhang.
A generalized iterated shrinkage algorithm for non-convex sparse coding.

In *IEEE Int. Conf. on Computer Vision (ICCV)*, pages 217–224, Sydney, Australia, Dec 2013.

